Single Crystal Sapphire Photonic Crystal Fibers

Neal Thomas Pfeiffenberger

Dissertation submitted to the faculty of the Virginia Polytechnic Institute and State University in partial fulfillment of the requirements for the degree of

Doctor of Philosophy
In
Materials Science and Engineering

Gary R. Pickrell
William T. Reynolds
Yong Xu
Carlos T. A. Suchicital

August 27, 2012
Blacksburg, VA

Keywords: Photonic Crystal, Sapphire, Sensor, Modeling

Single Crystal Sapphire Photonic Crystal Fibers

Neal Thomas Pfeiffenberger

ABSTRACT

A single crystal sapphire optical fiber has been developed with an optical cladding that is used to reduce the number of modes that propagate in the fiber. This fiber is the first single crystal sapphire photonic crystal fiber ever produced. Fabrication of the optical cladding reduces the number of modes in the fiber by lowering the effective refractive index around the core, which limits the amount of loss. Different fiber designs were analyzed using Comsol Multiphysics to find the modal volumes of each. The MIT Photonic Bands modeling program was used to see if the first photonic band gap fiber could be achieved theoretically. The fibers were qualified using far field pattern and photodetector measurements as well as gas sensing experiments. The fibers were then exposed to a harsh environment of 1000 °C with a coating of alumina to test the resistance to scattering of the fiber. The fibers were also examined using materials characterization equipment to see how the harsh environments impacted the optical and mechanical stability of the bundled fiber.

Dedication

I would like to dedicate this work to my family and friends. Without their love and support I would not be where I am today.

Acknowledgments

First, I would like to thank all of my co-workers at DuPont. Without your guidance I would have never considered graduate school. I would also like to thank my advisor Dr. Gary Pickrell, whose advice and guidance during this process has been invaluable. I would like to thank my committee members Dr. Suchicital, Dr. Reynolds, and Dr. Xu for their guidance throughout this endeavor. I would like to thank Dr. Brian Scott and Dr. Vincent Pureur for blazing the trail and helping me with all of my research along the way. I would also like to thank my friends Tim Ciarkowski, Gabby Ferrar, Tyler Horseman, Cheng Ma, Zhipeng Tian, Mohammad Al-Mamun, Michael Fraser, and Sean Dee for helping me with my classes and understanding materials science. I would also like to thank my friends at CPT who have selflessly taught me everything I know about optics. Lastly, I would like to thank Danielle Gross-Eskin; she has supported me throughout this endeavor and has shown me more patience than I ever thought possible.

Table of Contents

List of Figures

List of Tables

1. Introduction

Optical fibers find wide use in communications and sensing systems. They can be produced from many different materials such as glass, plastic, and single crystals in a large variety of configurations and dimensions. Long distance communication fibers are composed of a solid glass core surrounded by a solid glass cladding of lower refractive index, which serves to confine light to the central core, thereby minimizing the transmission loss. Single crystal sapphire fibers are highly multimode due to their large refractive index difference between the core (n_1 = 1.744 at 1.693 μm) and air (n_2 = 1.0). The single crystal sapphire bundled fiber works by changing the effective index of the cladding region (replacing the n_2=1.0 with an average of 1.744 and 1.0 due to the six rods of single crystal sapphire). These "non" photonic band gap photonic crystal fibers (PCF) can still strongly confine light by lowering the average effective index of the cladding region. There have been many useful fibers that have come from these types of fibers but all of them are based on silica. Single mode guidance for a single crystal sapphire fiber is desired to reduce attenuation, increase bandwidth, and reduce the losses caused by modal dispersion.

There is currently much interest in single crystal sapphire optical fibers due mainly to their ability to survive high temperatures and harsh chemical environments. Single crystal sapphire can transmit light over a wide wavelength range but does have a relatively high transmission loss compared to that of standard telecommunications optical fibers composed of silica. One use for single crystal sapphire fibers is in highly corrosive, toxic environments at high temperatures and pressures. Fiber optics, in general, are immune to electromagnetic interference and radiation making them ideal for sensing pressure and temperature in these environments.

Presently, most sensor-based fibers are made from silica glass due to its low transmission loss, 0.16 dB/km at 1.55 μm, high availability, and comparatively low cost[1]. The silica fibers are usually coated with polymers such as acrylate and polyimide, but coatings can be made of metals and carbon as well. This coating serves to protect the fiber from the outside environment, as oftentimes moisture will penetrate tiny cracks on the silica surface causing the cracks to propagate under stress, eventually weakening the fiber[2]. Coatings also serve to inhibit water diffusion into the fiber.

Single crystal sapphire (α-Al_2O_3) grown along the C-axis has a melting temperature[3] of 2053 °C, which is much higher than that of a comparable fused silica fiber that has a maximum usage temperature near 700 °C. At 1025 °C, fused silica reaches its strain point and creep is induced by the strain at high temperatures[4]. When the temperature is raised above 1000 °C, dopants in the silica begin to migrate from the core leaving the fiber unfit for sensing[5]. Single crystal sapphire's high melting temperature, chemical inertness, resistance to corrosion, high sensitivity, large bandwidth, and immunity to electromagnetic interference and radiation make it a reliable choice for harsh environment sensing.

Single crystal sapphire fibers are a new technology and are being heavily researched due to their high potential in sensing applications. In order for these fibers to become useful they must be able to have long lengths, low loss, and the ability to be clad. Cladding helps to protect the fiber while limiting attenuation and confining the optical signal to the core. A reduction in the number of modes due to this cladding will lessen the loss of the fiber, which is why a single mode sapphire fiber is desired. For single mode operation to occur in a single crystal sapphire fiber in

air, the fiber diameter would need to be in the range of 0.1 to 1 μm[6] for the transparency window7 (0.19 – 5.2 μm) of sapphire. This is given by Equation 1 for single mode operation that states6

$$d = \lambda*(2.405)/\pi*n_s \quad (1)$$

where d is the diameter of the sapphire rod, λ is the wavelength, and $ns = \sqrt{\frac{n_f{}^2}{n_c{}^2}}$. The refractive index of sapphire core is n_f with the refractive index of the air cladding being n_c at their corresponding wavelength. When the single crystal sapphire fiber is clad, the delta Δ, which is the difference in refractive index between the core and cladding layers, decreases and the diameter of the sapphire core can be a larger value. Fabrication of a successful single crystal sapphire fiber with a cladding layer will enable the continued development of lower loss high temperature sensors by reducing surface contamination, less loss over long distances, easier creation of fiber interferometers, and stronger core confinement due to a reduction of propagating modes. This in turn will improve the efficiency of optical processing and will eventually allow for single mode operation.

The development of cladding for single crystal sapphire fibers will allow for better pressure and temperature sensing in very corrosive environments that glass-based fibers would typically not be able to survive. Currently, the use of single crystal sapphire fibers in high temperature applications is limited to a bare fiber surrounded by the environment that it will be sensing. If this environment is air, a large refractive index difference is created between the sapphire core and the air cladding causing the fiber to be highly multimode. A core that has no cladding is also more susceptible to surface contaminants as well as not having the physical support that a

cladding provides. The fabrication of single crystal sapphire fibers with cladding has remained unproven so far. Through the incorporation of an all-single crystal sapphire cladding, the effective index difference between the core and cladding layer is reduced, minimizing surface contaminants on the core, and providing greater physical support. The question to be answered remains what is the optimal fiber design to allow for a reduction of modes while giving the ability to have a sapphire optical fiber with a cladding layer that can protect the core from various contaminants. We will be able to test this question through the use of optical modeling and optical characterization. Both will allow us to prove the reduction of modes while the optical characterization will allow us to examine the optimized transmission and gas sensing abilities of the bundled single crystal sapphire fiber.

This research covers the background, fiber modeling, experimental procedure, and the results and discussion. The background covers the main subjects essential to understanding the research. The fiber modeling section allows for optical modeling data to be designed and optimized before fabrication to determine the best path forward. The experimental procedure section focuses on the setup for the testing of the different fiber structures. The results and discussion section will examine the data to prove the usefulness of these fiber designs and open the door for further applications based on the results.

2. Background

2.1 Single Crystal Sapphire

Single crystal sapphire is a material that has a continuous crystal lattice with no grain boundaries present. Single crystal materials have high strength and no porosity compared to their

polycrystalline counterpart. Single crystal sapphire, which is comprised of α-Al_2O_3, has a refractive index of 1.744 at 1.693 µm. It is a uniaxial crystal, which is a member of the trigonal system[7] and belongs to the space group R-3c. It has a broad transmission window[8] from 0.19 µm to 5.2 µm making it very useful for high power applications. Single crystal sapphire is more brittle than fused silica due to a much larger Young's modulus value (400 GPa vs. 73 GPa for that of fused silica)[7]. Single crystal sapphire fibers for this work were grown with the C-axis of the crystal extending along the optical axis of the fiber (along the length of the fiber). Since single crystal sapphire has a hexagonal crystal structure, the two axes perpendicular to the C-axis are equivalent and are referred to as the A-axes. Sapphire has more optical loss than fused silica, is more expensive, and is more difficult to fabricate. The main reason sapphire is being considered for this study is its resistance to corrosion in harsh, high-temperature environments. Sapphire, like silica, also has the capability to transmit light radiation at infrared (IR) wavelengths. It comes in both single crystal and polycrystalline form. The transmission spectrum measured in Nubling's work[9] (with the discrete squares giving the measured transmission for bulk sapphire[10]) can be seen in Figure 2.1 below. Sapphire has a loss minimum of 0.13 dB/m at 2.94 µm, but is transparent over the 0.24 – 4.0 µm spectrum9 with a respective refractive index operation range from 1.785 – 1.674 and a birefringence of -0.008.

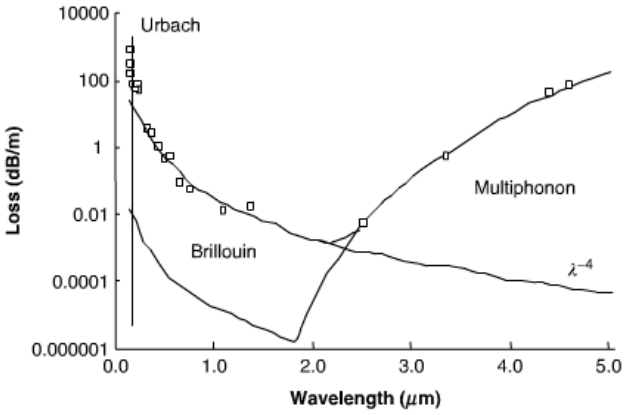

Figure 2.1 Theoretical vs. measured attenuation in bulk sapphire from reference [9] with permission

Multi-phonon absorption in the sapphire crystal occurs when two or more phonons interact producing dipole moments that the incident irradiation can couple. The maximum coupling occurs when the vibrational mode of the molecular dipole is equal to the frequency in the far IR spectrum. This Brillouin scattering is caused when phonons are scattered by a vibration in the crystal lattice. The Urbach edge causes an increase of the absorption coefficient as the frequency approaches the band gap energy7 of sapphire (9.9 eV). Rayleigh scattering is also predicted to exist due to inhomogeneities in the crystal, which are small compared to the wavelength of light.

Currently, most single crystal sapphire fibers are created by two different growth methods. The first is the laser heated pedestal growth method (LHPG) which has been studied extensively by researchers at many universities[11-16]. The other method of single crystal sapphire growth is the edge-defined film fed growth method[17] (EFG), which is used by Saphikon, Inc. Growth methods are important to examine because defects in the fabrication process translate into optical scattering and loss. It is also important to note that the complicated growth processes are the main limiting factor, second to cost of the material that limits their production. This is due to the

fact that only relatively short lengths of single crystal sapphire can be produced. The EFG method has losses that average near 1.5 to 2.0 dB/m but multiple fibers can be grown at the same time[18-20]. Both methods currently do not permit sapphire to be grown with a cladding. In addition, neither permits the fiber to be single mode operation at this time.

The LHPG process is a higher-cost and better optical quality process that begins with growth from a molten tip of source crystal. A CO_2 laser is focused onto an Al_2O_3 source rod seed crystal. The shape of the fiber is determined by the surface tension of the molten zone as seen in the diagram[21] in Figure 2.2 below.

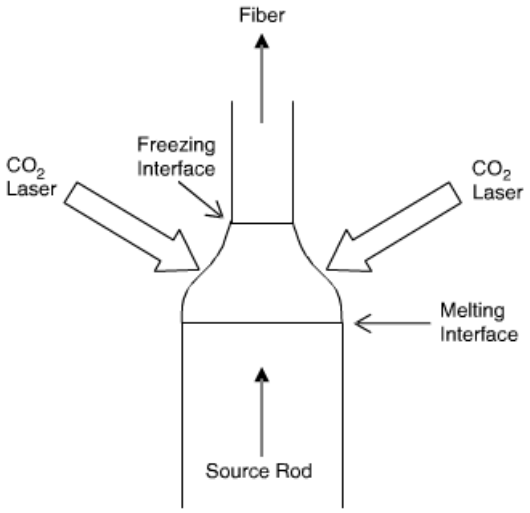

Figure 2.2 Laser-heated pedestal growth method (LHPG) schematic used from reference [22] with permission

Small adjustments in the source rod feed rate and the rate at which the seed crystal moves away from the source rod determine the diameter of the resultant fiber. This diameter is approximately one third the dimension of the source rod[22]. The dimensions of the source rod determine the maximum length of fiber that can be obtained. The purity of the source rod also directly determines the purity of the resultant fiber. The LHPG process is enclosed in an atmosphere

controlled environment to reduce the air currents or other perturbations caused by fluctuations in the CO_2 laser, a change in source feed rate, or exposure to OH^- or other gaseous species that could induce loss[22].

The EFG process, which was invented by Saint-Gobain Saphikon, allows for multiple fibers to be grown at the same time. This process uses a molybdenum crucible full of molten sapphire. The molten source material moves into the die tip, which forms a meniscus that is drawn into a fiber. This process does induce some molybdenum contaminants into the resultant sapphire fiber (on the order of 5 ppm[22]). As in the LHPG process, the EFG process is carried out in an enclosed environment to reduce air currents and other defects. This process can be expanded to produce multiple fibers at the same time by adding multiple capillary tubes into the molybdenum die. The resultant fiber diameter will directly correspond to the outer diameter of the die tip. The typical length of a bare single crystal sapphire fiber available for purchase is 2 meters in length[21]. A schematic of the EFG process diagram[22] can be seen in Figure 2.3 below.

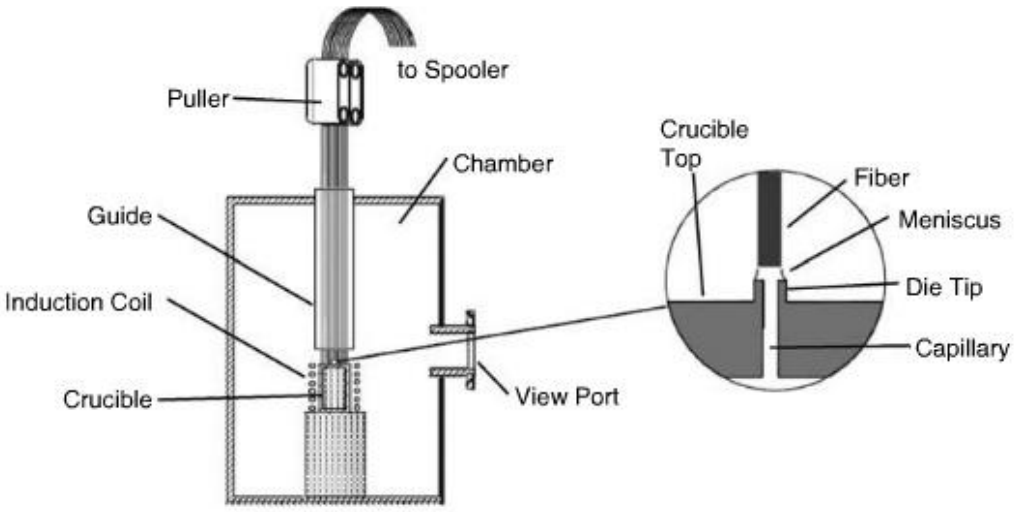

Figure 2.3 Edge-defined film fed growth method (EFG) schematic used from reference [22] with permission

Both the LHPG and EFG methods have a post-annealing step to aid in the reduction of defects. This post-anneal temperature9 is generally 1000 °C in an enclosed oxygen or air environment. Loss transmission spectra[22] of both the LHPG vs. EFG methods can be found in Figure 2.4 below.

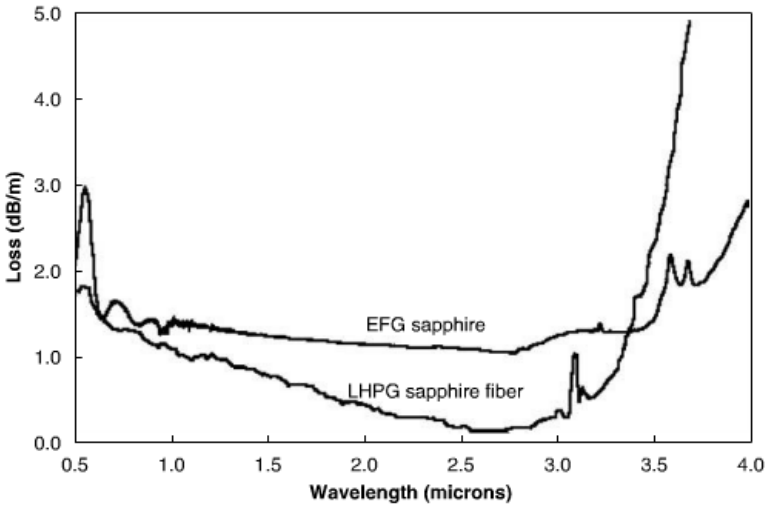

Figure 2.4 Loss transmission of EFG vs. LHPG growth methods for single crystal sapphire used from reference [22] with permission

The EFG process, which was once thought to be inferior to the LHPG process, has recently been approaching LHPG in terms of fiber quality[23]. Scattering and absorption are the main causes of extrinsic loss in sapphire fibers. The scattering is mainly due to inhomogeneities, surface defects, and voids, while the absorption is due to color centers and impurities in the source material and other gaseous species present in the fabrication process[22]. OH^- hole center impurities are prevalent from 0.41 – 3.0 μm, with the O^{2-} ion trapping a hole pair near an Al^{3+} vacancy. Annealing the fiber after fabrication can decrease the resultant absorption. Dislocations in sapphire fibers, in general, do occur, but in far less amounts compared to bulk sapphire due to their small fiber diameter. Twinning and other dislocation effects are also vastly reduced in sapphire fibers due to the small fiber diameters.

It is difficult to clad a single crystal sapphire fiber using the current fabrication methods (EFG and LHPG) due to convective currents in the molten area, which alter the structure of the source rod[24]. Cladding a single crystal optical fiber serves three main purposes. The first is to decrease the effective refractive index difference between the core and cladding layer; the second to reduce the amount of contaminants on the surface of the core, and the third is to increase the mechanical stability of the core. This will reduce scattering caused by the scattered mode coupling into other modes that are propagating in the fiber. Surface contaminants will also attenuate the intensity of the optical signal. When a contaminant has a refractive index higher than that of the sapphire core, scattering losses will occur due to a slower travel speed. If the contaminant has a refractive index lower than that of sapphire, a faster travel speed will occur causing any interacting modes to propagate faster than that of the modes in the core[25]. In both

refractive index cases, if a solid contaminant is present, and its diameter is larger than that of the transmitted wavelength, scattering losses will occur.

In order for a single crystal sapphire fiber to approach single mode guidance, a cladding material will need to have a refractive index less than that of the sapphire core. Many materials have been examined for a post fabrication cladding through a variety of deposition techniques. The main problem is finding a cladding material that is transparent, has a lower refractive index than sapphire, has no detrimental phase changes, has a similar coefficient of thermal expansion, can temperature cycle adequately at high temperatures, all while forming a layer that does not stress the sapphire core. Deposition techniques include both direct and ion exchange techniques. Direct deposition techniques, which are the most researched, include chemical solution deposition, metal organic chemical vapor deposition, and physical vapor deposition[22]. Current materials that are being examined by researchers[26] include SiO_xN_y, Mg_xSiO_y, Ti_xSi_yO, polycrystalline alumina, silicon carbide, zirconia, and niobium with the x and y values having the ability to be changed to alter the refractive index of the coating. The main problem with all of these coatings is the stability at high temperatures as most react or strain the sapphire surface well before sapphire's melting temperature is reached[22].

Full utilization of these devices has not been realized in large part owing to the lack of appropriate high temperature claddings on sapphire optical fibers. The lack of cladding on the single crystal sapphire fibers results in higher environmental vulnerability of the single crystal sapphire fibers due to fluctuations in the optical signal as a result of materials adsorbed onto the fiber surface or reactions at the sapphire surface; higher modal volume resulting in higher phase

difference between low and high order modes; and increased sensitivity to the effects of fiber bending due to the loss of the higher order modes.

The effect of the incorporation of "holes" or tubes into the cladding region to lower the effective index of that region is well documented in the literature for silica fibers. This gives rise to an index difference between the core and the cladding region due to the lowering of the effective refractive index by the holes. Dr. Tanya Monro's research[27] used a computer simulation to demonstrate that the ordered arrangements of the holes were not necessary to get many of the properties of the PCF fibers. In fact a "random" arrangement of holes was shown by computer simulation to yield fibers with similar properties to the PCF's. It is clear that the incorporation of holes in the cladding region whether in an ordered pattern or a random pattern lowers the average effective index of the fiber and therefore provides an optical cladding to the fibers.

The air holes incorporated into the sapphire fiber lower the average effective index of the cladding region in a similar manner to that observed in holey silica fibers[27]. The term photonic crystal fiber is used to denote the ordered arrangement of holes in the fiber similar to that used in the literature.

2.2 Photonic Crystal Fibers

Photonic crystal fibers fall into two main categories: those that use index guiding via total internal reflection and those that guide light via a photonic band gap[28]. Index guiding usually consists of a solid core surrounded by a material with a refractive index less than that of the core. If the size and spacing of the "holes" in the fiber are controlled properly, a photonic band gap

fiber can be produced. If the size and/or spacing of the holes do not permit a photonic band gap to exist, the fiber can still guide light by lowering of the average effective index in the cladding region. The photonic band gap phenomenon will be discussed in greater detail in the next section.

Photonic crystal fibers (PCF), which belong to the class known as "microstructured optical fibers" (MOF) or "holey fibers," were first reported in the 1990's[29-31] and have been the subject of intensive research ever since. Most PCF's consist of a pure silica core surrounded by ordered longitudinal air holes in the cladding region. Many PCF structures have been proposed (mainly differing in the size, spacing, and number of air holes present in the cladding region), including hollow core PCFs. Photonic crystal fibers have ordered holes in which the holes occur in a regular or periodic pattern (giving rise to the term "crystal"), which extends along the length of the fiber. This stems from the fact that the fibers are drawn from preforms, which contain tubes that run the entire length of the preform. Recently, a new type of holey fiber, called the random hole optical fiber (RHOF), has been developed[32]. In this type of fiber, thousands of longitudinal holes, which surround the solid central optical core, are random in size, spatial location, and extent along the optical axis[33]. Both the ordered hole and random hole fibers have some interesting properties for sensing applications[34-38] as well as for potential fiber to the home applications[39].

Photonic crystal fibers or "ordered hole" fibers have generated a significant amount of interest due to the unique properties exhibited by these fibers including an extremely small core size, single mode guidance over a very large wavelength range, and guidance through a hollow core[32-

[35]. Many useful fibers and devices have been developed based upon these "ordered hole" PCF's. However, these are all based on silica fibers, which limit the maximum use temperature due to fiber crystallization, fiber reactions with the environment, or glass creep under stress. Photonic crystal fibers also have the capability to be endlessly single mode. This is due to the fact that the effective index contrast between the core and cladding decreases at smaller wavelengths[40].

2.3 Photonic Band Gap Fibers

As previously stated, if a periodic lattice that has the correct size and spacing of the holes is formed then a photonic band gap similar to the electrical band gap found in a semiconductor can be produced. This photonic band gap operates on the principle that the periodic arrangement of a material with a given refractive index difference between that of the background material will not allow electromagnetic waves of a certain range of wavelengths to be transmitted. Two types of photonic band gap fibers are currently known. They include the hollow core photonic band gap fiber as well as the solid core photonic band gap fiber. The solid core photonic band gap fiber will be discussed in greater detail in a later section. In the hollow core case, if one of the holes in the lattice is removed, this will confine a range of wavelengths from operating anywhere besides in this "defect"[30]. A photonic band gap will not, however, occur if the size and/or spacing of the holes are not in correct relation to the wavelength range of the injected light. In a one-dimensional photonic band gap, which is the simplest case, ordered structures with two different dielectric constants are periodically arranged. The incoming light reflects and refracts off the interfaces of the two materials, which overlap the beams of incoming light. This cancels out the incoming beams according to the lights wavelength and direction[30]. When a wavelength is inside the band gap, the wave partially reflects off each layer of the periodic structure. The

reflected waves reinforce one another since they are in-phase, which causes them to combine with the incident wave producing a standing wave, which cannot propagate through the material[40]. When a wavelength is outside the band gap, the reflected waves cancel each other due to a phase mismatch[40]. This slightly attenuates the light but still allows the light to be propagated through the material.

The main factors that affect the properties of photonic band gaps are dielectric contrast, the arrangement of the periodic elements, and the size and spacing of the periodic elements. In a 2D periodic structure it is possible to prevent light from propagating in any direction within the plane. A 2D periodic structure has both Transverse Electric (TE) and Transverse Magnetic (TM) modes of propagation. In a TE mode, the electric field is perpendicular to the direction of propagation whereas in a TM mode, the magnetic field is perpendicular to the direction of propagation. It is also possible that a 2D periodic structure will have a photonic band gap for one polarization but not for the other. In general, a large energy distribution contrast will give rise to a large band gap. A 2D photonic band plot for a fiber is very complex and is generally solved using a computer program. Photonic band gap fibers are attractive because they minimize loss and undesired nonlinearities because they have the ability to guide in air.

2.4 Modal Propagation

Intrinsic, extrinsic, and defect absorption are the three main mechanisms that cause absorption of the transmitted signal in fiber optics[41]. Intrinsic absorption is defined as the inherent material absorption for that given material and is caused by the absorption bands in the UV region and the atomic vibration bands in the near-IR. Intrinsic absorption in the UV region can occur when a

photon interacting with an electron in the valence band gets excited and is promoted to a higher energy level. The absorption in the near-IR stems from the vibrational frequency of the chemical bonds between the atoms in the material. This interaction also exists with the electromagnetic field of the optical signal and gives rise to a transfer of energy from the electromagnetic field to the chemical bond creating absorption. Extrinsic absorption is a result of impurity atoms in the fiber that are often transition metal ions interacting with OH^- ions. Many starting materials in the glass making processes have trace amounts of these transition metals in the range of less than 10 parts per billion. Defects in the glass composition also cause absorption. These include, but are not limited, to high-density clusters of atom groups, missing molecules, and oxygen defects. Defect absorption is generally small in relation to extrinsic and intrinsic effects.

The main cause of scattering loss in single crystal sapphire fibers is variations in diameter of the fiber9. Heating power fluctuations or the source rod feed rate can cause the diameter variations during the production stage. Small variations in core diameter allow power to couple into higher order modes giving rise to scattering losses[42].

2.5 Random Hole Optical Fibers

Random hole optical fibers (RHOF) are a new type of fiber structure in contrast to the ordered holes present in the microstructure optical fiber (MOF) or the photonic crystal fiber (which is a subset of the MOFs). The name originates from the fact that the "holes" in the fiber are randomly located in the spatial domain, and can be controlled to sizes in the micron to nanometer size range by controlling the conditions of fabrication. The RHOFs use thousands of air holes to confine the light to the core of the fiber through an average index guiding mechanism. One of

the important aspects of the air holes is the fact that they can allow access to the interior of the fiber while still maintaining the modal properties of the fiber[37]. This can be very important in sensing applications. In addition, since the structures can be produced in pure silica (no dopants required), the high temperature capabilities are improved relative to conventional doped fibers. Current telecommunication fibers incorporate dopants into the silica glass structure to change the refractive index of the silica. These doped regions are not robust in high temperature applications because their dopants can diffuse from the core to the cladding layers or vice versa, which leads to changes in their modal properties.

The continual work on the characterization and fabrication of ordered hole fibers can be seen throughout the literature[27-31] beginning with the work of Knight, Birks, Russell and Atkin. Ordered hole fibers are oriented in a preform which is comprised of an array of stacked longitudinal tubes. These longitudinal tubes are then carefully drawn to produce an ordered arrangement of holes in the finished fiber.

In contrast to the ordered hole fibers, the random hole fibers are created by producing holes *in-situ* during the fiber drawing stage. This produces a vast number of "holes", which can be controlled to have diameters that range from a few nanometers to the micron size range, by controlling the conditions of the fiber drawing process and the preform characteristics. Like the ordered hole fibers, RHOFs are composed of longitudinal holes, which run parallel to the fiber axis. The large difference between the refractive index of air and silica glass along with the numerous possibilities regarding the arrangement of these air holes may allow RHOFs to be used in a wide range of applications.

2.6 Solid Core Photonic Band Gap Fibers

Solid core photonic band gap fibers (SC-PBG) differ from hollow core photonic band gap fibers as they are composed of a solid, homogeneous core and surrounded by a periodic lattice of higher refractive index inclusions. These higher index layers can be concentric in composition, producing a 1D solid core photonic band gap fiber, also called a Bragg fiber[43]. Light is guided in a solid core photonic band gap fiber by a photonic band-gap effect produced in the cladding where the average cladding index is higher than that of the core's index. Total internal reflection using Snell's law would argue that light would be guided in the higher index regions. Solid core photonic band gap fibers operate under the same theory as hollow core photonic band gap fibers where having the correct size and spacing between high index inclusions would give a full 2D band-gap effect[45]. The optical properties of SC-PBG fibers depend heavily on the diameter d of the higher refractive index doped rods (generally doped with Ge), the ratio of d/Λ, and the wavelength of excitation[45]. The pitch, Λ, is the distance between the centers of the high-index inclusions. In the solid core case, the defect in the periodic array is the absence of one or multiple high index inclusions.

Solid core photonic band gap fibers are of interest because unlike hollow-core photonic band gap fibers, they are easier to fabricate and splice due to their "hole-free" nature, and can be doped as in step index optical fibers. Solid core photonic band gap fibers also have the added advantage of being free of surface modes, which are causes of loss in many hollow core photonic band gap fiber designs[44]. They are being investigated for use in the telecommunications industry because of their dispersive and spectral properties around the 1550 nm wavelength[45]. In solid core

photonic band gap fibers, confinement losses exist due to the fact that there are only a finite amount of high index inclusions in the cladding.

2.7 Fiber Optic Modeling

The fiber optic modeling in this work consists of using Comsol Multiphysics and MIT photonic Bands (MPB). Comsol Multiphysics is more useful for analyzing losses and examining different modes present in a fiber while MPB is focused on understanding the band gaps that occur in different material structures. The objective of the modeling work is to examine how a fiber design will perform without having to build the fiber.

Finite element analysis (FEA) can be a very useful tool for fiber optic design. Comsol Multiphysics uses high-order vectorial elements composed of both an automatic and iterative grid refinement calculator. This allows for optimum error estimation during the solving process. The models in this thesis require complex meshing to render the smaller materials domains with high accuracy. Comsol Multiphysics requires the user to first select the geometry and axes of the fiber in question. During this step, the size and shape of the core and cladding layers are chosen. Next, the material properties of the fiber are chosen. The main variables include the refractive index (both real and the imaginary part), electric conductivity, relative permittivity, and relative permeability values for the core and cladding. The electromagnetic waves heading is chosen for this RF mode and the modal analysis then presumes the wave propagates in the z-direction. This allows the user to select the perpendicular hybrid mode wave using transversal fields, which will give the modal solutions. The electric field of this wave is given[46] in Equation 2:

$$\mathbf{E}(x,y,z,t) = \mathbf{E}(x,y) \exp\,[j(\omega t - \beta z)] \tag{2}$$

with ω being the angular frequency, t is time, and β being the propagation constant. The boundary condition on the outside of the cladding layer is set to $n \times \mathbf{E} = \mathbf{0}$. Now using the Helmholtz equation, an eigenvalue equation in terms of the electric field can be written as Equation 3:

$$\nabla \times (n^{-2}\nabla \times \mathbf{E}) - k_0{}^2\mathbf{E} = \mathbf{0}. \tag{3}$$

Equation 3 is solved for the effective refractive index value $n_{eff} = \beta/k_0$, which gives the eigenvalue, with k_0 being the wavenumber. At this point, it is important to setup a perfectly matched layer (PML). The PML layer absorbs all outgoing waves (typically leaky eigenmodes), which radiate toward the outer cladding layer. The PML is reflectionless for any frequency, thus absorbing all outgoing radiation[47]. Maxwell's equation for a vector wave with an anisotropic PML is defined as:

$$\nabla \times ([\boldsymbol{S}]^{-1}\nabla \times \boldsymbol{E}) - k_0{}^2 n^2 [\boldsymbol{S}]\boldsymbol{E} = 0 \tag{4}$$

where $\boldsymbol{S}$ is the Poynting vector, $\boldsymbol{E}$ is the electric field, $\boldsymbol{k_0}$ is the propagation constant, and n is the refractive index of the medium that contains the PML. The electromagnetic wave heading is chosen for this RF mode and the modal analysis then presumes the wave will propagate in the z-direction. This allows the user to select the perpendicular hybrid mode wave using transversal

fields, which will give the modal solutions. This equation is obtained from the uniformity of the electric field, which gives us:

$$\boldsymbol{E}\ (x, y, z) = \boldsymbol{e}(x, y)\exp(-\gamma z) \tag{5}$$

with γ being the propagation constant. A perfect electrical conductor (PEC) is the boundary condition that is generally set for the region inside the PML when solving for most fibers. Unlike field continuity conditions, a PEC cannot sustain internal fields[47] and thus $\hat{n}\times\mathbf{E} = 0$, where $\hat{n}$ is the unit vector normal to the interface between two mediums and **E** is the electric field intensity in volts/meter. All regions inside of the PEC are set to a continuity boundary condition which describes the source free interface between two mediums[47] given by Equation 6:

$$\hat{n} \times (\boldsymbol{E_1} - \boldsymbol{E_2}) = 0 \tag{6}$$

where $\boldsymbol{E_1}$ and $\boldsymbol{E_2}$ are the electric field intensities at both mediums.

Confinement loss, L_c, is a commonly used metric for measuring how an optically modeled fiber will perform under optimal operating conditions. It is directly related to the imaginary portion of the propagation constant[48], γ, through the equation:

$$L_c = 8.686 * \alpha \tag{7}$$

where α is the attenuation constant. This equation gives the loss[49] in units of dB/m. The propagation constant is defined as:

$$\gamma = \alpha + j\beta \tag{8}$$

where β is the phase constant. Another important metric that Comsol Multiphysics can calculate for a given mode is the power flow time average, Po*i*av, which is equivalent to:

$$\text{Po}i\text{av} = \tfrac{1}{2} * \text{Re}(\mathbf{E} \times \mathbf{H}^*)i \tag{9}$$

which gives the z_i component in the direction of propagation (into the fiber). This shows that at any point in an electromagnetic field, the vector in Equation 9 can be interpreted in terms of power flow for a specific direction.

Before these equations are computed, the mesh of the fiber's geometry must be set up. Here a precise mesh using quadrilateral or triangular grid is necessary due to the complicated fiber designs to obtain optimal accuracy. The accuracy of the output data is directly correlated to how precise the mesh is for each fiber structure. The mesh is limited by the memory of the computer as the degrees of freedom increase with a decrease in mesh size. After the mesh is chosen, the modal analysis of the fiber begins. The user specifies the desired number of modes to search for and which effective index to look around after specifying the free space wavelength (which is the wavelength at which the modes propagating in the fiber are being tested).

These types of RF modal propagation problems are generally solved with a direct linear system solver (UMFPACK) so that Maxwell's equations in the FEM discretization can be computed without error. Comsol Multiphysics also features the Multifrontal Massively Parallel sparse direct Solver (MUMPS) solver, which allows for parallel computing on a quad core computer to decrease computation time. Comsol assumes the 2-D slice of the fiber design to continue along the z-direction. In real fibers there will be perturbations in the fiber structure along the z-direction which explains why the optical losses seen in Comsol Multiphysics modeling are always less than that of an actual fiber.

2.8 MIT Photonic Bands

The MIT Photonic Bands program[40] (MPB) allows users to compute the eigenstates and eigenvalues of Maxwell's equations for plane waves in the frequency domain. This solver examines the frequencies of both a periodic or non-periodic system using Equation 10:

$$\left[(i\mathbf{k}+\nabla)\times\frac{1}{\varepsilon(\mathbf{r})}(i\mathbf{k}+\nabla)\times\right]\mathbf{u}_{\mathbf{k}}(\mathbf{r})=\hat{\Theta}_{\mathbf{k}}\mathbf{u}_{\mathbf{k}}(\mathbf{r})=\frac{\omega(\mathbf{k})^2}{c^2}\mathbf{u}_{\mathbf{k}}(\mathbf{r}), \tag{10}$$

where $\mathbf{u}_k(\mathbf{r})$ is the Bloch envelope of the magnetic field, $\mathbf{k}$ is the Bloch wave vector, ε is the dielectric constant of the material, c is the speed of light, $\mathbf{r}$ is the cartesian position vector, Θ is the differential Hermitian operator that depends on $\mathbf{k}$ (where $\Theta=(ik+\nabla)\times 1\,\varepsilon(r)(ik+\nabla)$), and ω is the angular frequency. The solution to Equation 10 above as a function of $\mathbf{k}$ gives the resultant band structure of the fiber design being analyzed. A Bloch envelope is composed of

wavefunctions of particles that are in a periodic potential. The Magnetic field is defined as Equation 11:

$$\mathbf{H}_k = e^{i\mathbf{k}\cdot\mathbf{r}}\mathbf{u}_k(\mathbf{r}), \tag{11}$$

with $\mathbf{u}_k(\mathbf{r})$ fulfilling the transversality constraint given by Equation 12.

$$(i\mathbf{k} + \nabla) \bullet \mathbf{u}_k = 0 \tag{12}$$

When the Bloch envelope is periodic, only a finite unit cell of the structure must be solved. The band structure of the fiber under consideration is given by solving the above equation as a function of $\mathbf{k}$. This eigenequation is then discretized with N degrees of freedom (dof) using plane wave expansion. This gives a finite generalized eigenproblem in the form $Ax = \omega^2 Bx$ where x is the eigenvector and A and B are $N \times N$ Hermitian matrices, with B being positive definite preserved by the Galerkin discretization[40]. MPB then uses iterative methods to solve the above equations. Iterative methods are defined by computing a small number of the eigenvalues and eigenvectors by guessing a value for x and then using an iterative approach to improve the initial guess. This enables MPB to quickly converge on a solution for a true eigenvector. When the fiber under study is not periodic, MBP uses supercell approximations. Supercell approximations consist of a periodic boundary condition with a large cell around the localized mode so the boundaries become irrelevant to the problem.

Fibers are modeled as a 2D structure, being periodic in the x and y planes, and homogeneous in the z plane. A 2D fiber classifies the two types of electromagnetic waves, which propagate in the z-direction along the fiber as transverse electric (TE) and transverse magnetic (TM). Transverse electric modes will have their electric field vector in the x and y plane and their magnetic field vector perpendicular to the z plane whereas transverse magnetic modes will have their electric field vector perpendicular to the z plane and their magnetic field vector in the x and y plane. The two polarizations of light enable reflections in any direction in the xy plane. The main structure of interest in this thesis is known as the hexagonal geometry. A hexagonal lattice, as seen in Figure 2.5 has a periodicity a, with $a_1 = a_2$. The lattice parameter a is also known as the pitch or periodicity, sometimes denoted by Λ.

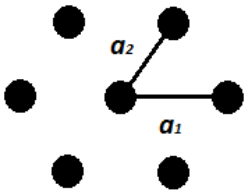

Figure 2.5 Hexagonal crystal lattice structure

The reciprocal space for the irreducible Brillouin zone is a more common way of analyzing photonic band gaps because all other points in the reciprocal space can be obtained from the Γ, M, and K points through rotational symmetry as seen in Figure 2.6. The outlined Brillouin zone for the hexagonal structure has a unit lattice equivalent to $b_1 = b_2 = \frac{4*\pi}{a*\sqrt{3}}$.

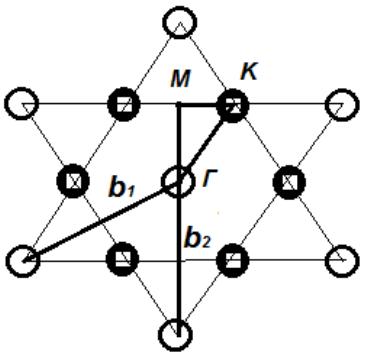

Figure 2.6 Reciprocal lattice for the hexagonal crystal lattice with the Brillouin zone shown by the *M*, *K*, and *Γ* points

MIT Photonic Bands software is based off Maxwell's equations, which are scale invariant. This allows the user to scale to a highlighted frequency range by multiplying lattice constant *a* by *x*, which in turn divides the frequency by *x*. In order to convert the frequency eigenvalues given by the software which are in units of c/a, (with *c* being the speed of light, and *a* being the spacing in-between rods or air holes) we find the wavelength corresponds to *a* divided by the frequency eigenvalue. By definition, frequency $f = c/\lambda$ and because every parameter in the software is normalized to the auxiliary lattice parameter (a), we multiply and divide by *a* on the right hand side of the Equation 13:

$$f = c * \frac{a}{a} * \lambda \;=\; \left(\frac{c}{a}\right) * \left(\frac{a}{\lambda}\right) \tag{13}$$

The units on the right hand side show that the term a/λ is a unit-less term and hence the representation of frequency is in multiples of a/λ. The band midgap point (f_m), which is the center frequency of the middle of a band gap on the frequency scale, is then equated to the term a/λ through the Equation 14.

$$f_m = a/\lambda \quad (14)$$

Lambda, λ (the wavelength of operation) is then set as L_1 with which the auxiliary lattice parameter (a) can be obtained. This is shown through Equation 15:

$$a = f_m * L_1 \quad (15)$$

and now using this parameter, we can find out the actual physical parameters (for example when $r/a = 0.5 \Rightarrow r = 0.5 * f_m * L_1$).

2.9 White light interferometry

Interferometry is defined when two or more waves of the same frequency combine and the phase between these two waves is changed, the intensity of the resultant wave will oscillate[50]. When the two waves have interfered from two partially reflective surfaces placed close together, as seen in Figure 2.7 below[51] that beam A_2 will travel a longer distance than beam A_1.

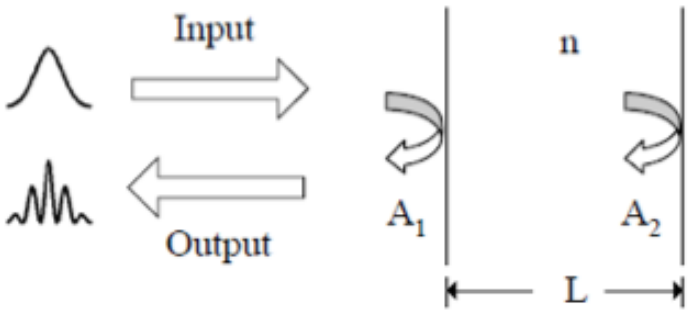

Figure 2.7 Fabry-Perot interferometer setup used from reference [51] illustrated under "Fair Use" copyright guidelines

As shown in Figure 2.7 above, there are two reflective surfaces separated by a cavity of length L, with a refractive index of n. The input light will generate two reflections, one from each surface with amplitudes A_1 and A_2, which interfere to produce the total reflected light intensity. The phase of the light in a free-space virtual material is determined by the optical path difference (OPD), which is defined as:

$$OPD = 2*n*L \tag{16}$$

with a corresponding time delay, Δt of:

$$\Delta t = \frac{(2*n*L)}{c} = \frac{OPD}{c} \tag{17}$$

with c being the speed of light and n being the materials index of refraction. By dividing OPD by an integer of wavelength iterations, a wavelength that interferes with the interferometer can be realized. Partial cycles will create a phase mismatch that will cause destructive interference. When one cycle is scaled by 2π, the constructive interference will be zero and the destructive

interference will be π. The power of the optical beam however is at a maximum during constructive interference and at a minimum during destructive interference. This oscillatory cosine behavior is shown as the electric field amplitude A_2 oscillates versus A_1 in Equation 18 below:

$$I(\lambda) = A_1^2 + A_2^2 - 2 * A_1 A_2 * \cos\left(\frac{2\pi * OPD}{\lambda} + \varphi_0\right) \quad (18)$$

where I is the light intensity as a function of wavelength, and φ_0 is the phase value. When there is a change in temperature or pressure, the cavity length will change, thus modifying $I(\lambda)$. An optimal cavity length can be determined through various types of demodulation, but this is an entirely different subject that is well covered in Zhu[51] et al. The "fringes" are defined as the oscillations in the intensity as a result of the interference. From this, we can find the visibility, which is the ratio of the amplitude of these oscillations to the sum of the powers of the individual waves[52]. Like other more conventional interferometers, white light interferometry is immune to like source power drift. It also has a high resolution, large dynamic range, and a variety of potential applications[53-56].

2.10 Gas Sensing

Gaseous emission monitoring has become more prevalent in recent years due to the rise of many industrial processes. The need for monitoring gases like CO, CO_2, hydrocarbons, NH_3, and NO_x makes the case for a fast, stable, highly sensitive, and high temperature sensor. Extensive research has been performed to develop sapphire fiber-based sensors. Various sensors including intrinsic and extrinsic interferometers, polarimetric devices, and birefringence-balanced lead-

insensitive sensors have been demonstrated for measurement of various physical parameters at high temperatures.

An evanescent wave[57] has an intensity that exponentially decays with distance from the core towards the cladding and has a characteristic penetration depth of 50-100 nm. This evanescent wave occurs from the reflection with the cladding layer of the fiber which is due to the input light having an angle greater than that of the critical angle. This happens because the electric and magnetic fields cannot be discontinuous at a boundary. The critical angle is defined as Equation 19:

$$\Theta_c = \arcsin (n_2/n_1) \tag{19}$$

where n_1 is the core refractive index and n_2 is the cladding refractive index with $n_2 < n_1$. The propagation of light in two differing materials behaves according to Snell's law, which is stated in Equation 20:

$$n_1 \sin \theta_1 = n_2 \sin \theta_2 \tag{20}$$

where θ_1 is the angle from the normal plane of incidence and θ_2 is the angle from the refracted wave. The evanescent wave is only produced when the crystal has a higher refractive index than that surrounding the fiber. Evanescent fields are created when light is reflected at a boundary under total internal reflection. The higher the mode that is traveling in the fiber, the more the

evanescent wave travels into the cladding region. The light in the cladding region can then interact with the gaseous environment when the cladding layer is porous or completely removed. When a light ray, incident on a dielectric boundary at an angle θ, experiences total internal reflection, an evanescent field is produced. The chemical absorption can be described using the complex refractive index for these types of fibers. In this case, the electric field, E of the electromagnetic wave traveling through the chemical species is described using the equation:

$$E=E_0*\exp[j(\omega t-\alpha l)] \tag{21}$$

where l (cm) is the length of the region containing the chemical species being sensed, ω is the angular frequency, t is time, and α being the propagation constant given by the equation:

$$B=k_0*n=2\pi*(n_r - jk_x)/ \lambda \tag{22}$$

where k_0 is the wavenumber, n_r is the real part of the refractive index, and k_x being the imaginary part of the refractive index. The exponential decay of this evanescent field is given by the equation:

$$E = E_0 * exp\left(-\frac{x}{d_p}\right) \tag{23}$$

with the penetration depth d_p being:

$$d_p = \frac{\lambda}{2\pi * sqrt\left(n_2{}^2 * (sin(\theta))^2 - (n_1)^2\right)} \tag{24}$$

where E_0 is the field amplitude at the dielectric boundary. Thus, the attenuation of the guided light is dependent on the how much power is carried out by the mode outside the core region. The chemical concentration *C*, (a fraction of percentage) also controls the output intensity *I*, by the equation:

$$I = I_0 * exp[-(r * \sigma_m) * Cl] \quad (25)$$

where I_0 equals the intensity of the incident radiation, r is the relative sensitivity of the attenuation coefficient, and σ_m is the molar absorption coefficient in units of $at^{-1}cm^{-1}$. Absorption strength is related to the chemical concentration C, through the Beer-Lambert law, which is defined by the equation:

$$I = I_0 * exp(-2\alpha_0/C) \quad (26)$$

with α_0 being the absorption coefficient of the gas.

Gas sensing is dependent on mode distribution so a multimode fiber is disadvantaged because of launching conditions and external effects. The presence of a gas during a sweep of wavelength ranges will appear to be lossy at specific characteristic wavelengths based on the gaseous species that is present. Multiple gases could technically be detected using the same fiber over a given wavelength range. Other common evanescent gas sensing fibers include the D-shaped fiber, which allows the core continuous contact with the gas present along the length of the entire fiber.

Hollow core waveguides are another type of gas sensor that offer significant advantages over traditional evanescent field gas sensing. The light guiding mechanism in the hollow wave guide is a function of how strong the reflections from the incident light are on the interface of the surface of the waveguide. The higher the reflection at this interface, the higher the transmission of incident light. Hollow core waveguides can have a higher sensitivity due to the majority of the incident light propagating in the area filled with the gas that is being sensed. This allows the incident light to directly interact with the gas molecules. Other advantages of this type of gas sensing include a short response time and long-term stabilization.

3. Fiber Modeling

3.1 Random Hole Optical Fiber

3.1.1 Experimental

Accurate numerical modeling is essential for optimal fiber design. Comsol Multiphysics uses high-order vectorial elements along with an automatic and iterative grid refinement calculator for optimum error estimation. This process is a necessity when accurate silica-air interfaces need to be sampled during the meshing stage. The silica-air interface puts a large burden on the computer's memory because of fast far-field variations and the fact that the electric field's normal component will become discontinuous.

Random hole optical fibers (RHOF) are very difficult to replicate in FEM software due to the various diameters and shapes of the air holes. In order to get an accurate structure when

modeling using a FEM solver, Matlab must be used. Matlab has the capability of importing an SEM micrograph and then converting it to grayscale. After import and conversion, Matlab can recognize the difference in pixels of the imported image. It is then a matter of exporting the file from Matlab into Comsol Multiphysics and changing the scale to match the original SEM data.

Figure 3.1 shown below is an SEM cross-section of the RHOF that has been created using the experimental fabrication process as described from Pickrell[33] et al. The fiber has a 108.5 μm outer diameter with an inner diameter at 64.6 μm. The core region is approximately 20.3 μm in diameter; the imported SEM image consists of thousands of air holes ranging in size from less than 100 nm to above 1 μm. The air holes non-uniform shape will also alter the birefringence. All models were examined at the free space wavelength λ_0 =1550 nm.

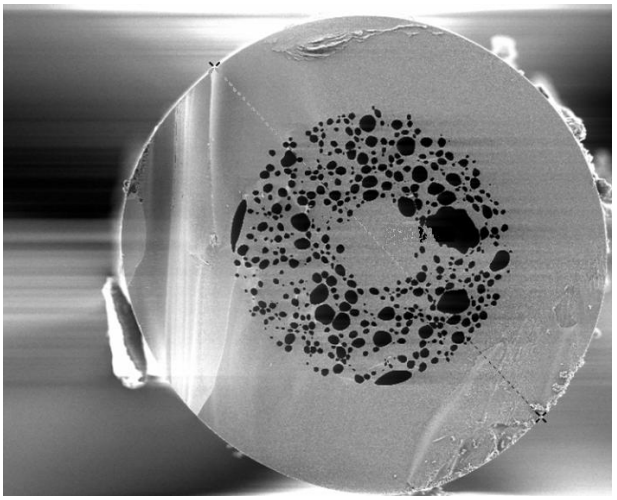

Figure 3.1 SEM cross section of Random Hole Optical Fiber

3.1.2 Fem Analysis

Once the SEM image in Figure 3.1 has been successfully imported into Comsol Multiphysics, the next step is to mesh the structure. The precision of the data directly relates to how refined the mesh can be. The only limitation of the mesh is the memory of the computer that will be solving the boundary equations. Figure 3.2 below, shows a mesh consisting of 288892 elements run on a 4 Gb Macintosh.

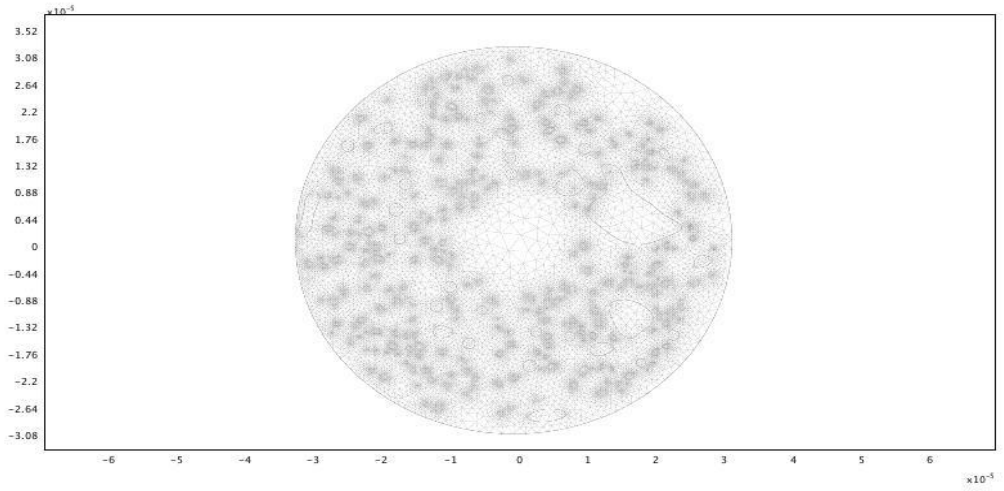

Figure 3.2 Mesh consisting of 288892 elements of the imported SEM shown in Figure 3.1 with the x and y axes in (m)

The outer diameter of the fiber is set as a cylindrical perfectly matched layer (PML), which utilizes a reflectionless outer layer as described in Section 2.7 Fiber Optic Modeling. No modes were expected in this region, and therefore, the outer layer has been omitted. This saved valuable memory space during the meshing and solving stages. As shown in Figure 3.1, the actual outer boundary of the fiber is composed of a silica layer which is fused to the random air holes.

When the mesh is complete, the boundary conditions must be met. Continuity was set inside the cylindrical PML while a perfect electrical conductor was set to the outer edge. The air holes were then set to n=1.00 and the silica glass was set to n=1.45. Comsol is then solved using a direct linear equation solver (UMFPACK) near the effective mode index of the silica glass (1.449). Figure 3.3 shows the resultant fundamental hybrid mode for the given SEM micrograph in Figure 3.1. This is as expected for the power flow to be concentrated directly in the center of the core. The power flow time average z-component is at a maximum (in red) at 1.074×10^{17} W/m^2 and at a minimum (in blue) at 3.92×10^{-5} W/m^2.

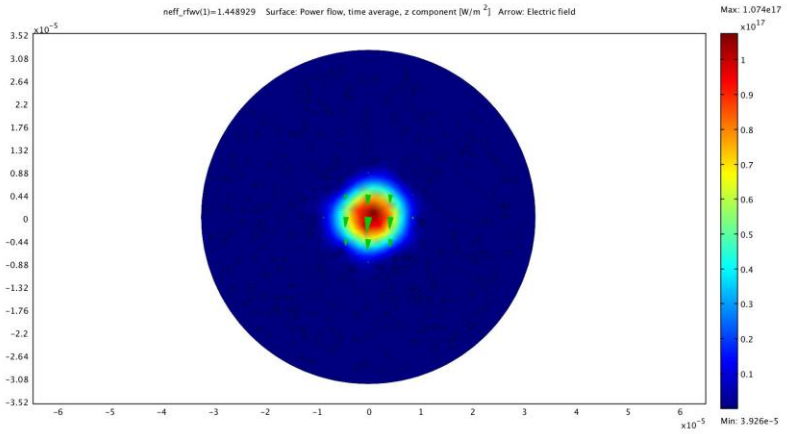

Figure 3.3 Transversal profile of the time-averaged power flow (W/m^2) in the z-direction with the x and y axes in (m)

Figure 3.4, which is shown below, is a magnified picture of Figure 3.3; in order to make the electric field (green cones) more visible. The electric field in Figure 3.5, also shown below,

gives the relative height (3D) of the power flow time average z-component. This relative height is proportional the optical intensity $|\mathbf{E}|^2$.

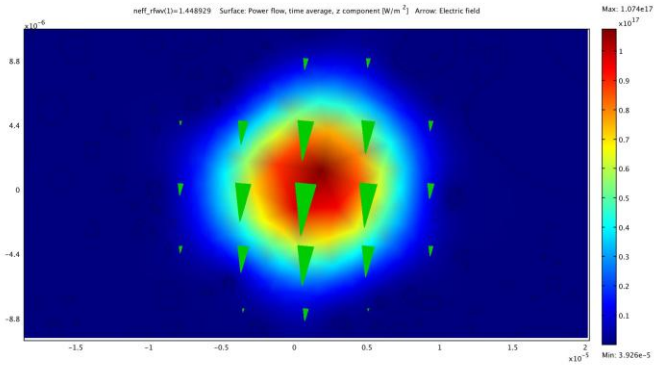

Figure 3.4 Fundamental mode of the fiber (magnified view) with the x and y axes in (m)

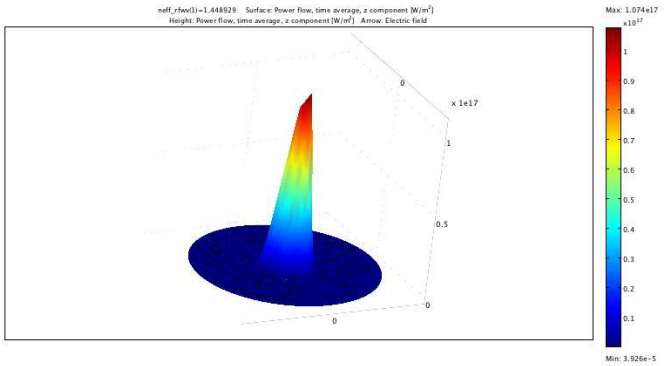

Figure 3.5 Power flow (W/m^2) 3D view with the x and y axes in (m)

Figure 3.6, as shown below, gives the various LP_{11} modes that also propagate in this multimode fiber.

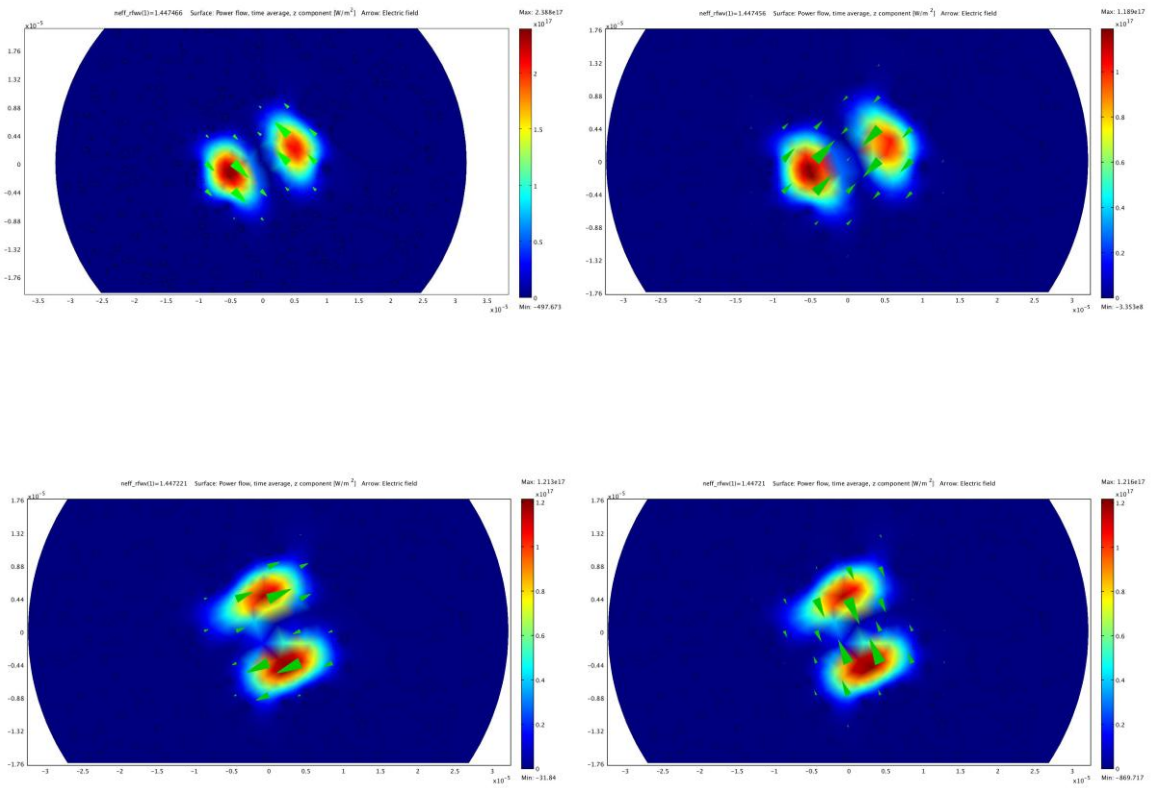

Figure 3.6 LP_{11} modes of the fiber near n=1.4495 (magnified view) clockwise from top left y-polarized even $\psi=A_0J_1(ur)\cos\varphi a_y$, x-polarized even $\psi=A_0J_1(ur)\cos\varphi a_x$, x-polarized odd $\psi=A_0J_1(ur)\sin\varphi a_z$, y-polarized odd $\psi=A_0J_1(ur)\sin\varphi a_y$ with the x and y axes in (m)

In summary, this section examined a modeling study of a RHOF using the Comsol Multiphysics modeling program. The importation process of an SEM cross-section simplifies the modeling process and provides a great degree of accuracy in the image translation using Comsol Multiphysics with Matlab. This process allows the user to easily modify the current air hole arrangement in order to further analyze any changes that can or will be made in the future. Much work has been done in the area of RHOF's, but this is the first time that a RHOF has been modeled in a FEM environment. Finite element modeling allows for the examination of how the porous refractive index of the cladding region is effecting the modal propagation of light through

the fiber. Importation of a specific 2D cross section from an image into Matlab and then into Comsol allows for the most accurate representation of the actual fiber structure compared to building a representation of the structure.

3.2 Solid Core Photonic Band-Gap Fibers

3.2.1 Experimental

Accurate numerical modeling is essential for optimal fiber design. Comsol Multiphysics uses high-order vectorial elements along with an automatic and iterative grid refinement calculator for optimum error estimation. This process is a necessity when accurate small interfaces need to be sampled during the meshing stage. The nature of the small material interface puts a large burden on the computer's memory because of fast far-field variations and the fact that the electric field's normal component will become discontinuous. This experiment uses a direct linear system solver (UMFPACK) for its modal analysis[58].

The initial model of the SC-PBG fiber used in this work was replicated from a previously published paper[59] to validate the working model. The fiber has seven rings of Ge doped silica rods with a refractive index of 1.48. The doping process assumes a parabolic refractive index range of 3.0E-2 from the center of the Ge doped rod to the outer edge of the rod. This fiber maintains a d/Λ ratio equal to 0.683 with an outer PML diameter of 1.368E-4 m and an inner diameter at 1.216E-4 m. This gives a diameter d of 300 μm and pitch Λ of 15.2 μm. The core region is approximately 20 μm in diameter. All models were examined at the free space wavelength $\lambda_0 = 1550$ nm. When no defects are present in this fiber, Comsol Multiphysics gives

a confinement loss $L_c = 0.006968$ dB/km. The loss with no defects can be seen over a wide range of free space wavelengths as seen in Figure 3.7 below.

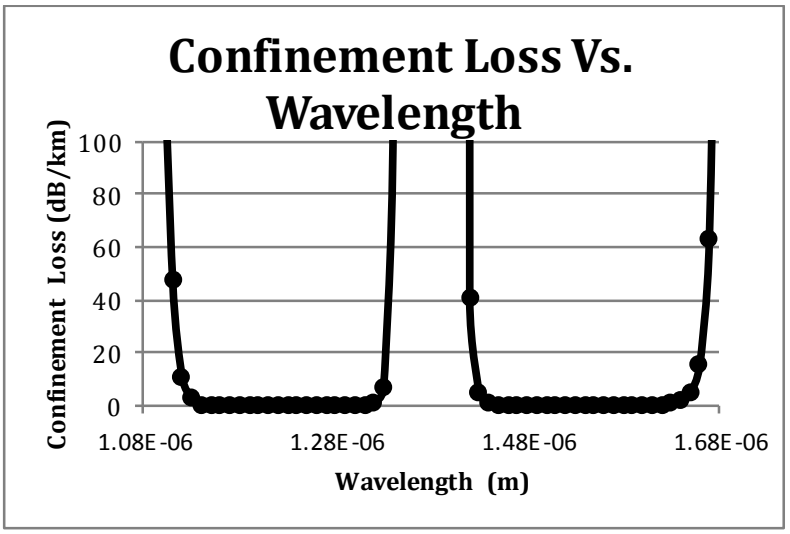

Figure 3.7 2D band structure of the Solid Core Photonic Band Gap Fiber

The objective of this section was to see how the confinement loss of solid core photonic band gap fiber is affected when a defect is present. The results should follow the anti-resonant reflecting optical waveguide (ARROW) model[60], which states that the closer a defect is to the core region, the greater the confinement loss will be. An air hole defect was thus added and its diameter and position was changed in order to observe how this would affect the confinement loss of the fundamental mode (LP_{01}). The air hole defect starts with a radius of 0.2595 μm and increases by 0.2595 μm each time, until it reaches a final value of 2.076 μm. The x positioning stays constant at 0 while the y positioning changes starting from (0,0) and increasing by 1.86 μm until the y position reaches a value of 18.6 μm. An example of this can be seen below in Figure 3.8.

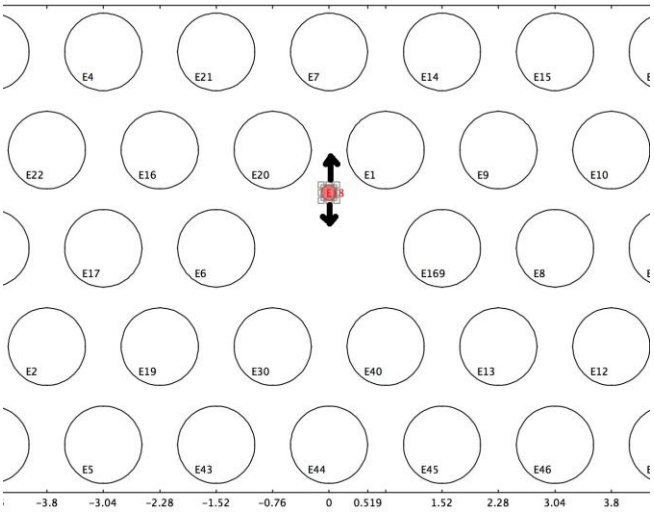

Figure 3.8 A 2D model of an air hole defect (as seen in red) with the x and y axes in (m). The defect's diameter and y position was modified to examine its effect on confinement loss. The numbered circles are the high index Ge-doped rods.

3.2.2 Fem Analysis

Again, the precision of the data directly relates to how refined the mesh can be. The only limitation of the mesh is the memory of the computer that will be solving the boundary equations. Figure 3.9 below shows a mesh consisting of 288892 elements run on a 4Gb Macintosh.

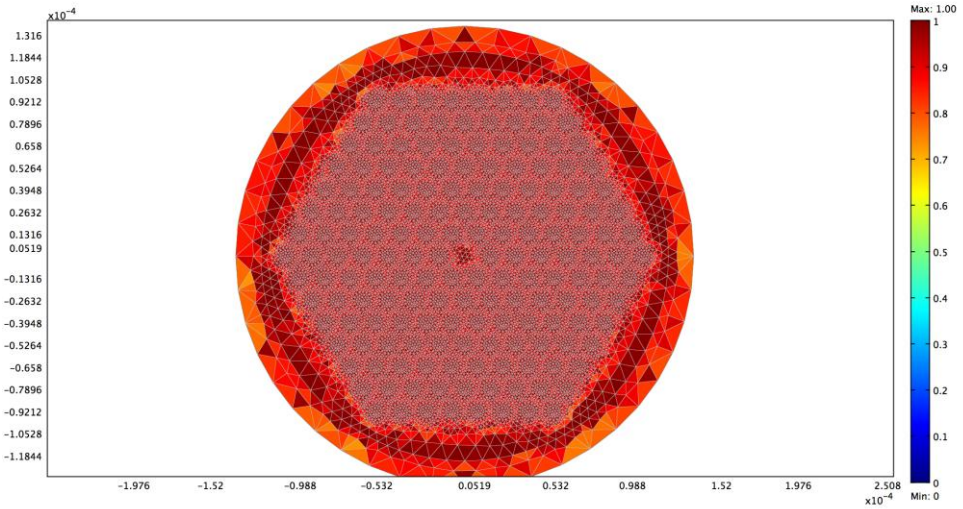

Figure 3.9 2D Comsol model of the meshing accuracy of the Solid Core Photonic Band Gap Fiber with the x and y axes in (m). The rainbow colored y-axis (at right) demonstrates the accuracy of the mesh.

The outer diameter of the fiber is set as a cylindrical perfectly matched layer (PML), which utilizes a reflectionless outer layer. This is used in our research in order to absorb all outgoing waves[47] as discussed in Section 2.7 Fiber Optic Modeling.

When the mesh is complete, the boundary conditions must be met. Continuity was set inside the cylindrical PML while a perfect electrical conductor was set to the outer edge. The Ge doped silica rods were then set to n=1.48 with a parabolic refractive index range of 3.0E-2 and the silica glass was set to n=1.45. Comsol is then solved using a direct linear equation solver (UMFPACK) near the effective mode index of the silica glass. Figure 3.10, shown below, is the resultant fundamental hybrid mode for the SC-PBG with no defect. This is as expected for the power flow to be concentrated directly in the center of the core.

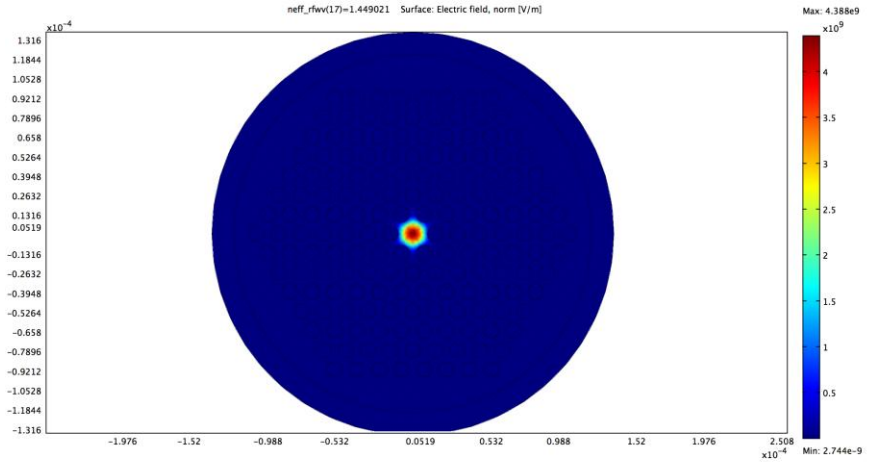

Figure 3.10 Transversal profile of the time-averaged power flow (W/m^2) for the LP_{01} mode in the z direction with the x and y axes in (m)

As stated in the Experimental Section 3.2.1 above, an air hole defect was added and its diameter and position were changed in order to observe how this would affect the confinement loss of the fundamental mode (LP_{01}). The results for these changes can be viewed below in Figure 3.11 and 3.12. Figure 3.11 shows the confinement loss versus the radius of the air hole defect with the numbers in the legend indicating the distance from the core in (m). Figure 3.12 shows the confinement loss versus distance from the core in the y-axis with the numbers in the legend indicating the radius of the air hole defect. These results are for the fundamental mode (LP_{01}) with a free space wavelength of 1.55 μm.

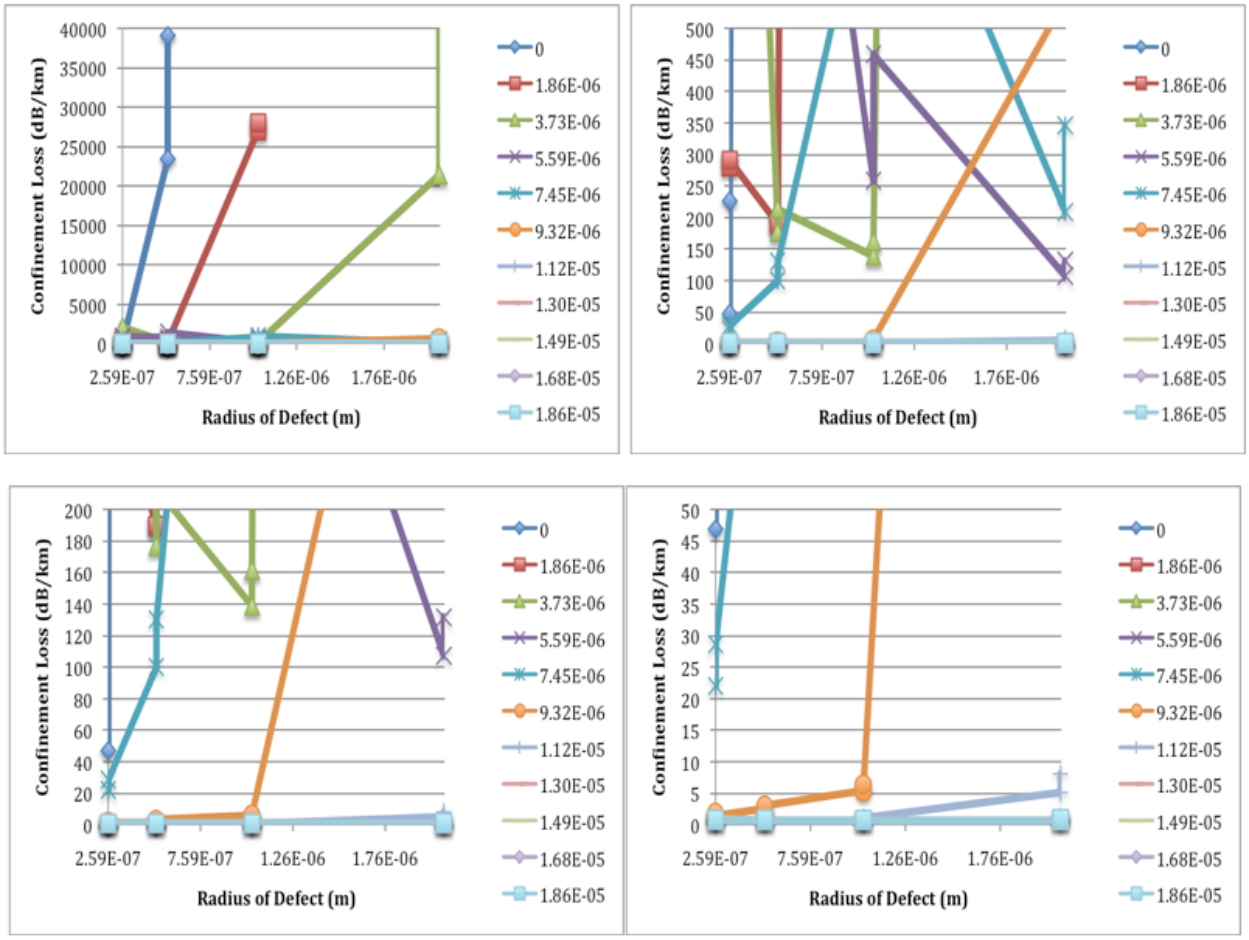

Figure 3.11 Confinement loss (dB/km) vs. radius of air hole defect (m)

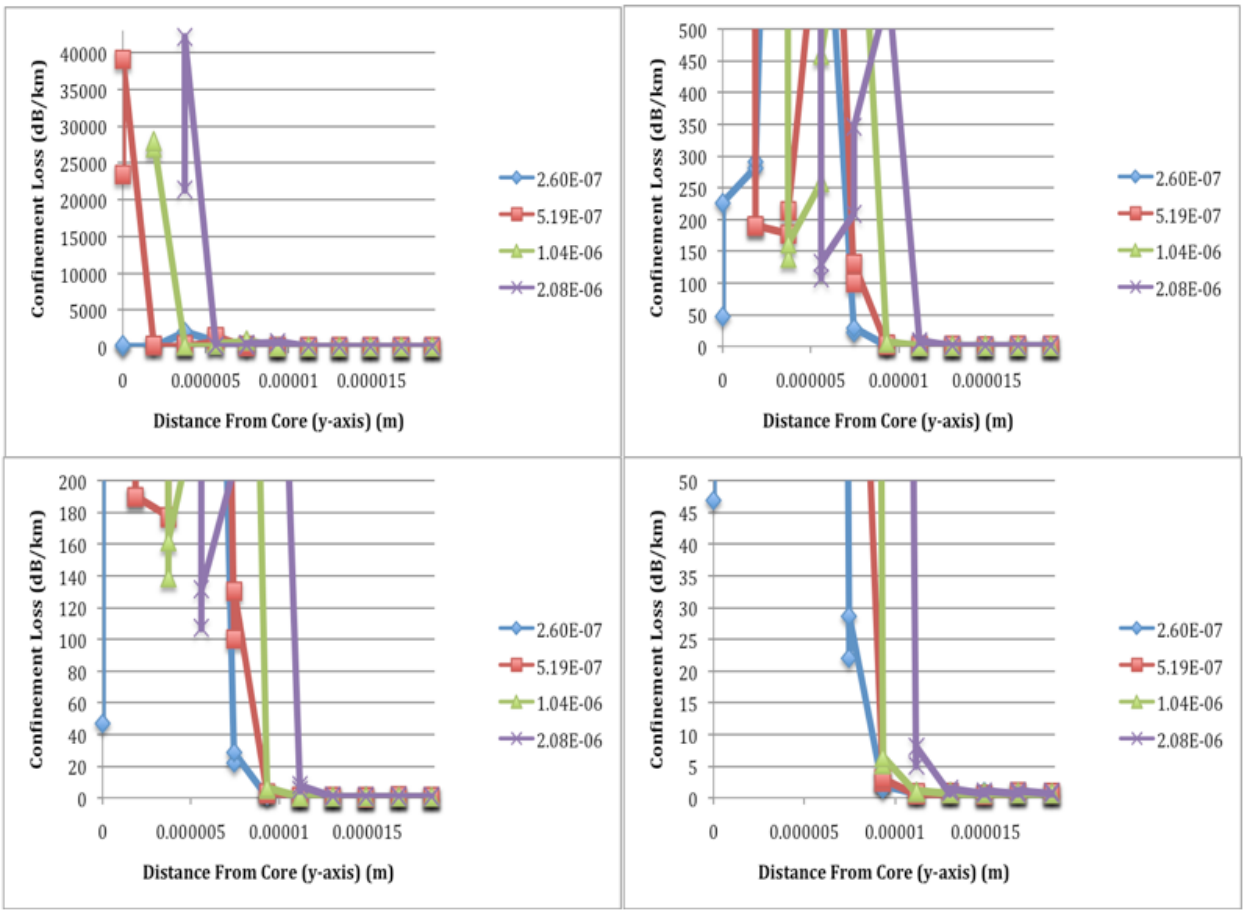

Figure 3.12 Confinement loss (dB/km) vs. distance from core (y-axis) (m)

In summary, this section examines the addition of an air hole defect in a solid core photonic band-gap fiber (SC-PBG) using the Comsol Multiphysics modeling program. The characteristics of the defect were modified in terms of spatial location in relation to the core and the size of the defect. The resulting changes in optical characteristics of the fiber due to this defect were determined. This process allowed for easy modification of the current defect's position and or radius in order to further analyze what affect this will have on the confinement loss. The results follow the ARROW model and show that the closer a defect is to the core region, the higher the confinement loss will be due to surface modes present at the defect. The results also show that the confinement loss is directly related to the size of the air hole defect.

This work is important for other applications besides Ge doped silica rods. This work can help to describe high index rods in a background matrix of a lower refractive index, which is the case for a 7-rod bundled single crystal sapphire fiber. SC-PBG fibers ability to be easily spliced and handled could make for a more desirable fiber for high temperature sensing if materials with similar coefficients of thermal expansion to that of sapphire could be realized. This work also shows how to examine the photonic band gap structure for a range of frequencies for a given fiber structure using Comsol Multiphysics. The results of this study were compared to actual band gap plots of a similar structure and were in good agreement.

3.3 Sapphire Photonic Crystal Fibers

3.3.1 Experimental

The fibers in this section are based off both a single crystal sapphire rod and a single crystal sapphire rod surrounded by a ring of 6 single crystal sapphire rods. The bundling process[68], which is described later in Sections 4.1 and 4.2, enables the outer cladding rods to form a symmetric ring around the central fiber as seen in the schematic of the fiber placement shown in Figure 3.13.

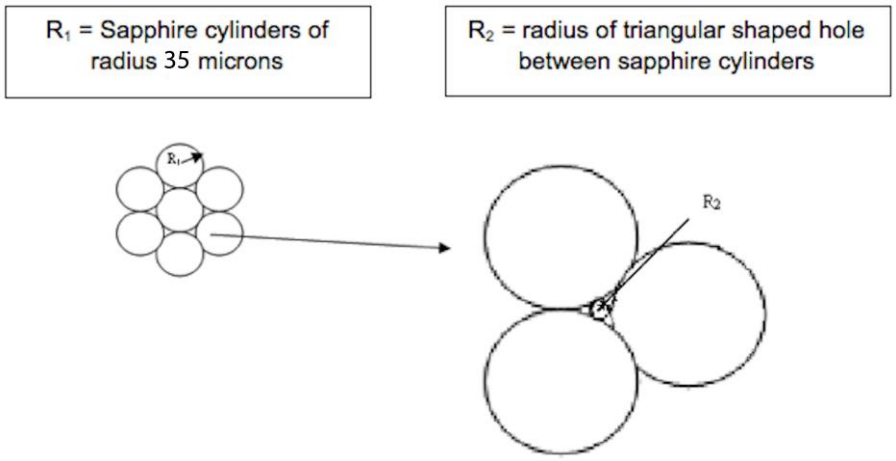

Figure 3.13 Schematic of fiber used in FEM modeling

In Figure 3.13 above, let R_1 be the radius of the sapphire cylinders shown above which equals 35 μm and R_2 be the radius of the hole, which would fit between the cylinders and just touch each cylinder. The radius ratio of R_2 / R_1 is 0.155 by simple geometrical considerations[61]. The upper bound of the hole size in between the sapphire cylinders is then equal to 5.4 μm.

The objective of the work in this section is to model the propagation characteristics of a single rod of single crystal sapphire as well as the 7-rod single crystal sapphire fiber structure. This would permit the resulting changes in optical characteristics of each fiber to be determined. This process would then allow for easy modification of the current size and positioning of the fiber rods in order to further analyze what effect this will have on the confinement loss.

3.3.2 Fem Analysis

Numerical modeling is a key component while creating an optimal fiber design. The high contrast between the 6-ring structure and the smaller air-hole sections places a large burden on the computer's memory because of fast far-field variations. Add to this the fact that the electric

field's normal component will become discontinuous and the equations become quite complex. A linear solver is typically used to compute the Maxwell's equations involved in the FEM discretization. To compensate for this, Comsol Multiphysics uses a direct linear system solver (UMFPACK) for its modal analysis.

Materials selection is the first main topic in sapphire photonic crystal modeling. We start with two separate fibers as described previously, which are scaled to the dimensions being demonstrated experimentally, as seen in a later section (Section 4.2). The single crystal sapphire rods in these models have a diameter of 70 μm. The refractive index of the air region is set to n = 1.0 and the sapphire region (α-Al_2O_3) is set to n = 1.74618. The air (blue) and sapphire (grey) regions can be seen in Figure 3.14. All models are solved for a free space wavelength of 1.55 μm.

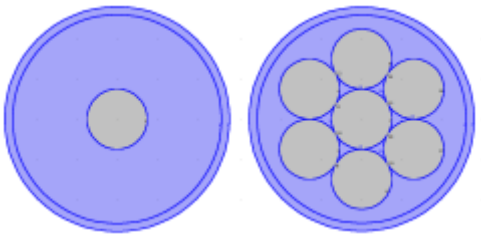

Figure 3.14 The air (blue) region is set to n = 1.0 and sapphire (grey) (α-Al_2O_3) is set to n = 1.74618

The outer diameter of the fiber (the outer ring in Figure 3.14) is set as a perfectly matched layer (PML). The outer diameter for the PML layer is set to 140 μm with an inner PML diameter of 130 μm. No modes are expected in this outer air layer as described in the Fiber Modeling Section 2.7. Confinement loss, L_c, is a commonly used metric for measuring how an optically

modeled fiber will perform under optimal operating conditions and was discussed in the Section 2.7 Fiber Optic Modeling.

The next step in the modeling process is the refinement of a mesh. Figure 3.15 below shows a mesh consisting of 24692 elements in the single rod case and 9508 elements for the 7-rod case. Both were computed on a 12Gb Macintosh I7 running Comsol 4.0a with a solution time of 875 seconds.

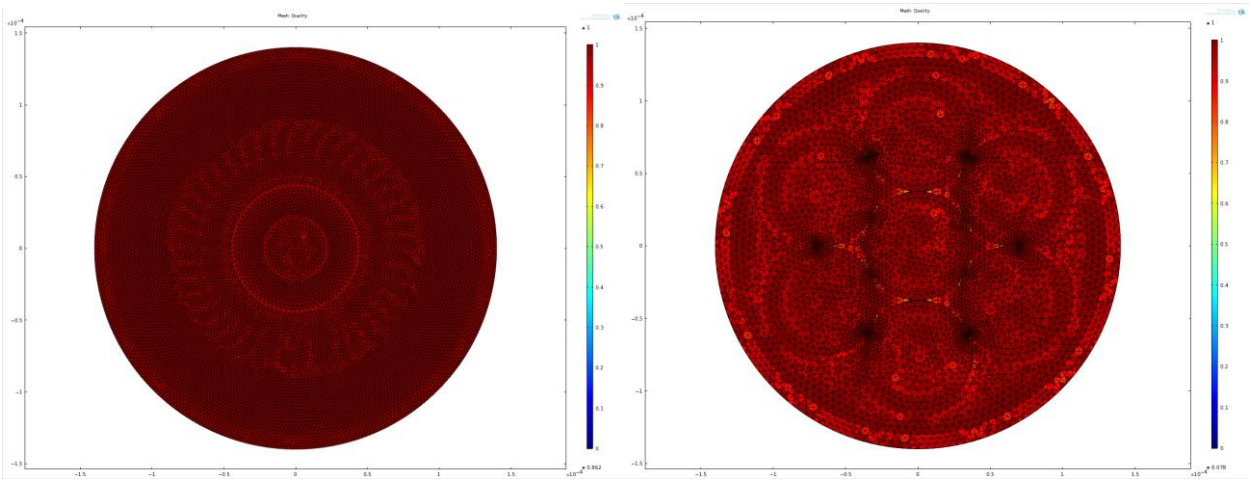

Figure 3.15 2-D Comsol mesh in both the single rod (left) and the 7-rod case (right) with the x and y axes in (m)

The boundary conditions for each fiber must now be setup. A perfect electrical conductor setting was used for the outer edge, while continuity was set inside the cylindrical PML. Comsol is then solved using a direct linear equation solver (UMFPACK) near the effective mode index of the single crystal sapphire (1.74618 at 1.55 μm). Figure 3.16 below is the resultant fundamental hybrid mode for the single rod (left) and the 7-rod case (right). This is as expected for the optical power to be concentrated directly in the center of the core of both the single rod and the central

rod of the 7-rod bundled fiber. The single rod case has an effective mode index of 1.746109 with a corresponding confinement loss L_c = 2.0166e-8 dB/km. The 7-rod case also has an effective mode index of 1.746109 with a larger corresponding confinement loss L_c = 1.3933e-6 dB/km.

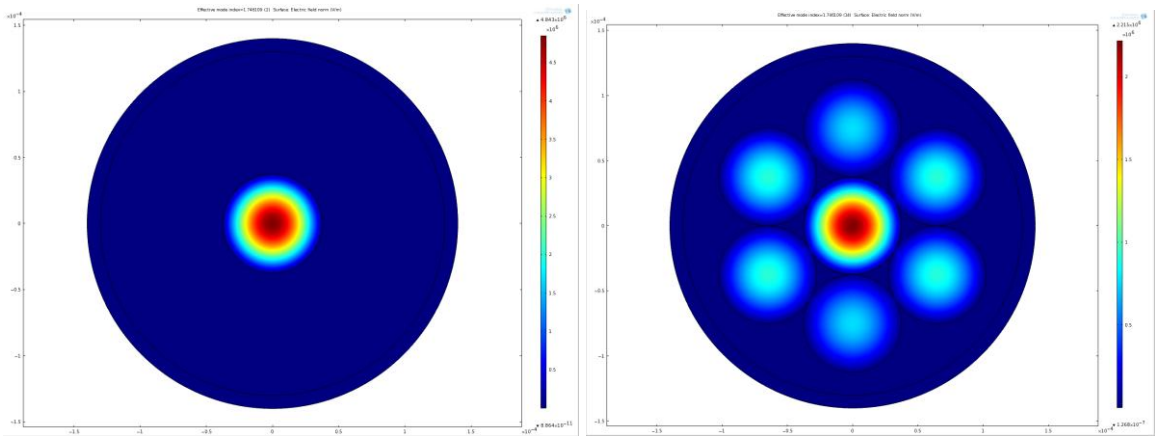

Figure 3.16 2-D Comsol mesh in both the single rod (left) and the 6-ring case (right) with the x and y axes in (m)

Figure 3.17 shows the higher order modes for the single rod case at a free space wavelength of 1.55 μm. They consist (starting clockwise from top-left) of the LP_{11} mode with an effective mode index of 1.745999 and a corresponding confinement loss L_c = 3.9775e-8 dB/km, LP_{21} mode with an effective mode index of 1.745855 and a corresponding confinement loss L_c = 2.3718e-9 dB/km, LP_{02} mode with an effective mode index of 1.745804 and a corresponding confinement loss L_c = 2.7683e-9 dB/km, and the LP_{31} mode with an effective mode index of 1.745678 and a corresponding confinement loss L_c = 1.1347e-8 dB/km.

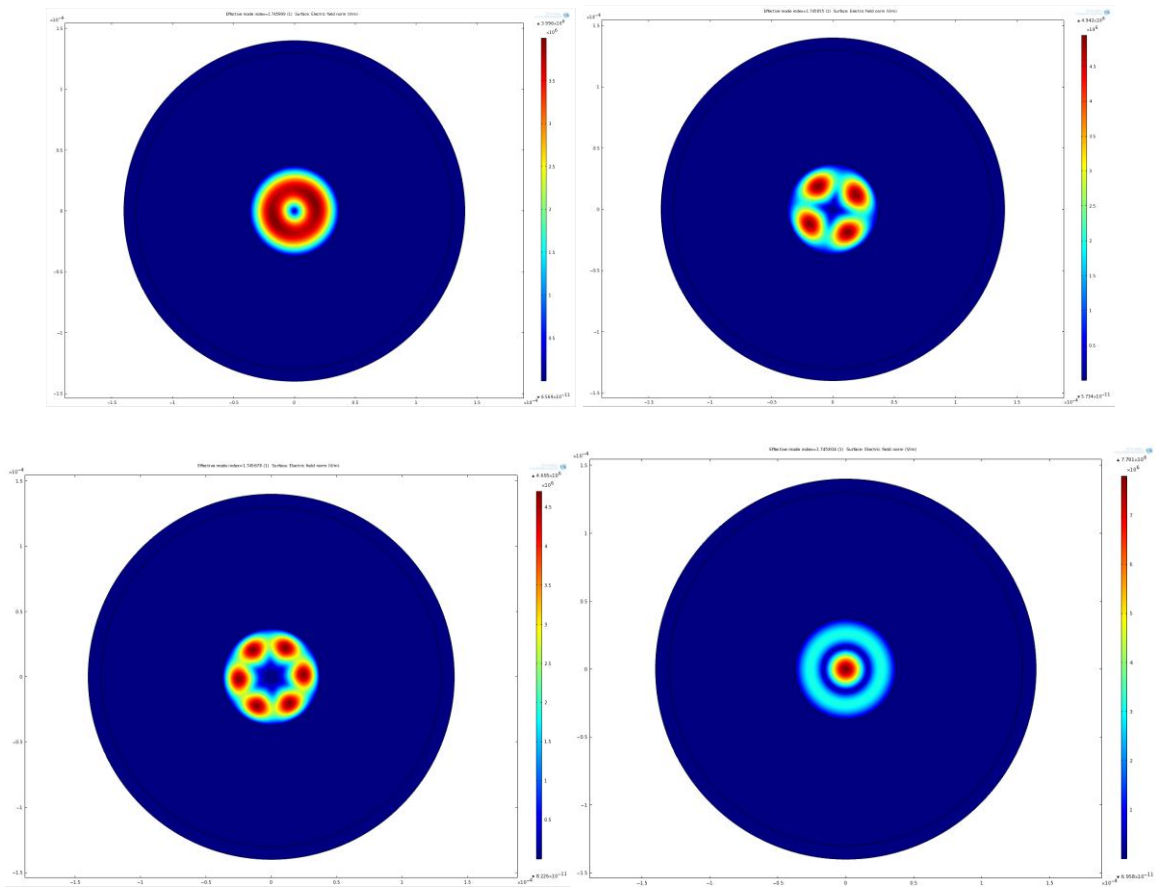

Figure 3.17 Higher order modes for the single rod case: (starting clockwise from top-left) LP_{11}, LP_{21}, LP_{02}, and LP_{31} with the x and y axes in (m)

Figure 3.18 shows the higher order modes for the 6-ring case at a free space wavelength of 1.55 μm. They consist (starting clockwise from top-left) of the LP_{11} mode with an effective mode index of 1.746001 and a corresponding confinement loss L_c = 2.3942e-6 dB/km, LP_{21} mode with an effective mode index of 1.745858 and a corresponding confinement loss L_c = 8.2314e-6 dB/km, LP_{02} mode with an effective mode index of 1.745807 and a corresponding confinement loss L_c = 9.1295e-6 dB/km, and the LP_{31} mode with an effective mode index of 1.745686 and a corresponding confinement loss L_c = 6.7056e-6 dB/km.

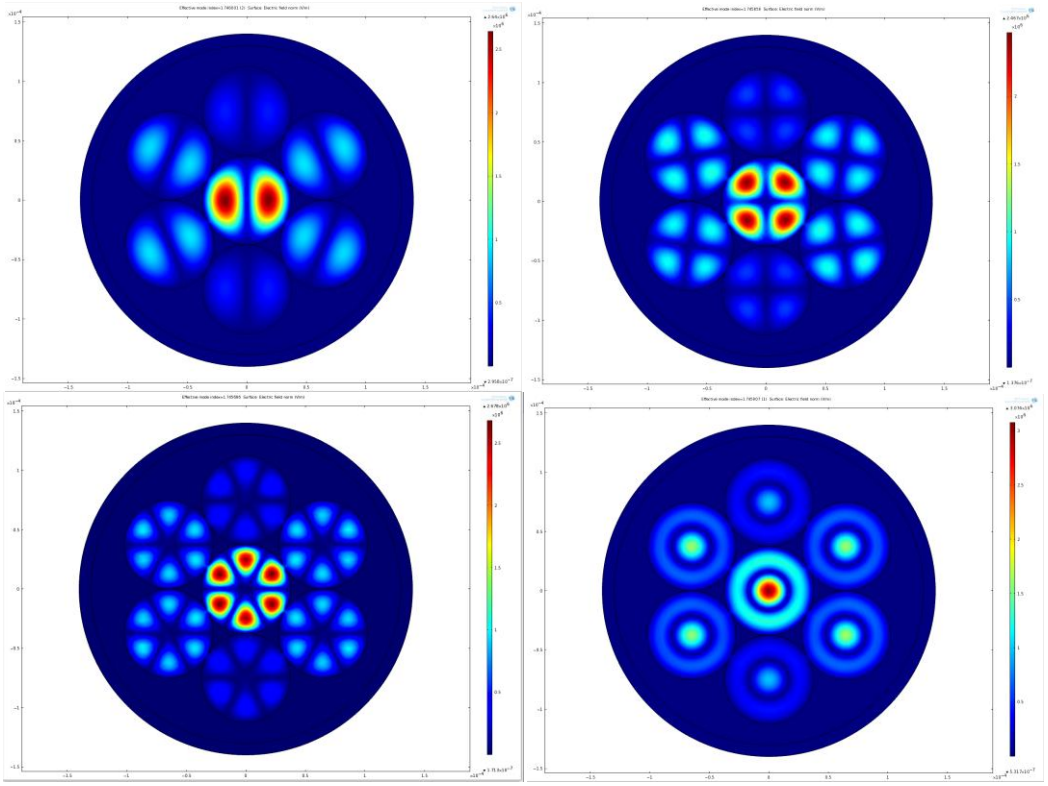

Figure 3.18 Higher order modes for the 6-ring case: (starting clockwise from top-left) LP_{11}, LP_{21}, LP_{02}, and LP_{31} with the x and y axes in (m)

In summary, the single rod sapphire fiber, as well as the 7-rod bundled sapphire fiber was modeled to see if resulting changes in optical characteristics of each fiber could be determined. Although photonic crystal structures have previously been reported in silica-based fibers, this work represents the first time that a single crystal sapphire photonic crystal fiber has been proposed and analyzed using finite element analysis. In general, the modeled bundled fiber has higher confinement loss than the single rod case for the fundamental modes as well as the higher order modes examined. This loss is determined in the central core region only and the figures show what seems to be a coupling to the outer rods for many of the lower order modes. The results also show that the confinement loss is directly related to which mode is propagating

through the fiber as lower order modes generally have a higher confinement loss (less lossy) than higher order modes.

This section is important because the models help to validate the modal coupling from the central core to the outer cladding rods. The theory behind this coupling is that the higher order modes will propagate into the cladding region with part of this cladding region being the outer ring of single crystal sapphire fibers. In the single rod of sapphire, these higher order modes would generally be scattered or lost, but in the 7-rod bundled fiber, these modes have the ability to be recaptured, leading to less loss and a greater intensity of the transmitted signal.

3.4 7-Rod Bundled Silica Fiber

3.4.1 Experimental

There is a need to create a cladding that will allow silica to be used for sensing at higher temperatures. The fiber cladding must be stable at high temperatures, have a refractive index less than the core region, remain chemically inert, and should have a similar coefficient of thermal expansion to that of the silica core. A unique solution has been developed for single crystal sapphire fibers[62-64] by bundling sapphire fibers around a sapphire fiber core, essentially serving as an external fiber cladding. This design, which can be similarly used in a silica structure, has the same material for both the cladding and core. This meets the cladding material requirements stated previously, while still having the capability to function as a pressure, temperature, or gas sensor.

Single rods of silica fiber are cheap, easy to manufacture, and can operate[65] to 1000 °C when undoped[66]. Compared to a bare silica fiber, the lack of cladding on a single rod of silica would result in higher environmental vulnerability due to fluctuations in the optical signal as a result of materials adsorbed or reactions at the fiber surface. This also creates a higher modal volume from the lack of a cladding layer resulting in higher phase difference between low and high order modes. The new bundled fiber designs can then be carried over to higher temperature fibers like those made of single crystal sapphire, which are a better choice than silica for harsh, high temperature environment sensing, as in the coal gasification industry.

In this work, an all silica bundled fiber has been developed and analyzed using Comsol Multiphysics 4.2a finite element analysis program. The radial spacing between the outer ring of cladding versus the solid silica core will allow us to understand how to optimize this type of bundled fiber structure. This will determine how precise the fiber bundling process needs to be to effectively reduce the number of modes that the fiber contains.

The modeling of the modes that are predicted to exist in the silica fiber bundles in relation to the spacing between them has been completed with COMSOL Multiphysics 4.2a modeling software. Silica fibers, with an outer diameter of 70 µm, were first modeled with the 6 outer rods touching the silica core in a pattern that consisted of a central fiber surrounded by six outer fibers, forming a symmetric ring around the central fiber. A single rod case was also modeled to show the reduction in modes from the 7-rod bundled case versus the single rod of silica case. The material properties of the bundled fiber and the single rod of silica are chosen to match those of the fiber materials being tested. The main variables include the refractive index (both real and the

imaginary part), electrical conductivity, relative permittivity, and relative permeability values for the core and cladding rods. Figure 3.19 shows a schematic of the fiber arrangement, the radial movement of the outer rods, and the respective refractive indices used in this model for both fibers. The air (blue) region is set to n = 1.0 and silica (grey) is set to n = 1.45. The outer rods were then moved radially outward away from the core rod in 2.5 μm increments in order to analyze how the spacing between the cladding rods and the central core rod effects the modal confinement of the core rod.

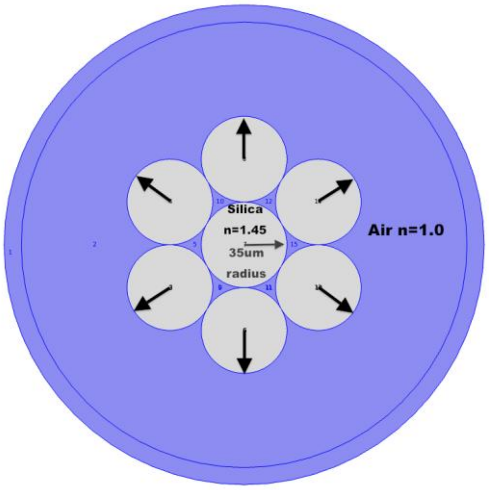

Figure 3.19 A 7-rod bundle of silica in air showing the fiber arrangement and the radial movement of the outer rods in 2.5 μm increments away from the central core rod

The different fiber arrangements were discretized with a minimum average mesh element quality of 0.937 for each model. Each model was analyzed at the standard telecommunications free space wavelength of 1.55 μm. Each model was also carried out at standard temperature and pressure. A perfectly matched layer (PML) was set to 280 μm with an inner PML diameter of 260 μm on all models.

Comsol Multiphysics then uses a direct linear system solver (UMFPACK) with the option for using multiple core computing to complete its modal analysis by solving near the effective mode index of silica (1.45 at a free space wavelength of 1.55 μm). The number of modes that propagate in the core region of the single rod and all of the spacing's of the bundled fibers must then be calculated[67]. Both the single rod of silica and all of the bundled fibers with various spacing will be highly multimode due to the large dielectric contrast between the silica core and the air cladding. The power flow time average in the z-direction, which is based on the Poynting vector, is calculated for the central core rod in all of the modeled scenarios. The calculated number of modes is determined by both the power flow time average in the z-direction and the propagation constant. This process removes the leaky modes from the results giving a more accurate representation of the actual number that will propagate in each fiber design.

3.4.2 Fem Analysis

Comsol Multiphysics 4.2a has been used to examine confinement loss vs. number of modes for both the single rod of silica and the bundled case where all of the outer silica rods are touching the central core rod as seen in Figure 3.20. The single rod case shows upwards of 2488 modes whereas the 7-rod bundled silica structure has approximately 1664 modes. This is a modal reduction percent difference of 39.69% from the 7-rod case to the single rod case.

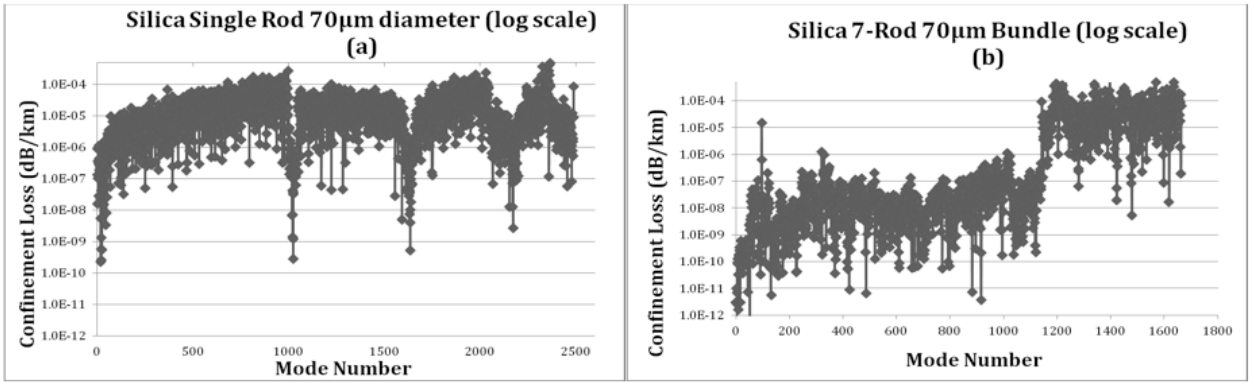

Figure 3.20 Single rod of silica (a) versus a 7-rod bundled silica fiber (b) showing the differences in confinement loss versus mode number

Thick bands of relatively high loss can be seen in both graphs in Figure 3.20 but are more distinct in the single rod case. The 7-rod bundled case shows almost no bands of relatively high loss for the lower order modes (up to about the 1150th mode), which is most likely due to higher order modes being re-coupled into the outer ring of rods instead of being lost. It is important to note that the loss in the 7-rod bundle is on average much less than the single rod case for the lower order modes.

This work agrees with previous modeling work completed[64] using an all sapphire 7-rod bundle compared to a single rod of single crystal sapphire with the same rod diameters. The outer ring of the 7-rod bundle was then moved radially outward from the core rod in 2.5 µm increments. This data was also completed using the same geometry as in Figure 3.19 with a free space wavelength of 1550 nm.

Figure 3.21 shows a large drop in the number of modes within the first 5 µm due to the outer rods either touching or being very close to the central core rod. The graph then drops off near 2350 modes as it slowly approaches the number of modes found in the single rod fiber. The core

only fiber represents the infinite distance case where a 7-rod bundle would have its outer ring of silica fibers so far away from the central core rod that the ring would have no effect on the modal reduction. This data confirms that the closer the outer ring of rods is to the central core rod, the more modal reduction will take place. This is due to the average index lowering of the cladding rods combined with the air region.

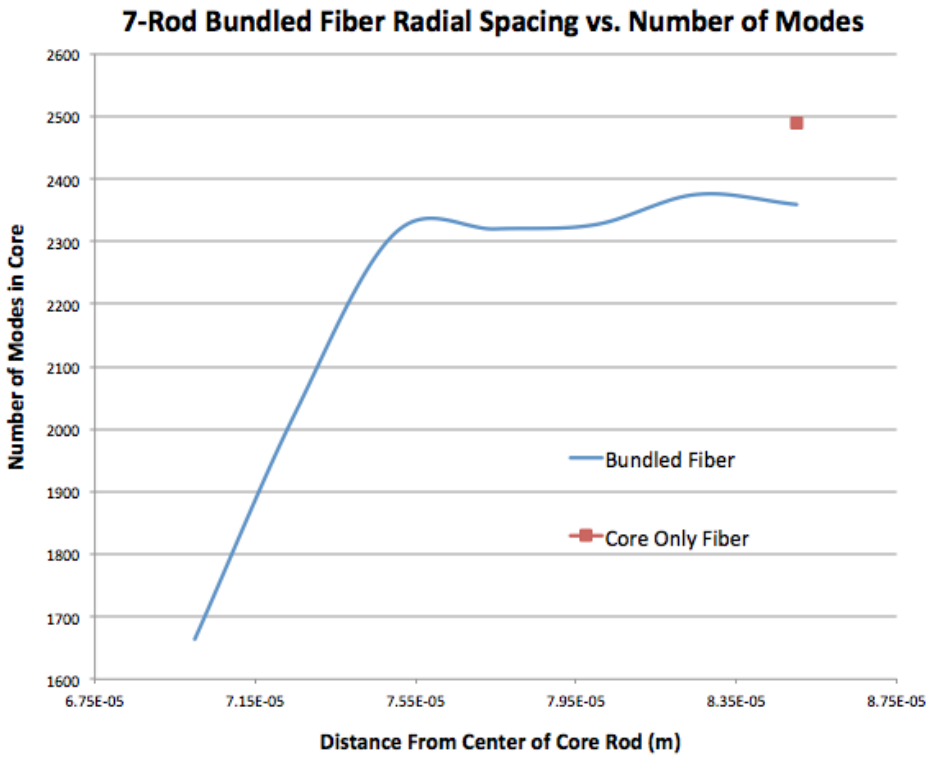

Figure 3.21 7-rod bundled silica fiber radial spacing versus the number of modes at that spacing

In summary, Comsol Multiphysics 4.2a was used to examine both a single rod of silica with a core diameter of 70 μm and also a 7-rod silica fiber with diameters of 70 μm, all made of bare silica fiber. The 7-rod case shows a modal reduction percent difference of 39.69% from the single rod of silica fiber with an air cladding when all of the surrounding rods of silica are touching the core rod.

3.5 Mode Reduction in Bundled Sapphire Photonic Crystal Fibers

3.5.1 Experimental

The fiber designs examined in this section have an outer ring of single crystal sapphire rods which surround the central core rod and produce voids periodically around the central core. This lowers the effective refractive index of the air-sapphire region surrounding the core rod. This allows for a modal reduction while still maintaining the material advantages of using single crystal sapphire as a cladding layer as previously described. The first photonic crystal fiber made of single crystal sapphire fiber was published previously by Pfeiffenberger[68] et al. and incorporated this same hexagonal shape in a 15 cm long bundled fiber. Initial work has been accomplished with the FEA models to examine the modal structure of these types of fibers in greater detail[69].

The fibers examined in this study fall into the photonic crystal fiber category. These fibers all operate via total internal reflection (TIR). In these fibers, light is more strongly confined to the core due to a large refractive index difference of single crystal sapphire, 1.74618 vs. 1.0 for air at a free-space wavelength of 1.55 μm. The other branch of photonic crystal fibers operate via a photonic band gap which was described in great detail in Section 2.3 Photonic Band Gap Fibers.

The fibers in this section are examined to show how the rod diameter of a hexagonal ring of single crystal sapphire affects the modal volume of the fiber. In this study, two different fibers are compared versus a single rod case with no cladding. The number of modes that propagate in an optical fiber is directly affected by the size of the core. The core sizes in these cases are 50

μm and 70 μm in diameter, respectively. The number of modes propagating in a step index multimode fiber, *Nm*, can be approximated by Equation 27:

$$Nm = 0.5 * \left(\frac{\pi * D * NA}{\lambda}\right)^2 \quad (27)$$

where D = diameter of the core, λ = wavelength of propagation, and NA is the numerical aperture, which is the light gathering ability of the fiber. The equation for numerical aperture can be approximated by Equation 28:

$$NA = \sqrt{{n_f}^2 - {n_c}^2} \quad (28)$$

with n_f = the refractive index of the core and n_c = the refractive index of the cladding. In the single rod case, n_f = 1.74618 (single crystal sapphire) while n_c = 1.0 (air). In both bundled fibers, n_c = an average somewhere between 1.0 and 1.74618, lowering the effective refractive index of this material. Comsol Multiphysics estimates the effective refractive index of this air-sapphire region surrounding the core in both fibers to be approximately 1.7147. Plugging this value into Equation 28 for n_c with n_f = 1.74618 we obtain an NA = 0.330. When this value is substituted in Equation 27 above, we obtain Equation 29:

$$Nm = 0.5 * \left(\frac{\pi * D * (0.330)}{1.55 \mu m}\right)^2 \quad (29)$$

when $D = 70$ µm, $Nm = 1096.05$ and when $D = 50$ µm, $Nm = 559.209$. The real question that this modeling work aims at understanding is how the average effective index really is affected by the reduction in fiber diameter for a bundled fiber from 70 µm to 50 µm at a wavelength of 1.55 µm.

This section examines two single crystal sapphire photonic crystal fibers through the use of a Finite Element Modeling (FEM) program called Comsol Multiphysics 4.2. FEM is useful for fiber optics research because it can accurately predict the modal structure of an optical fiber without fabrication. The objective of this section was to model the propagation characteristics of both a bundled fiber with 70 µm diameter rods and a bundled fiber with 50 µm diameter rods at 1.55 µm with the rods all being composed of single crystal sapphire. This process allows us to examine the benefits of a smaller core size for this bundled structure.

3.5.2 Fem Analysis

The fibers in this section are composed of a single crystal sapphire rod surrounded by a ring of 6 other single crystal sapphire rods, all of which are either 70 µm (left) or 50 µm (right) in diameter as seen in Figure 3.22 below. The air regions, as seen in blue in Figure 3.22, have a refractive index of n=1.0 while the gray region has a refractive index of n=1.74618. The process for creating this type of fiber experimentally has been outlined in previous papers[68,69].

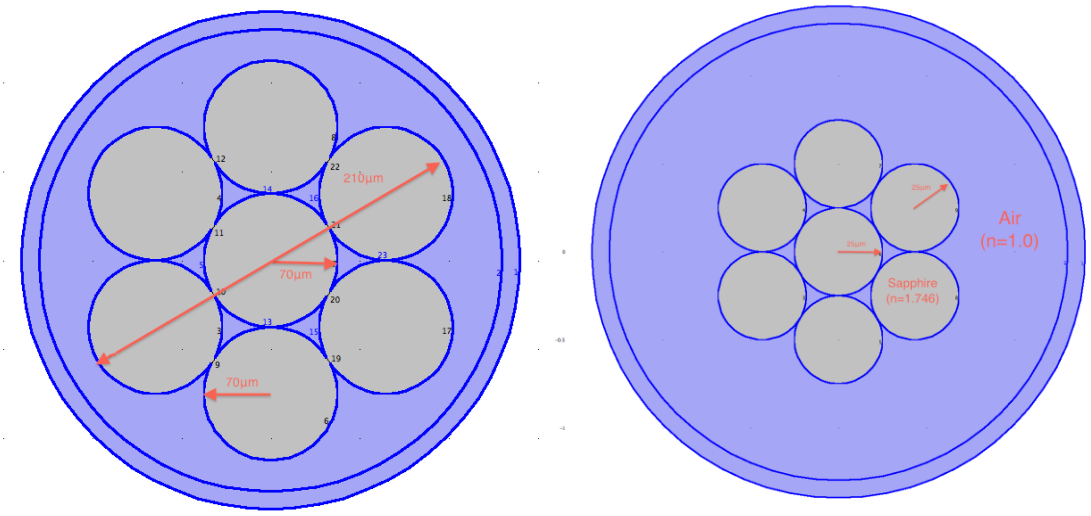

Figure 3.22 Schematic of fibers used in FEM. At left, the bundle composed of 7 (70 µm) rods of single crystal sapphire (in gray) surrounded by air (blue region). At right, the bundle composed of seven (50 µm) rods of single crystal sapphire (in gray) surrounded by air (blue region)

The sapphire rods in this study were examined along the C-axis of the crystal extending along the length of the fiber (z-direction). The hexagonal crystal structure of single crystal sapphire has two axes perpendicular to the c-axis, referred to as the A-axes.

The first step in the modeling process is the materials selection. As described above in Figure 3.22, two fibers, a bundled fiber with 70 µm diameter rods and a bundled fiber with 50 µm diameter rods are to be examined. The dimensions of the rods and the material properties are then adjusted so that the rods of single crystal sapphire (α-Al_2O_3 in gray) have a refractive index of n = 1.74618 and are surrounded by air (blue region), where n=1.0. All models in this section are solved for using a free space wavelength of 1.55 µm, as this is a standard telecommunications wavelength. The outer region of the fibers in Figure 3.22 is set as a perfectly matched layer (PML). The outer diameter for the PML layer is set to 280 µm with an inner PML diameter of

260 μm. Confinement loss, L_c, is a commonly used term for measuring loss under optimal operating conditions in FEM modeling and was discussed in Section 2.7 Fiber Optic Modeling.

Another important metric that Comsol Multiphysics can calculate for a given mode is the power flow time average, Po*i*av, as discussed in Section 2.7 Fiber Optic Modeling. The boundary conditions governing each fiber rod in the bundle is then determined. A perfect electrical conductor (PEC) setting was selected for the inner ring surrounding the fiber bundle as is common in the FEA of optical fibers. The regions inside of the PEC where set to a continuity boundary condition. As discussed previously, a cylindrical PML was set for the region surrounding the PEC.

The next step in the Comsol Multiphysics modeling process is the mesh refinement. Both models in this section require a complex mesh to render the large air-sapphire regions with high accuracy. Figure 3.23 below shows a mesh consisting of 64240 elements for the bundled fiber with 70 μm diameter rods and 88864 elements for the bundled fiber with 50 μm diameter rods.

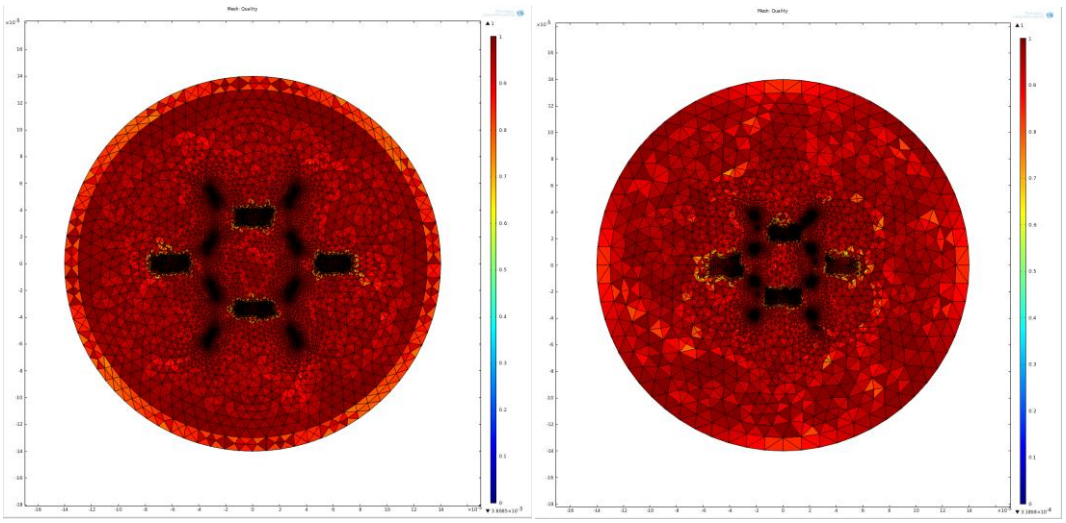

Figure 3.23 2D Comsol meshes of both the bundled fiber with 70 µm diameter rods (left) and the bundled fiber with 50 µm diameter rods (right) with the x and y axes in (m)

RF modal propagation problems are generally solved with a linear solver so that Maxwell's equations in the FEM discretization can be computed without error. These equations are solved using a direct linear equation solver (UMFPACK) in combination with the MUMPS solver, which allows for the use of multiple cores, near the effective mode index of the single crystal sapphire (1.74602 at 1.55 µm). The models for this paper were computed on a 12Gb Macintosh I7 running Comsol 4.2 with a solution time near 7200 seconds for 500 modes.

Figure 3.24 below is the resultant fundamental hybrid mode for the bundled fiber with 70 µm diameter rods solved at a free space wavelength of 1.55 µm with 416663 degrees of freedom. Figure 3.25 below is the resultant fundamental hybrid mode for the bundled fiber with 50 µm diameter rods solved at a free space wavelength of 1.55 µm with 622176 degrees of freedom. In both Figures 3.24 and 3.25, the red arrows show the electric field polarization. The polarizations of these modes are 90° from each other for a given *LP* mode. The optical power is expected to

be concentrated directly in the center of the core of the central rod in both fibers due to the coupling from the outer ring of rods in both cases. The 70 µm diameter rods case has an effective mode index of 1.74602 with a corresponding confinement loss L_c = 2.0166e-8 dB/km. The 50 µm diameter rods case has an effective mode index of 1.74602 with a smaller corresponding confinement loss L_c = 1.92e-9 dB/km.

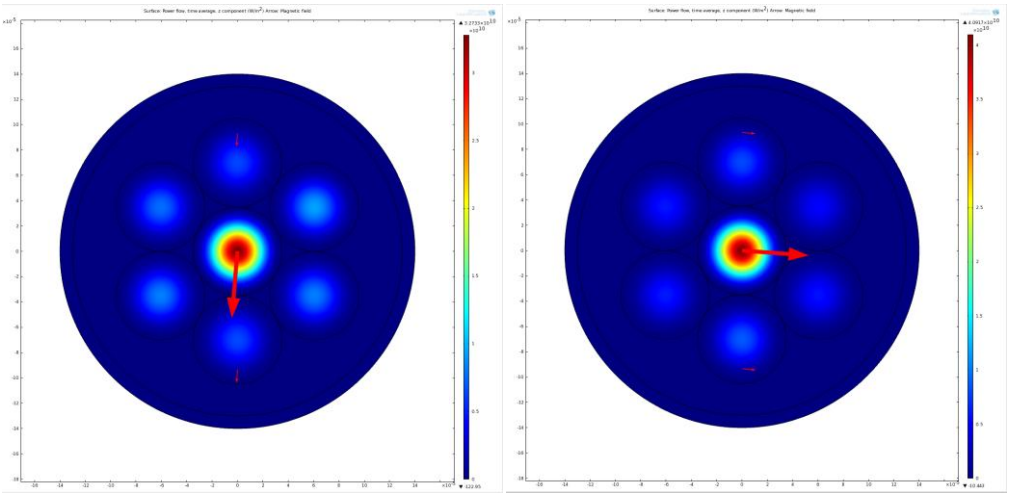

Figure 3.24 Fundamental LP_{01} modes for the bundled fiber with 70 µm diameter rods showing both electric field polarizations with red arrows with the x and y axes in (m)

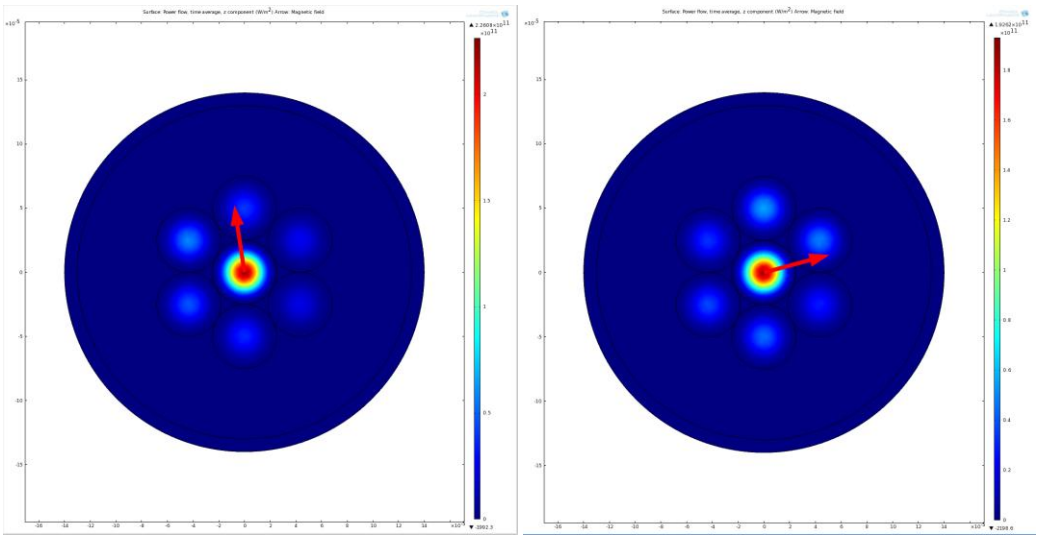

Figure 3.25 Fundamental LP_{01} modes for the bundled fiber with 50 µm diameter rods showing both electric field polarizations with red arrows with the x and y axes in (m)

Comsol Multiphysics also allows us to calculate the number of modes that will propagate in both fibers. By solving for all of the eigenmodes at a free space wavelength of 1.55 µm we find that the bundled fiber with 70 µm diameter rods holds approximately 38000 modes with 5429 of these modes being confined to the central 70 µm diameter core rod. The bundled fiber with 50 µm diameter rods holds approximately 22058 modes with 2844 of these modes being confined to the central 50 µm diameter core rod. This gives a modal reduction that is on the scale of that mentioned in Equation 29. Figure 3.26 shows the effective refractive index vs. confinement loss for the bundled fiber with 70 µm diameter rods. Figure 3.27 shows the mode number vs. confinement loss (right) for the bundled fiber with 70 µm diameter rods.

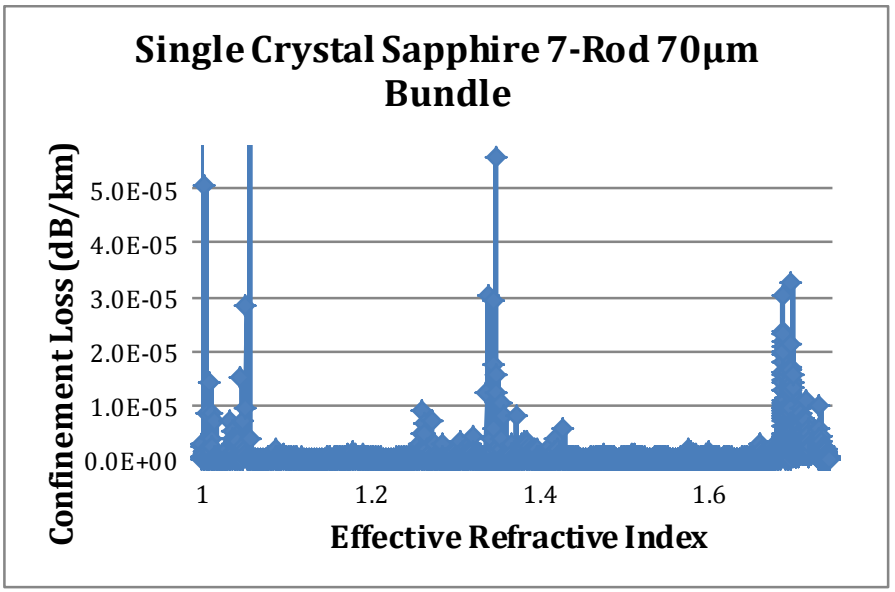

Figure 3.26 Effective refractive indexvs. confinement loss (dB/km) for the bundled fiber with 70 µm diameter rods

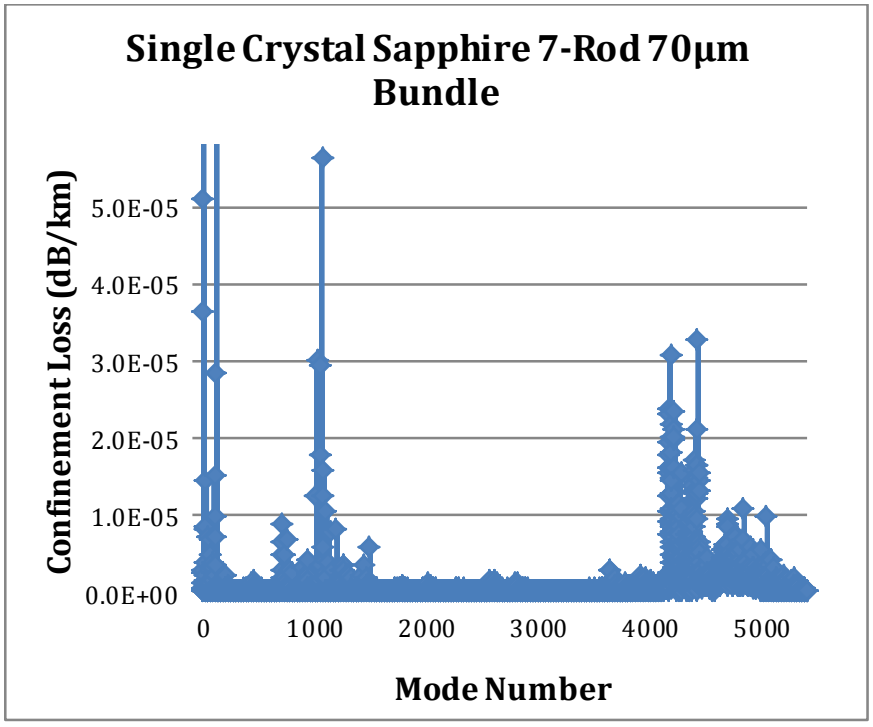

Figure 3.27 Mode number vs. confinement loss (dB/km) for the bundled fiber with 70 µm diameter rods

Figure 3.28 shows the effective refractive index vs. confinement loss for the bundled fiber with 50 µm diameter rods. Figure 3.29 shows the mode number vs. confinement loss (right) for the bundled fiber with 50 µm diameter rods. The data shows that the confinement loss for the bundled fiber with 50 µm diameter rods is much less than that of the bundled fiber with 70 µm diameter rods. This is mainly due to the smaller core size, which gives a reduction of modes in the 50 µm diameter rod case.

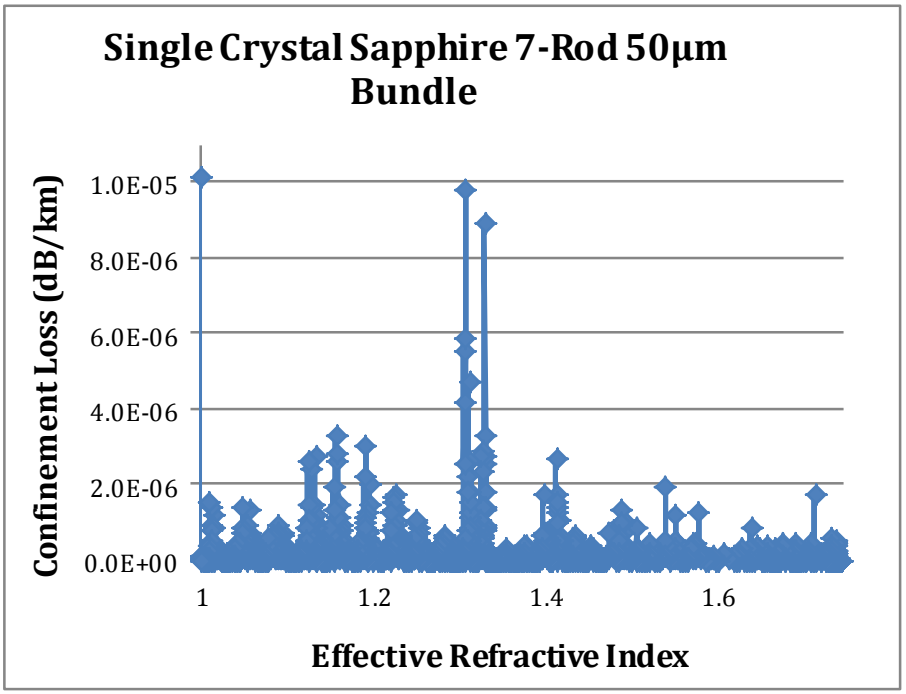

Figure 3.28 Effective refractive index vs. confinement loss (dB/km) for the bundled fiber with 50 µm diameter rods

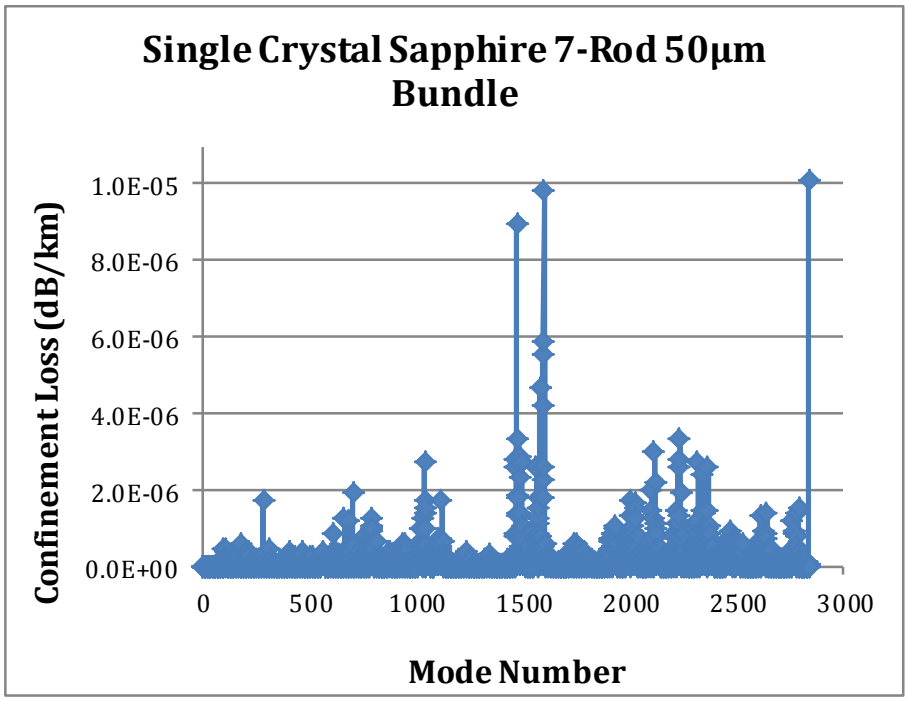

Figure 3.29 Mode number vs. confinement loss (dB/km) for the bundled fiber with 50 µm diameter rods

In summary, two sapphire photonic crystal fiber bundles have been presented and modeled using a multi-physics FEM program. Other single crystal sapphire fiber bundles with this type of structure have been previously[69] modeled, but this is the first attempt at optimization by reducing the diameter of the core and surrounding fibers. In this study we find that the bundled fiber with 70 µm diameter rods holds approximately 38000 modes with 5429 of these modes being confined to the central 70 µm diameter core rod. The bundled fiber with 50 µm diameter rods holds approximately 22058 modes with 2844 of these modes being confined to the central 50 µm diameter core rod. The mode counting data shows that the confinement loss for the bundled fiber with 50 µm diameter rods is much less than that of the bundled fiber with 70 µm diameter rods. This is mainly due to the smaller core size, which is a large contributor to the reduction of modes.

3.6 6-Rod Bundled Sapphire Photonic Crystal Fiber

3.6.1 Experimental

This section presents the results of the finite element modeling of a unique 6-rod bundled sapphire photonic crystal fiber. The structure is composed of five rods of single crystal sapphire fiber 70 μm in diameter symmetrically arranged around a solid single crystal sapphire core region, which is 50 μm in diameter. The modeling work focuses on the optimization and modal analysis of this photonic crystal fiber using Comsol Multiphysics 4.2a. The objective of this modeling work is to examine how a fiber design will perform optically without having to build the fiber. In sensor design and realization, reduction of the modal volume of the fiber can offer significant advantages, and as such, this research work is focused on computational determination of the structures, which may minimize the number of modes of the sapphire photonic crystal fiber. The fiber design being analyzed in this paper may be especially important for sensors operating in harsh high temperature environments.

Modeling different bundled sapphire fiber designs that can readily be fabricated allows for the continuous improvement in modal reduction. Different cladding designs can enable a reduction in the effective refractive index difference, which can reduce the number of modes that will propagate in the fiber. This also may allow the fibers to eventually approach single mode guidance.

3.6.2 Fem Analysis

Comsol Multiphysics 4.2a requires the user to first select the geometry and axes of the fiber in question. During this step, the size and shape of the core and cladding layers are chosen. In this model, the properties of the fiber are as follows: the central core rod is set to a diameter of 50 μm with 5 rods surrounding the central rod with diameters of 70 μm each. An image of this fiber can be seen at the left in Figure 3.30. A 50 μm diameter single crystal sapphire fiber with an air cladding has also been modeled as seen at the right in Figure 3.30.

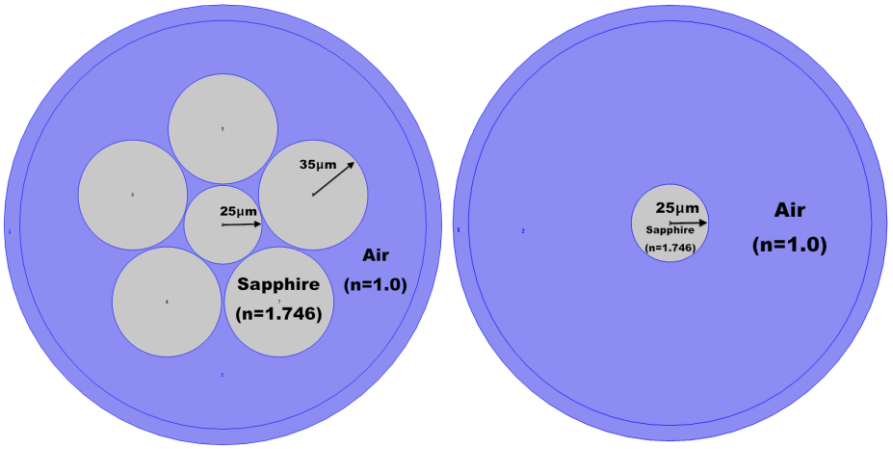

Figure 3.30 Geometry of 6-rod bundled single crystal sapphire fiber (left) and a single rod of single crystal sapphire in air (right) with respective refractive indices. The air (blue) region is set to n = 1.0 and sapphire (grey) (α-Al_2O_3) is set to n = 1.74618 in both models

Next, the material properties of the fiber are chosen. The main variables include the refractive index (both real and the imaginary part), electric conductivity, relative permittivity, and relative permeability values for the core and cladding. Figure 3.30 also shows the respective refractive indices used in this model for both fibers. The air (blue) region is set to n = 1.0 and sapphire (grey) (α-Al_2O_3) is set to n = 1.74618. The boundary conditions for each fiber must then be

established. A perfect electrical conductor setting was used for the outer edge, while a continuity boundary condition was set inside the cylindrical perfectly matched layer (PML). The outer diameter of both fibers in Figure 3.30 was set as a perfectly matched layer (PML). The outer diameter for the PML layer was set to 280 μm with an inner PML diameter of 260 μm for both fibers.

The mesh of the fiber's geometry must be designed. Here a precise mesh using a triangular grid is necessary due to the complicated fiber designs to obtain optimal accuracy. A mesh was developed for the 6-rod case with 38704 elements with an average element quality of 0.9559 as seen at left in Figure 3.31. The mesh for the single rod case had 24812 elements with an average element quality of 0.9775 as seen at right in Figure 3.31. The difference in mesh quality and number of elements stems from Comsol's difficulty to render the multiple fiber rods that are close to touching for the 6-rod case.

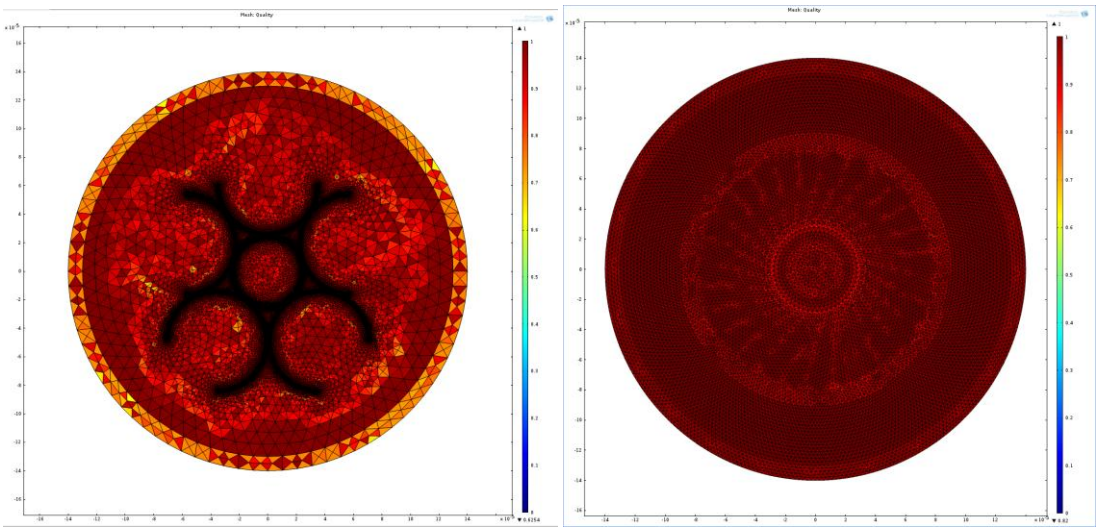

Figure 3.31 2-D mesh structure for the 6-rod bundled single crystal sapphire fiber with 38704 elements and an average element quality of 0.9559 (left) and for the single rod case with 24812 elements and an average element quality of 0.9775 (right) with the x and y axes in (m)

After the mesh is chosen, the modal analysis of the fiber begins. The user specifies the desired number of modes to search for and which effective index to look around after specifying the free space wavelength (which is the wavelength at which the modes propagating in the fiber are being tested). These models are solved using a direct linear system solver (UMFPACK) by solving near the effective mode index of the single crystal sapphire (1.74618 at a free space wavelength of 1.55 μm). The 6-rod case solves for 338941 degrees of freedom while the single rod case solves for 174317 degrees of freedom. In both cases, this is done through a number of iterations until a solution converges that meets a defined error limit.

After the solution is computed for a discrete number of modes, the models undergo post processing. Figure 3.32 below is the resultant fundamental hybrid mode for the 6-rod single crystal sapphire fiber showing both polarizations of the electric field. Figure 3.33 below is the

resultant fundamental hybrid mode for the single rod case of single crystal sapphire fiber showing both polarizations of the electric field. It is expected for the optical power to be concentrated directly in the center of the core of both the single rod case and central rod of the 6-rod fiber. The fibers in Figures 3.32 and 3.33 are highly multimode due to the large refractive index contrast between the core and cladding layers. The 6-rod case has an effective mode index of 1.74602 for both polarizations with corresponding confinement losses of L_c= 6.97051e-9 dB/km and L_c= 1.1817e-8 dB/km respectively. The single rod case has an effective mode index for both polarizations of its fundamental mode at 1.74602 with corresponding confinement losses L_c= 2.8976e-8 dB/km and L_c= 2.4770e-8 dB/km respectively.

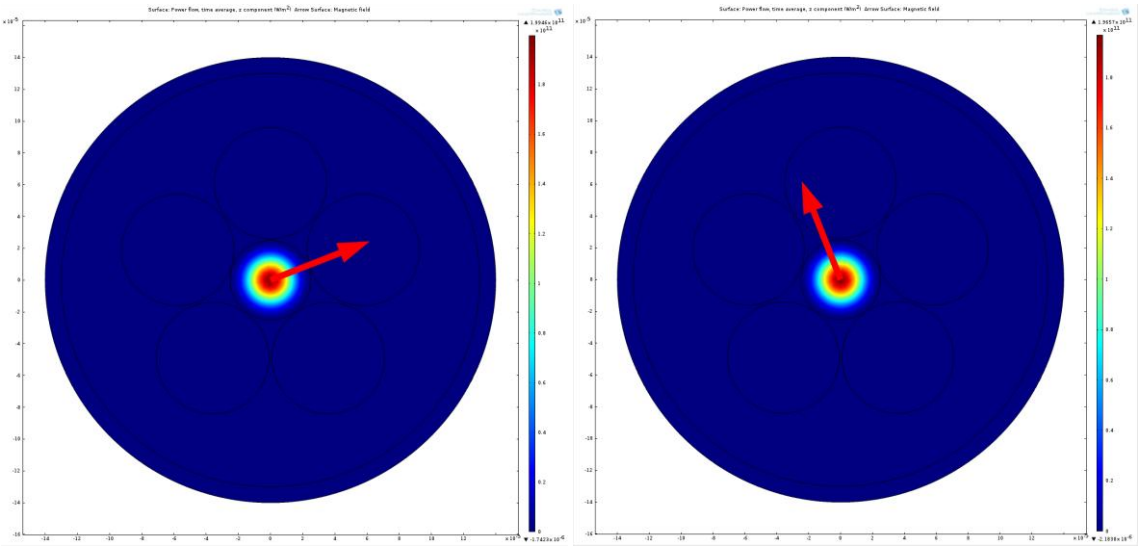

Figure 3.32 Linearly polarized LP_{01}–like modes for the 6-rod bundled single crystal sapphire fiber. The red arrow represents the electric field polarization for the fundamental mode (left and right) with the x and y axes in (m)

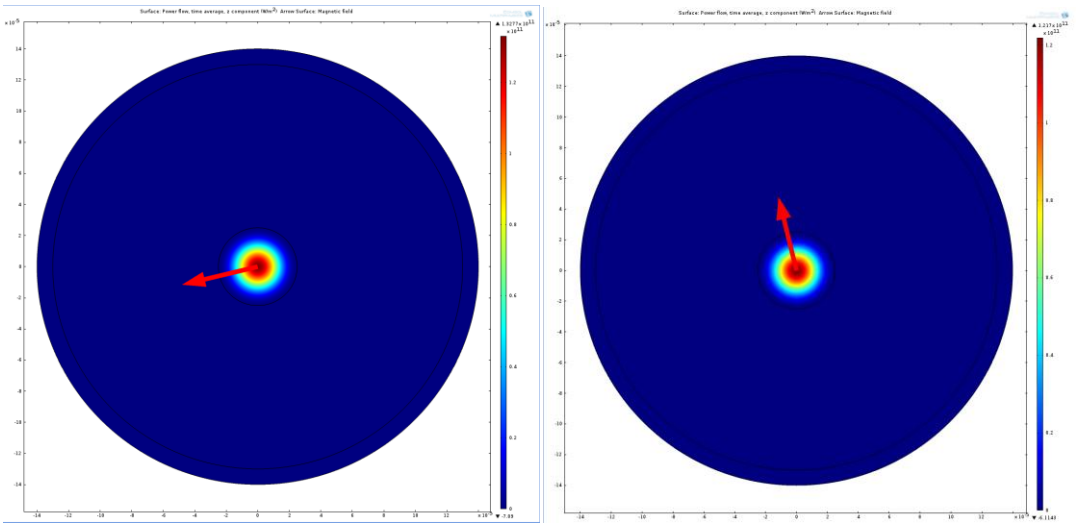

Figure 3.33 Linearly polarized LP_{01}–like modes for the single rod bundled single crystal sapphire fiber. The red arrow represents the electric field polarization for the fundamental mode (left and right) with the x and y axes in (m)

The number of modes that propagate in the core region of both fibers is then calculated[70]. This process consists of searching for the number of modes between the refractive indices of the core and cladding materials. Both of the fibers being analyzed are highly multimode thus a large number of modes need to be calculated. The power flow time average in the z-direction, which is based on the Poynting vector, is calculated for the core in both fibers. This metric removes surface or leaky modes from the results and give a more accurate representation of the actual number of modes that will propagate in each fiber. The calculated number of modes is determined by both the power flow time average in the z-direction and the propagation constant.

Comsol Multiphysics 4.2a has been used to examine confinement loss vs. effective refractive index for both the single rod and 6-rod single crystal sapphire cases. Using this data also allows

for the measurement of how many modes will propagate in each of these fibers. As seen in the Figure 3.34 below, the single rod case shows upwards of 4208 modes whereas the 6-rod bundle of single crystal sapphire has approximately 3496 modes. This is a modal reduction percent difference of 18.48%

The effective refractive index is plotted versus confinement loss in Figures 3.34 and 3.35 below, which demonstrates the predicted lossy regions with the effective refractive index value at which the mode was recorded. Thick bands of relatively high loss can be seen in both Figures 3.34 and 3.35 but are more distinct in the single rod case. The 6-rod bundled case shows thinner bands of relatively high loss, which is most likely due to the higher order modes being coupled into the outer ring of rods. It is important to note that the loss in the 6-rod bundle is on average less than the single rod case over the entire effective refractive index range. The lowest order modes have the lowest confinement loss in both fibers. This is especially prevalent in the 6-rod case. As the higher order modes approach a lower effective refractive index value, the modes tend to propagate in more than one rod in the 6-rod structure. This in turn, increases confinement loss. When compared to similar structures that have been modeled for harsh, high temperature environments, we see that other fiber designs[70] offer superior modal reductions in single crystal sapphire.

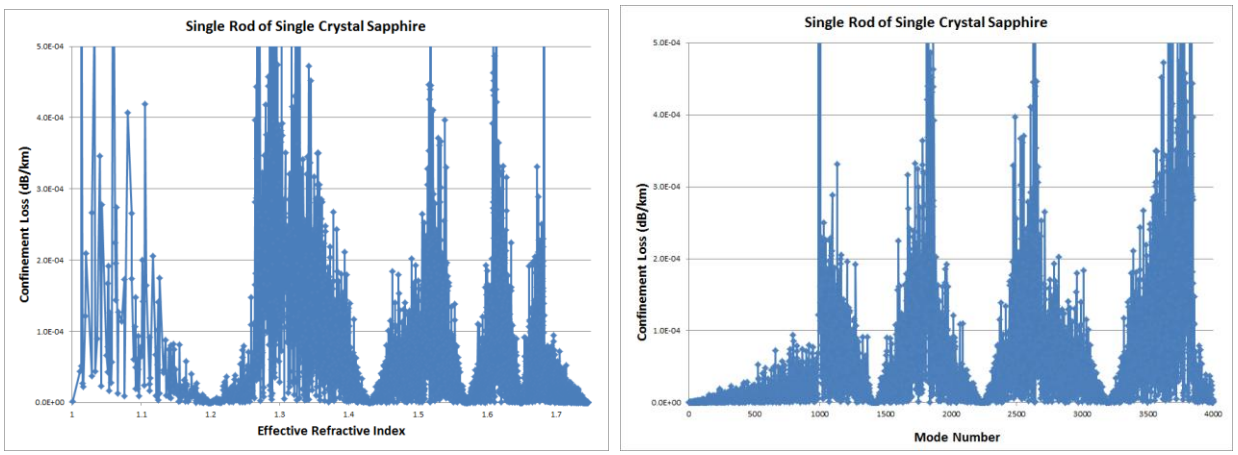

Figure 3.34 Confinement loss vs. effective refractive index(left) and mode number (right) for single crystal sapphire fiber consisting of 1 rod

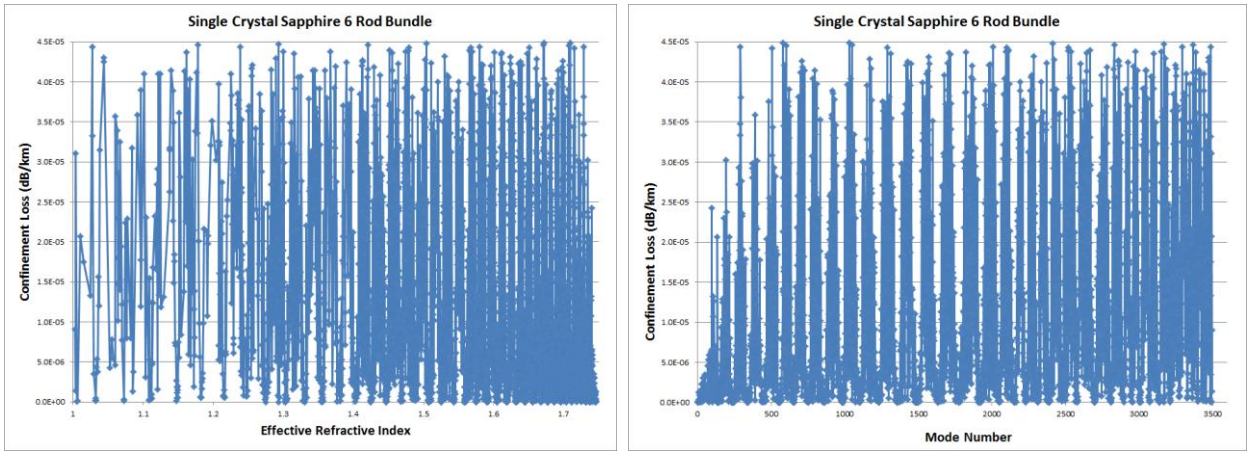

Figure 3.35 Confinement loss vs. effective refractive index(left) and mode number (right) for the 6-rod bundle of single crystal sapphire

In summary, Comsol Multiphysics 4.2a was used to examine both a single rod of single crystal sapphire with a core diameter of 50 μm and also a 6-rod structure consisting of 5 rods, with diameters of 70 μm, surrounding a central rod with a diameter of 50 μm all made of single crystal sapphire fiber. This work enables alternate fiber designs to be tested without having to fabricate the fibers, saving time and money. Fiber designs such as this will continue to be examined due to a large need for temperature and pressure fiber optic sensors that can operate in

harsh high temperature environments. The 6-rod case shows a modal reduction percent difference of 18.48% from the single rod of single crystal sapphire fiber. In addition to the advantages mentioned above for providing a cladding to the sapphire fiber, a reduction in the number of modes in these fibers increases the ease of fabrication of single crystal sapphire optical interferometers.

3.7 Photonic Band Gap Modeling

3.7.1 Experimental

The MIT Photonic Bands program (MPB) allows users to compute the eigenstates and eigenvalues of Maxwell's equations for plane waves in the frequency domain. The goal with this program is to successfully predict the feasibility of creating a photonic band gap with a 7-rod single crystal sapphire fiber bundle in air. If this is not possible, new designs will be analyzed to determine where a photonic band gap would exist if the structure can be fabricated.

The MBP program begins with setting the number of bands for each **k** point. For the models in this section, the number of bands is chosen to be 8, which is a common number of eigenstates for a hexagonal lattice structure. Next, the **k** points, often called Bloch wavevectors, at which the bands will be solved are set as the corners of the irreducible Brillouin zone (known as Γ, M, and K as seen in Figure 2.6). The basis size is chosen in order to maintain a hexagonal structure. This gives a basis of $(2/\sqrt{3}, 0.5)$, $(2/\sqrt{3}, -0.5)$ with the z direction being zero due to this being modeled as a 2D structure. Next the **k** points are linearly interpolated and the lattice directions are chosen. The geometry, grid size, and spacing of the rods in the fiber are then selected as functions of a. This is because Maxwell's equations are scale invariant, where a is the spacing

between rods or air holes, also called the lattice parameter or pitch. The radius of the rods or air holes, *r*, is scaled with *a* so that the correct 7-rod structure as we see in Figure 3.22 (left) can be obtained. For the case of a 7-rod structure with all of the rods touching in a hexagonal shape, *r* = 0.35 with *a* = 1 giving an equivalent structure to a fiber having a hexagonal arrangement with all rods touching with each rod being 70 μm in diameter. The resolution is set to 32, which results in a 32 x 32 computational grid for all of the structures analyzed in this section in order to obtain reasonable accuracy. The $\mathbf{k}_z$ out of plane propagation has not been considered in this case due to its complexity and limited usage in PBGF modeling. MPB uses a dielectric constant for the materials in the model and thus the dielectric constant for air $\varepsilon_{air} = 1.0$ and the dielectric constant for single crystal sapphire parallel to the C-axis taken from Kyocera[71] is $\varepsilon_{sapphire} = 11.5$ Linux MPB code for this fiber structure can be seen in Appendix A. The image of the resultant fiber structure can be seen in Figure 3.36 below.

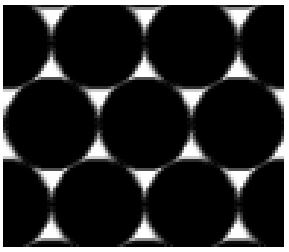

Figure 3.36 Output image from MPB code for the 7-rod structure of single crystal sapphire rods (black region) in a background matrix of air (white region) with *r/a* =0.5

3.7.2 Modeling Results

The TE and TM polarized modes can now be solved to output the band structure for the given fiber geometry. Figure 3.37 below shows the resultant TE modes while Figure 3.38 shows the TM polarized modes for the given structure in Figure 3.36 above.

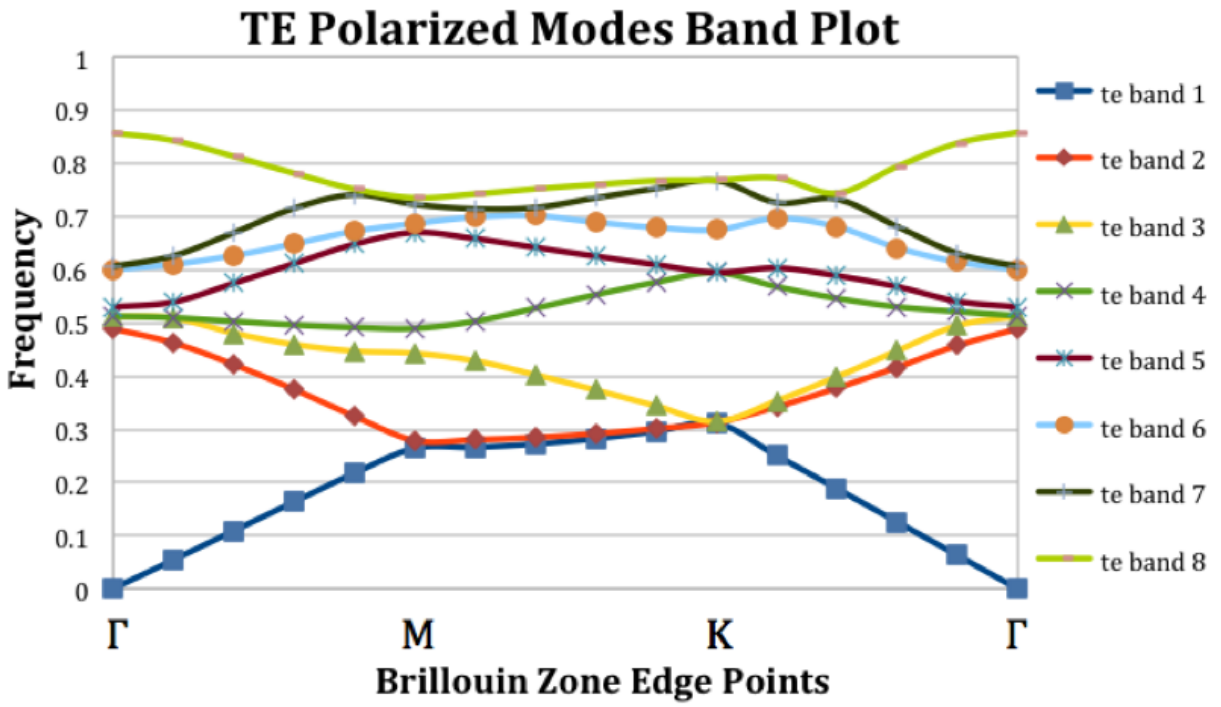

Figure 3.37 TE band gap plot of the frequency (in units of $\omega a/2\pi c$) versus the Brillouin zone edge points (M, K, and Γ) for the 7-rod structure of single crystal sapphire as seen in Figure 3.36 above

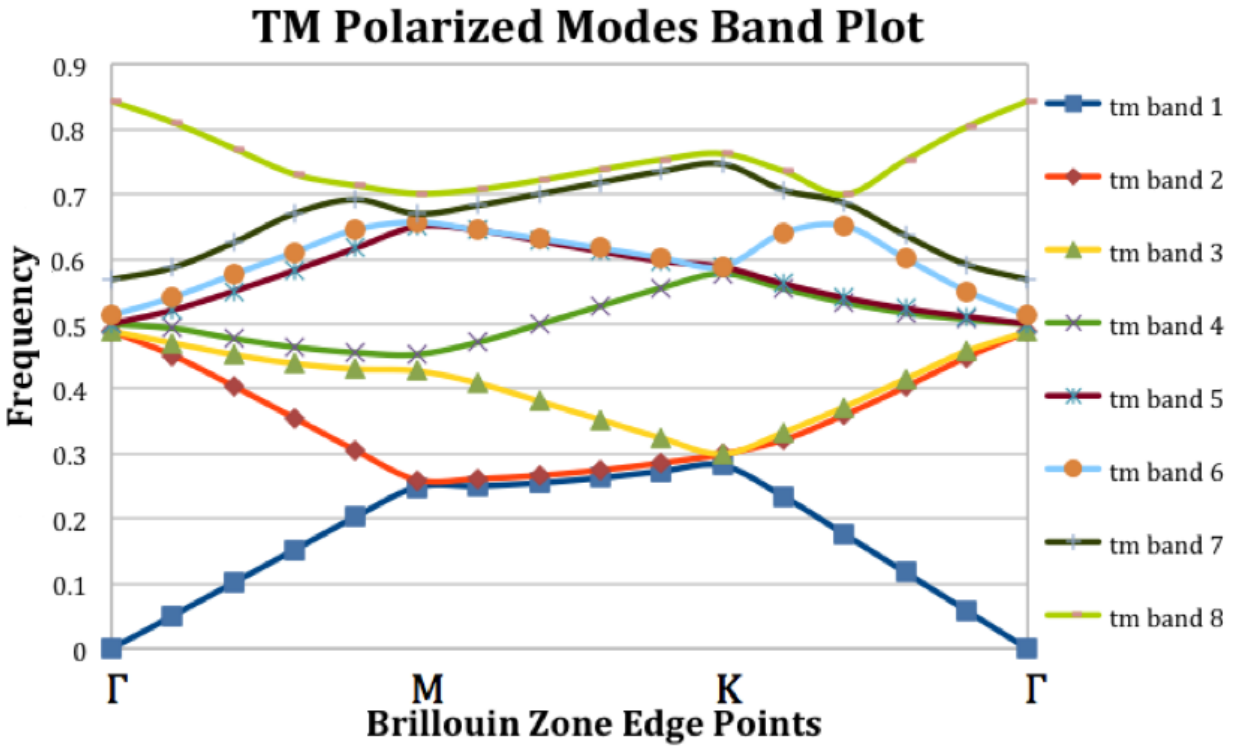

Figure 3.38 TM band gap plot of the frequency (in units of $\omega a/2\pi c$) versus the Brillouin zone edge points (M, K, and Γ) for the 7-rod structure of single crystal sapphire as seen in Figure 3.36 above

As noted in Section 2.8 MIT Photonic Bands, the edges of the Brillouin zone are denoted by the points by the M, K, and Γ points. From here we see that no band gap exists in either the TE or TM mode polarizations. This is due to the very small air fill fraction that is created when the sapphire rods are all touching in a hexagonal arrangement. This is typical for a rod type structure with a high dielectric contrast in a hexagonal arrangement[40].

Analysis of similar structures with a slightly different dielectric contrast (11.0) as in the MIT MPB tutorial[72] show that for a hexagonal array of high-index dielectric rods, a photonic band gap is present between the first (dielectric) band and the second (air) band for the TM modes. This is not the case for the TE modes for the same frequency as the TM gap. This results from the

lowest TM mode being localized in the high dielectric regions while most of the electromagnetic power of the air band is found in the lower dielectric regions of the air voids. This in turn increases the air fill fraction of the structure.

Now that the 7-rod bundled fiber made of all single crystal sapphire has been modeled, it is important to find what fiber designs will enable a partial or even a full TE and TM band gap. In order to do this, two distinct fiber designs were analyzed. The first was similar to our previous design of a 7-rod structure of sapphire rods in air, only with the radius and the spacing in between the rods changing in order to find a band gap. The second case consists of air holes in a background dielectric matrix of single crystal sapphire. This lattice of a high dielectric material is designed so that an almost isolated yet also connected structure consisting of triangular high ε-spots will be connected by narrow veins. A photonic band gap fiber using polycrystalline alumina as a background material with air holes in a hexagonal lattice orientation has already been demonstrated[40] so this design using single crystal sapphire should also produce a full band gap due to the similarity of dielectric constant between that of single crystal sapphire and polycrystalline alumina.

The first case examined has a 7-rod structure of sapphire rods in air, with the rod size changing from $r = 0.1$ with a respective basis size of $a = 0.2$ to a rod size of $r = 10$ with a respective basis size of $a = 20$. Maintaining the ratio $r/a = 0.5$ allows the various rod sizes when all of the 7 rods are touching one another to be visible. The ratio r/a is often called the air fill fraction when one of the dielectric constants is defined as air. Scaling of the rod size for five of the ratios analyzed can be seen in Figure 3.39 below. As in previous models, the dielectric constant for air is set to

$\varepsilon_{air} = 1.0$ and the dielectric constant for single crystal sapphire parallel to the C-axis is $\varepsilon_{sapphire} = 11.5$.

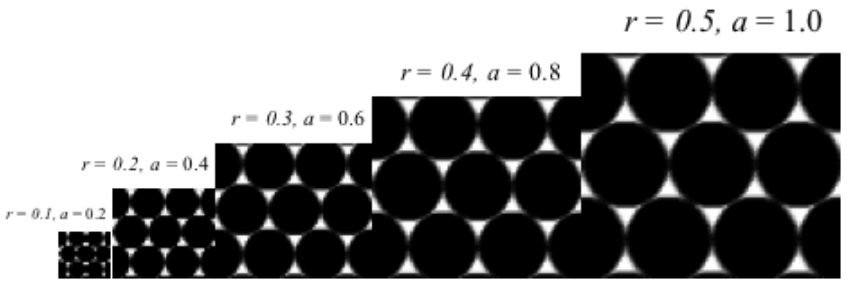

Figure 3.39 Images of five of the varied rod sizes analyzed with $r/a = 0.5$

Changing the rod radius and the lattice parameter with $r/a = 0.5$, we see that no band gaps exist for both TE and TM polarizations. This is mainly due to the large amount of sapphire and the minimal amount of air in this structure.

The next case examined has a 7-rod structure of sapphire rods in air, with the rod size kept constant at $r = 0.35$ while modifying the basis size from $a = 0.1$ to $a = 10$. By holding the rod size constant at $r = 0.35$, the ratio r/a scales the spacing between the rods. Scaling the rod spacing for five of the examined ratios can be seen in Figure 3.40 below. As in previous models, the dielectric constant for air is set to $\varepsilon_{air} = 1.0$ and the dielectric constant for single crystal sapphire parallel to the C-axis is $\varepsilon_{sapphire} = 11.5$.

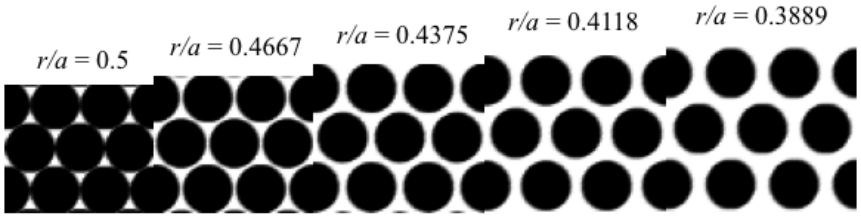

Figure 3.40 Images of five of the varied rod spacing's with $r = 0.35$

Changing the rod spacing we see that as the *r/a* ratio decreases, more TM band gaps are present. This directly correlates in a greater air fill fraction, which enables the large dielectric contrast between sapphire and air to produce a photonic band gap in one polarization. In this structure we see that the TM bands dominate in bands 1-2, 3-4, and 6-7, while small TE bands can be found from band 1-2 and band 4-5. This structure contains no full band gap. Table in Appendix B shows the rod size and spacing studied and whether a TE or TM band gap is present. The TE band data over the entire data range can be seen in Figure 3.41 and the TM is shown in Figure 3.42 respectively. Midgap frequency is defined as the average of the minimum and maximum frequency present where a band gap occurs. The bandgap percentage is defined as the change in frequency (maximum frequency at a band gap edge minus minimum frequency at a band gap edge) divided by the average of the minimum and maximum frequency present where a band gap occurs multiplied by 100. Both the bandgap percentage and the midgap frequency are unit-less due to Maxwell's equations being scale invariant.

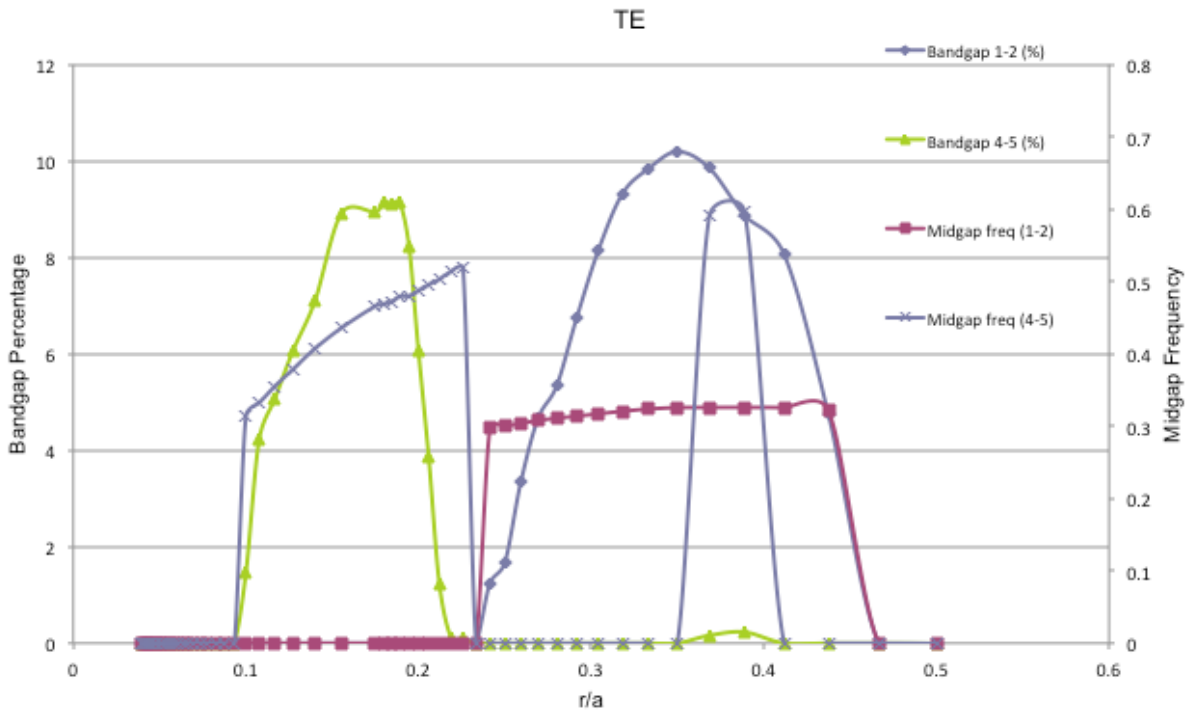

Figure 3.41 TE band profile for a structure with various rod spacing's while *r* is kept constant at *r* = 0.35

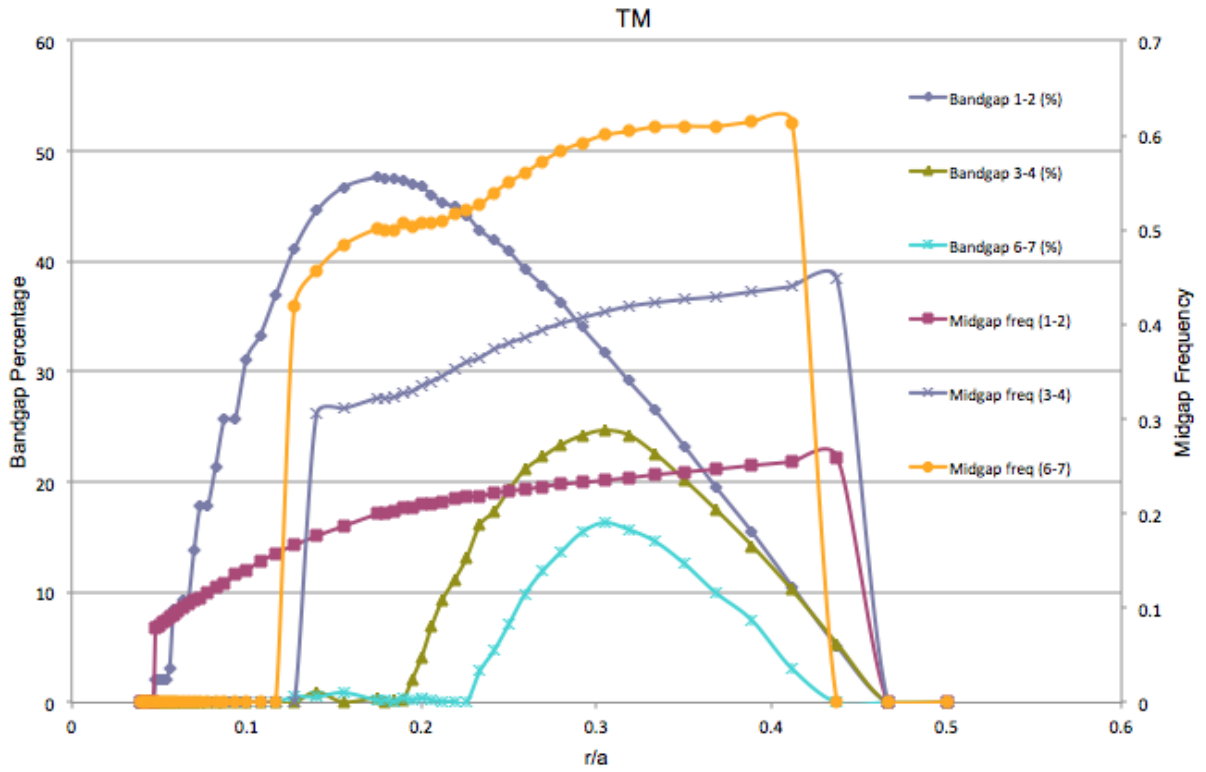

Figure 3.42 TM band profile for a structure with various rod spacing's while *r* is kept constant at *r* = 0.35

The next case examined consists of a 7-rod structure of sapphire rods in air, with the basis size *a* kept constant at *a* = 1.00 while modifying the rod radius from *r* = 0.1 to *r* = 0.5. By holding the basis size constant at *a* = 1.00, the ratio *r/a* scales the rod radius for a given spacing. Scaling the rod radius for five of the analyzed ratios can be seen in Figure 3.43 below. As in previous models, the dielectric constant for air is set to $\varepsilon_{air} = 1.0$ and the dielectric constant for single crystal sapphire parallel to the C-axis is $\varepsilon_{sapphire} = 11.5$.

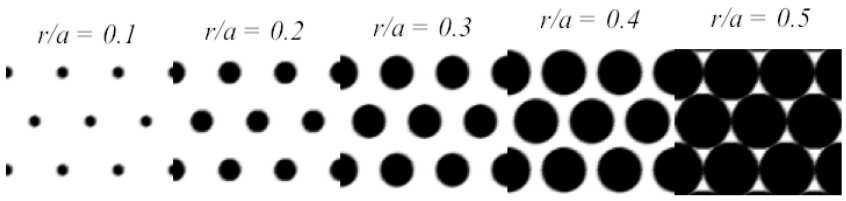

Figure 3.43 Images of five of the varied rod radius's with *a* = 1.00

Changing the rod spacing we see that as the *r/a* ratio decreases, more TM band gaps are present. This directly correlates in a greater air fill fraction, which enables the large dielectric contrast between sapphire and air to produce a photonic band gap in one polarization. In this structure we see that the TM bands dominate in bands 1-2, 3-4, and 6-7, while small TE bands can be found from band 1-2 and band 4-5. This structure also contains no full band gap. Table in Appendix B shows the rod size and spacing studied and whether a TE or TM band gap is present. The TE band data over the entire data range can be seen in Figure 3.44 and the TM is shown in Figure 3.45 respectively.

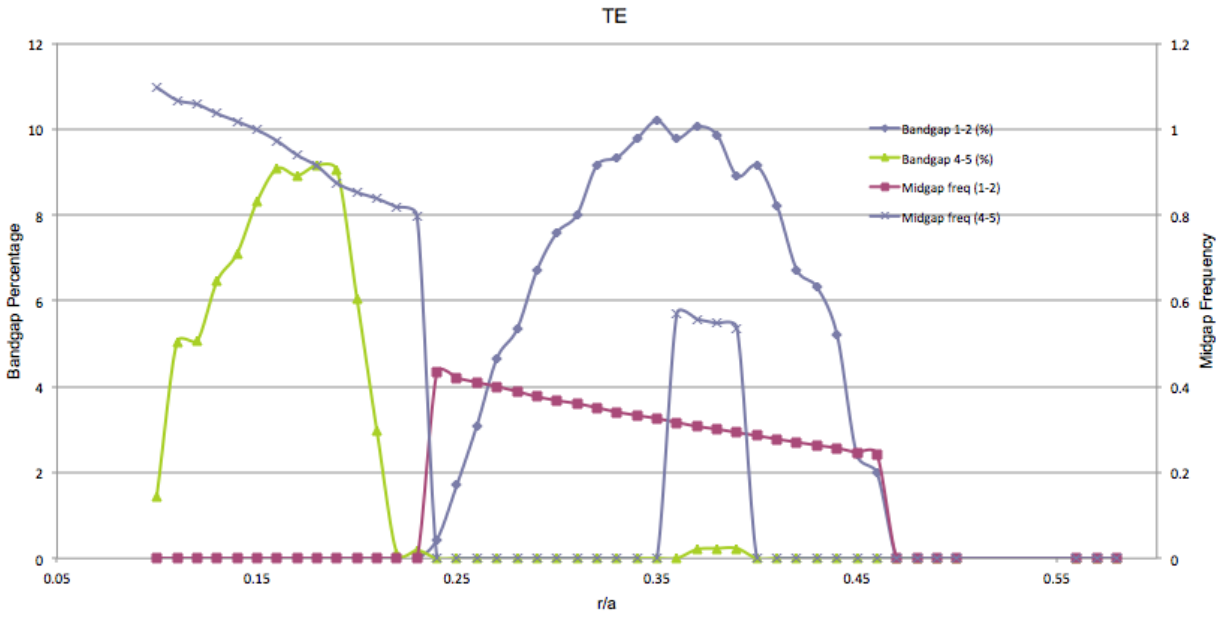

Figure 3.44 TE band profile for a structure with various rod radius's while *a* is kept constant at *a* = 1.00

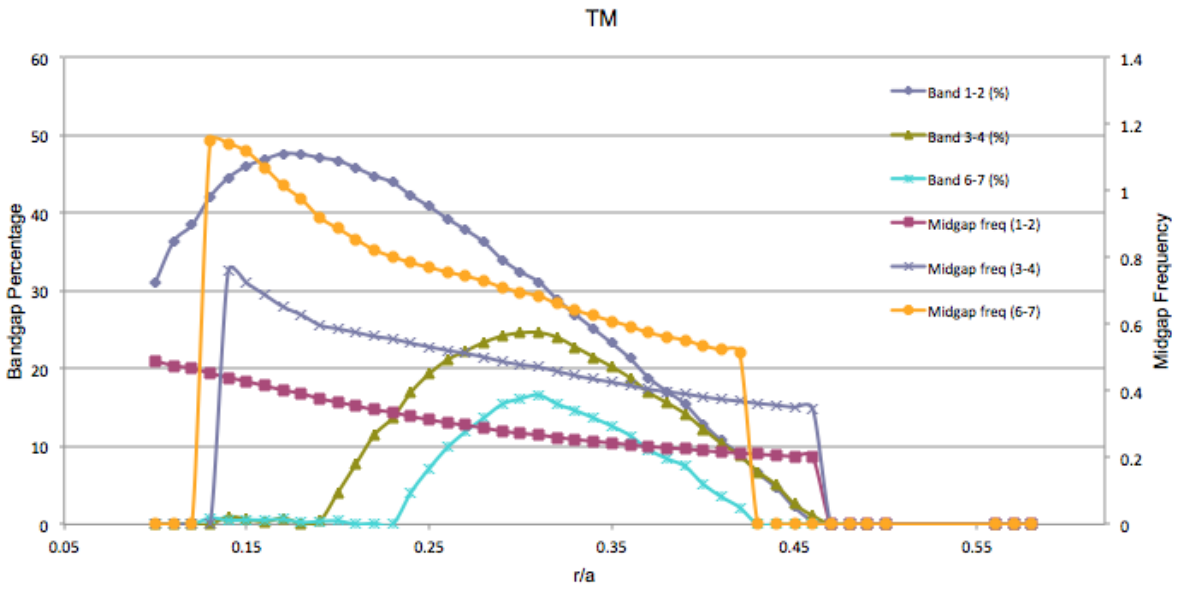

Figure 3.45 TM band profile for a structure with various rod radius's while *a* is kept constant at *a* = 1.00

The next case examined has a hexagonal structure of air holes surrounded in a background sapphire matrix. In this case the hole size changes from *r* = 0.1 with a respective basis size of *a* = 0.2 to a hole size of *r* = 10 with a respective basis size of *a* = 20. Maintaining the ratio *r/a* = 0.5 allows us to see various hole sizes when all of the 7 holes are touching one another. Scaling the hole size for the first five ratios can be seen in Figure below 3.46. As in previous models, the dielectric constant for air is set to $\varepsilon_{air} = 1.0$ and the dielectric constant for single crystal sapphire parallel to the C-axis is $\varepsilon_{sapphire} = 11.5$.

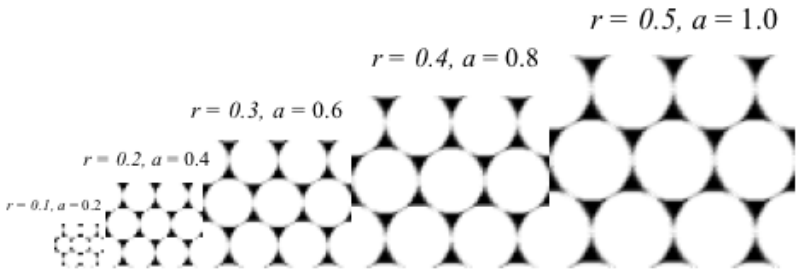

Figure 3.46 Images of five of the varied hole sizes with an *r/a* = 0.5

Changing the hole radius, we see that with a structure where all of the rods are touching (r/a = 0.5) we find that both TE and TM band gaps exist as well as a full band gap. This is mainly due to the high air fill fraction of the structure, which enables the large dielectric contrast between sapphire and air to produce a photonic band gap. Table in Appendix B shows the rod size and spacing studied and whether a TE or TM band gap is present. The TE band data over the entire data range can be seen in Figure 3.47 and the TM is shown in Figure 3.48 respectively.

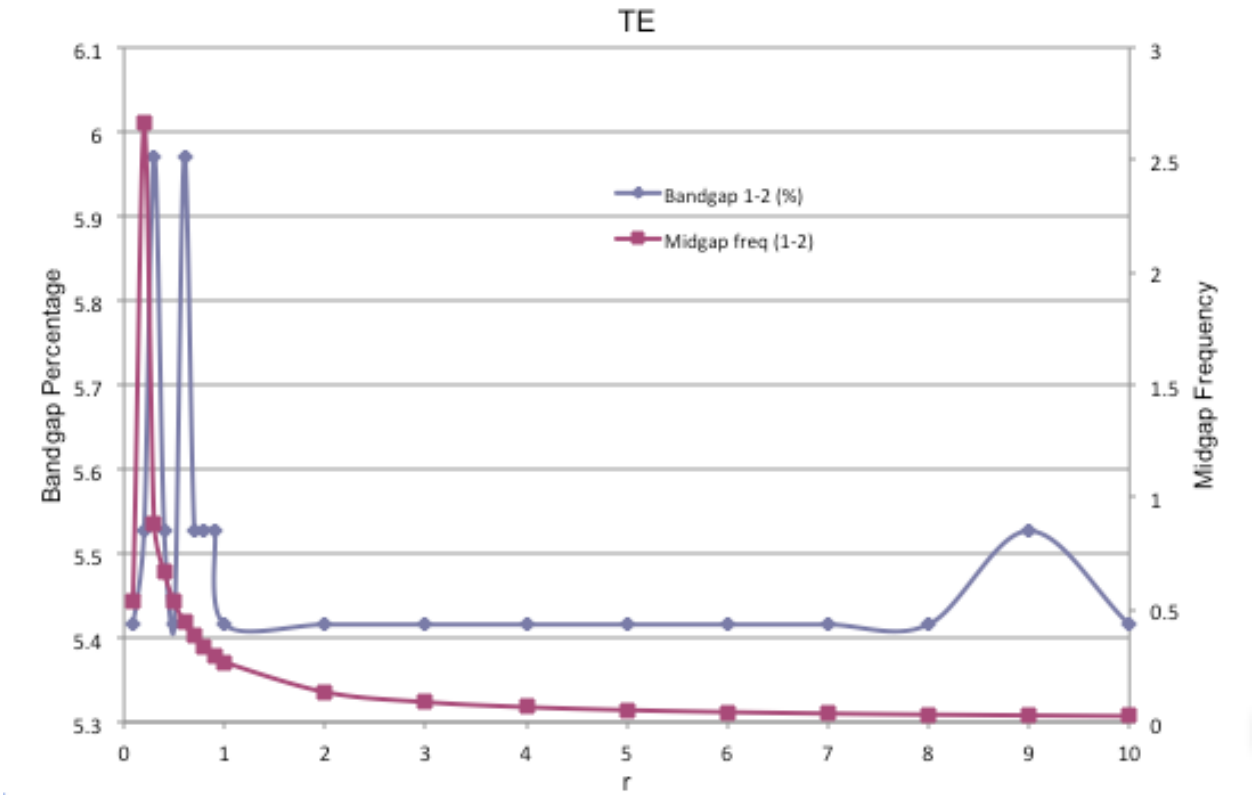

Figure 3.47 TE band profile for a structure with various hole sizes while maintaining the r/a = 0.5 ratio

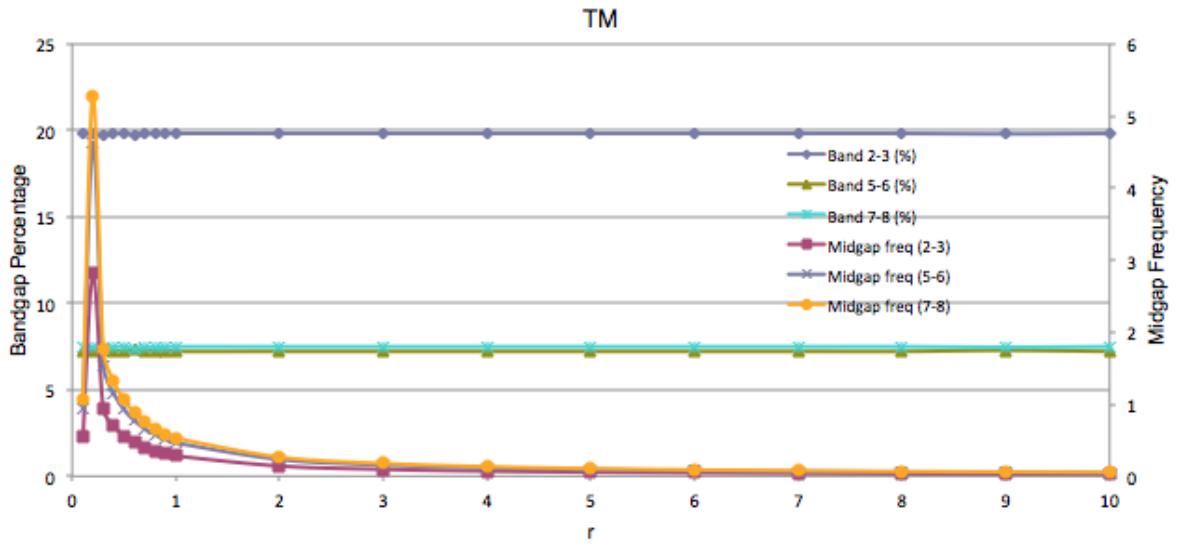

Figure 3.48 TM band profile for a structure with various hole sizes while maintaining the *r/a* = 0.5 ratio

The table for the full band gap can also be seen in Appendix B. A graph of the full band gap can be seen in Figure 3.49. This data shows the maximum full bandgap resides between the TE-1 and TE-2 bands at $r = 0.3$ and $a = 0.6$ with a bandgap percentage of 5.97% as seen in Figure 3.50. In order to convert the midgap frequency along the y-axis into a distinct wavelength one needs to simply multiply by a wavelength value which will determine the value of the lattice parameter *a*. The value of *r* can then be determined by the *r/a* ratio. An example of this would be in Figure 3.49 where the midgap frequency is equal to 2.7. If one wanted *a* to correspond to $\lambda = 1.55$ μm, one would use a lattice parameter $a = 2.7 * 1.55$ μm $= 4.185$ μm. Thus in the maximum bandgap case where $r = 0.3$ and $a = 0.6$, the radius then scales to $r = 2.0925$ μm.

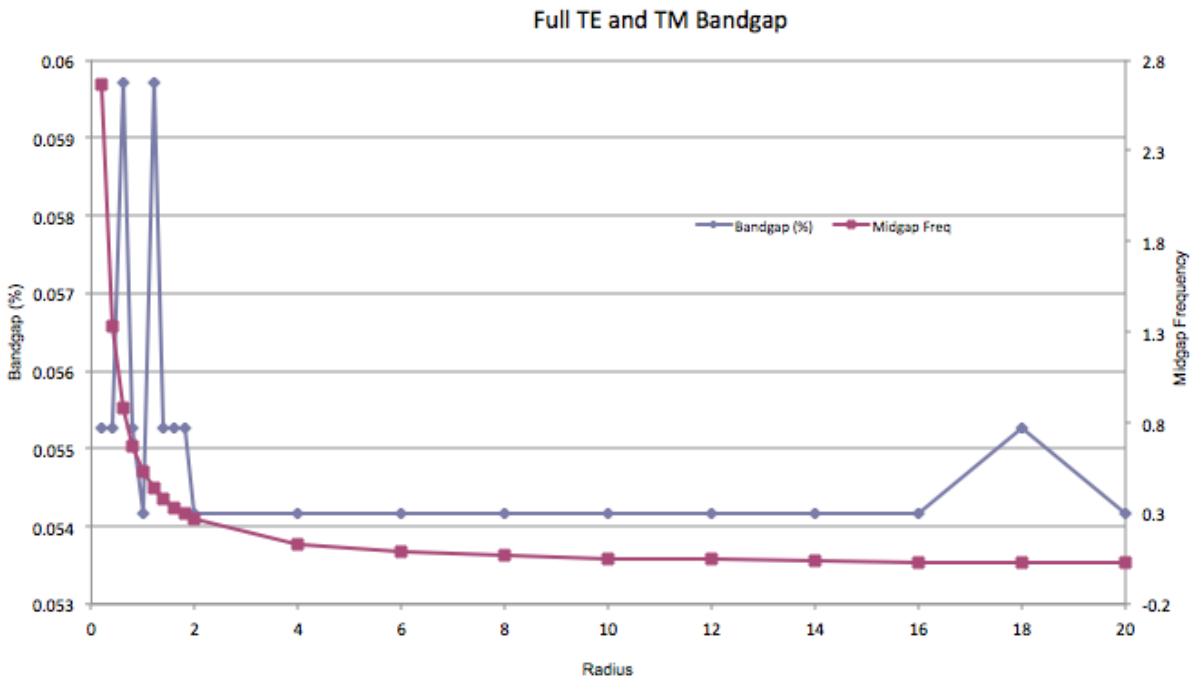

Figure 3.49 TE and TM full bandgap profile for a structure with various hole sizes while maintaining the $r/a = 0.5$ ratio

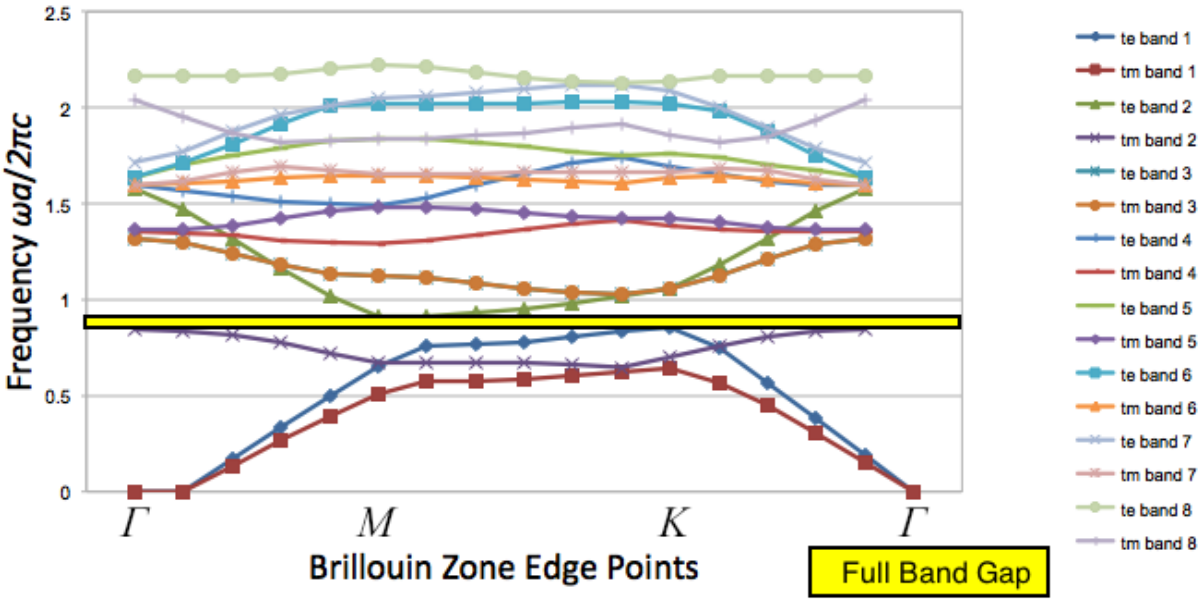

Figure 3.50 TE and TM full bandgap profile for a structure with $r = 0.3$ and $a = 0.6$

The next case examined has a hexagonal structure of air holes surrounded in a background sapphire matrix. In the case the radius of the holes was kept constant with $r = 0.35$ while the basis size was modified from $a = 0.1$ to $a = 10$. By holding the hole size constant at $r = 0.35$, the ratio r/a scales the spacing between the holes. Scaling the hole spacing for the first five ratios can be seen in Figure 3.51 below. As in previous models, the dielectric constant for air is set to $\varepsilon_{air} = 1.0$ and the dielectric constant for single crystal sapphire parallel to the C-axis is $\varepsilon_{sapphire} = 11.5$.

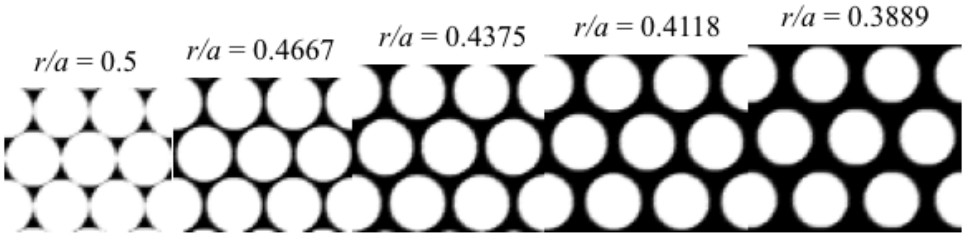

Figure 3.51 Images of five of the varied hole spacing's with $r = 0.35$

Changing the rod spacing we see that as the r/a ratio decreases more TM band gaps disappear. This directly correlates in a greater air fill fraction, which enables the large dielectric contrast between sapphire and air to produce a photonic band gap in one polarization. This test shows a much larger TE gap in band 1-2, with a smaller gap in band 7-8. The TM gaps are present, but are much smaller than the TE polarization and occur mainly between bands 2-3, 5-6, and 7-8. Table in Appendix B shows the rod size and spacing studied and whether a TE or TM band gap is present. The TE band data over the entire data range can be seen in Figure 3.52 and the TM is shown in Figure 3.53 respectively.

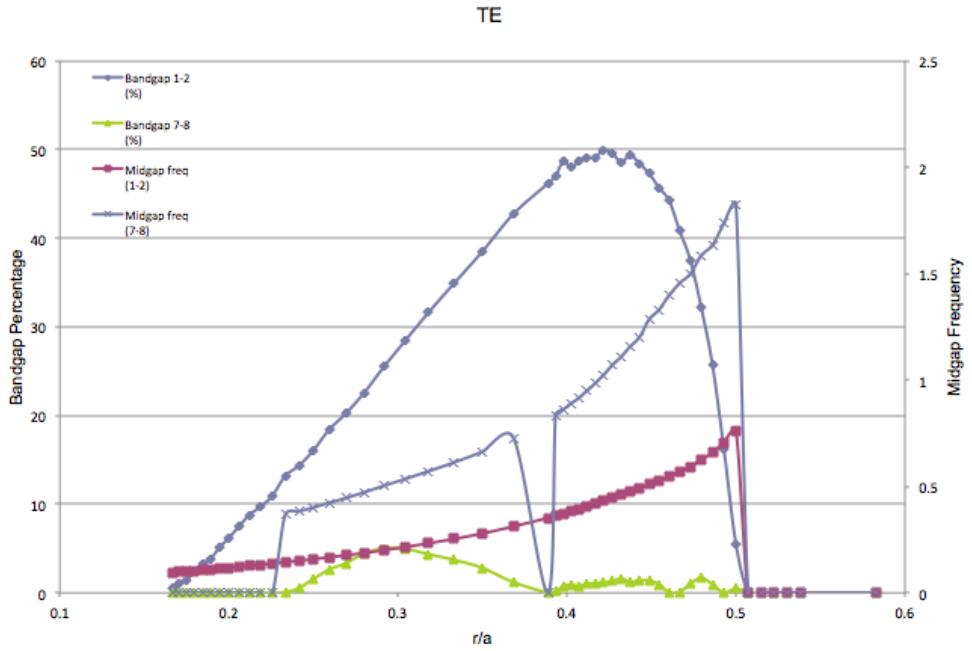

Figure 3.52 TE band profile for a structure with various rod spacing's while *r* is kept constant at *r* = 0.35

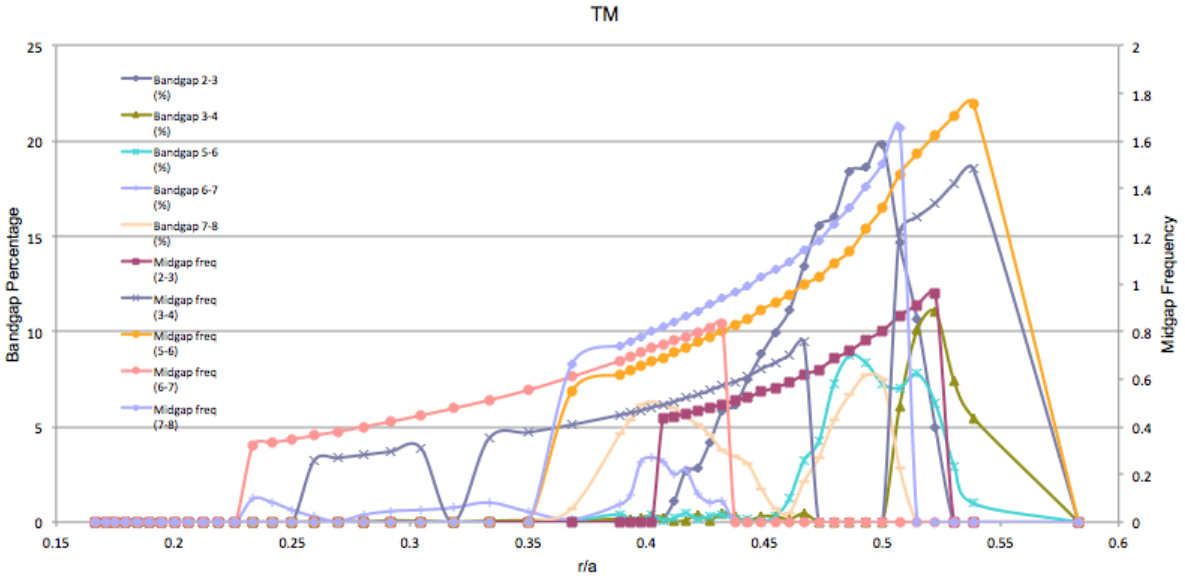

Figure 3.53 TM band profile for a structure with various rod spacing's while *r* is kept constant at *r* = 0.35

The table for the full band gap can also be seen in Appendix B. A graph of the full band gap can be seen in Figure 3.54. This data shows the maximum full bandgap resides between the TM-2

and TM-3 bands at $r = 0.35$ and $a = 0.74$ with a bandgap percentage of 15.551% as seen in Figure 3.55.

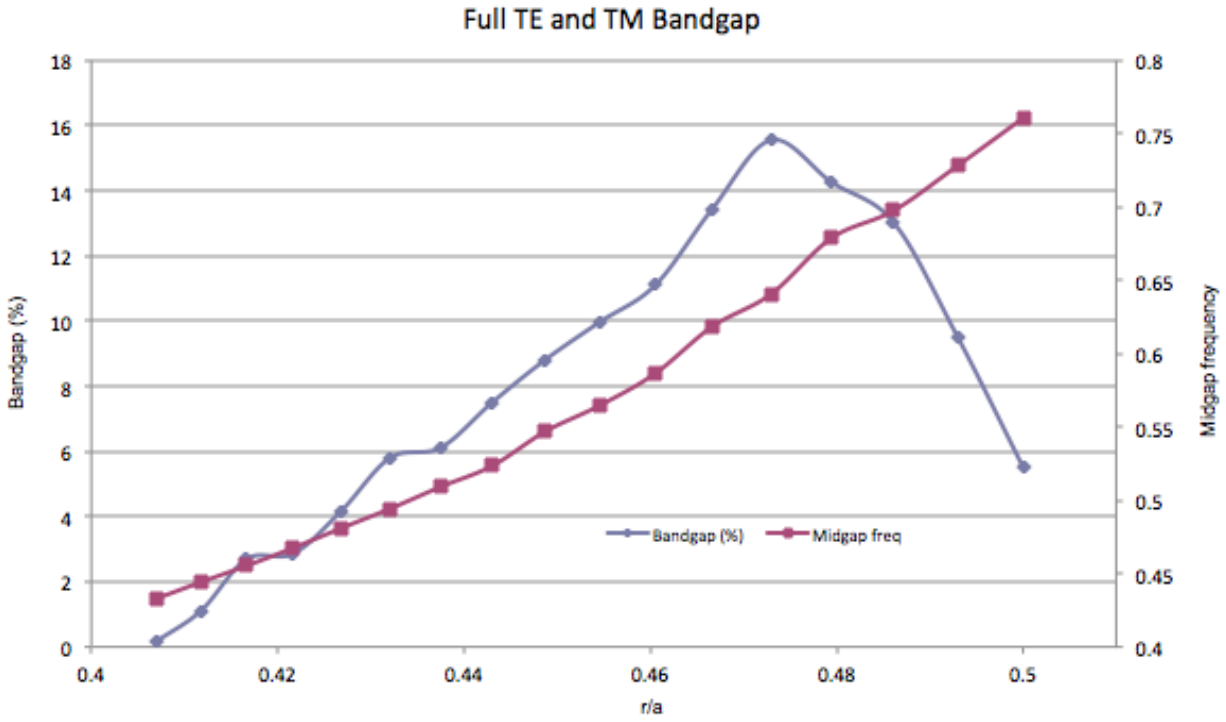

Figure 3.54 TE and TM full bandgap profile for a structure with various rod spacing's while r is kept constant at $r = 0.35$

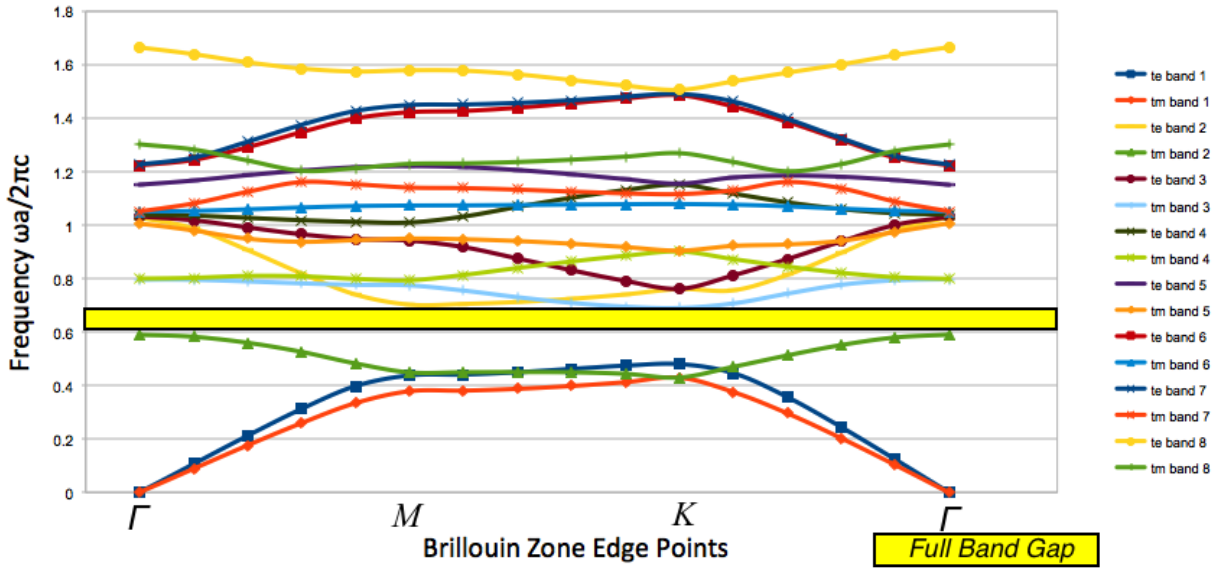

Figure 3.55 TE and TM full bandgap profile for a structure with r = 0.35 and a = 0.74

The final case examined has a hexagonal structure of air holes surrounded in a background sapphire matrix with the basis size *a* kept constant at $a = 1.00$ while modifying the hole radius from $r = 0.1$ to $r = 0.5$. By holding the basis size constant at $a = 1.00$, the ratio r/a scales the hole radius for a given spacing. Scaling the hole radius for five of the analyzed ratios can be seen in Figure 3.56. As in previous models, the dielectric constant for air is set to $\varepsilon_{air} = 1.0$ and the dielectric constant for single crystal sapphire parallel to the C-axis is $\varepsilon_{sapphire} = 11.5$.

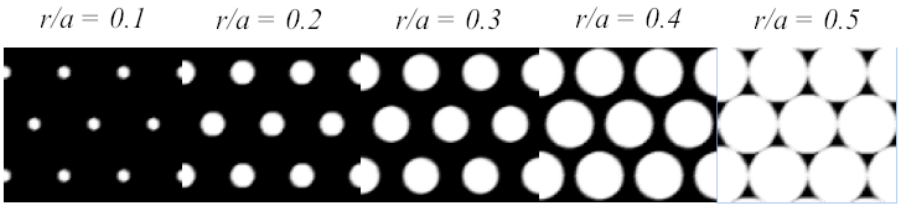

Figure 3.56 Images of five of the varied hole radius's from to $r = 0.1$ to 0.5 with $a = 1.0$

Changing the hole radius we see that as in the last two tests the TE polarization dominates. A large TE polarization gap can be seen between bands 1-2 with a smaller gap between bands 7-8. The TM polarization has the majority of its gaps opening up in the *r/a* >0.4 region with gaps seen between bands 2-3, 5-6, 6-7, and 7-8. Table in Appendix B shows the rod size and spacing studied and whether a TE or TM band gap is present. The TE band data over the entire data range can be seen in Figure 3.57 and the TM is shown in Figure 3.58 respectively.

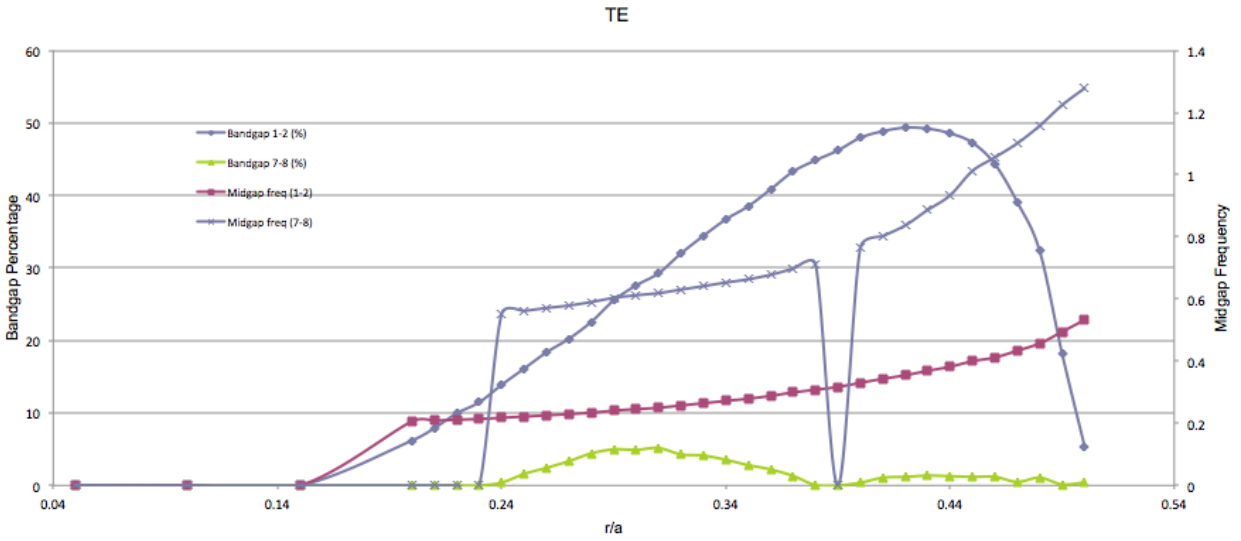

Figure 3.57 TE band profile for a structure with various hole radius while *a* is kept constant at *a* = 1.0

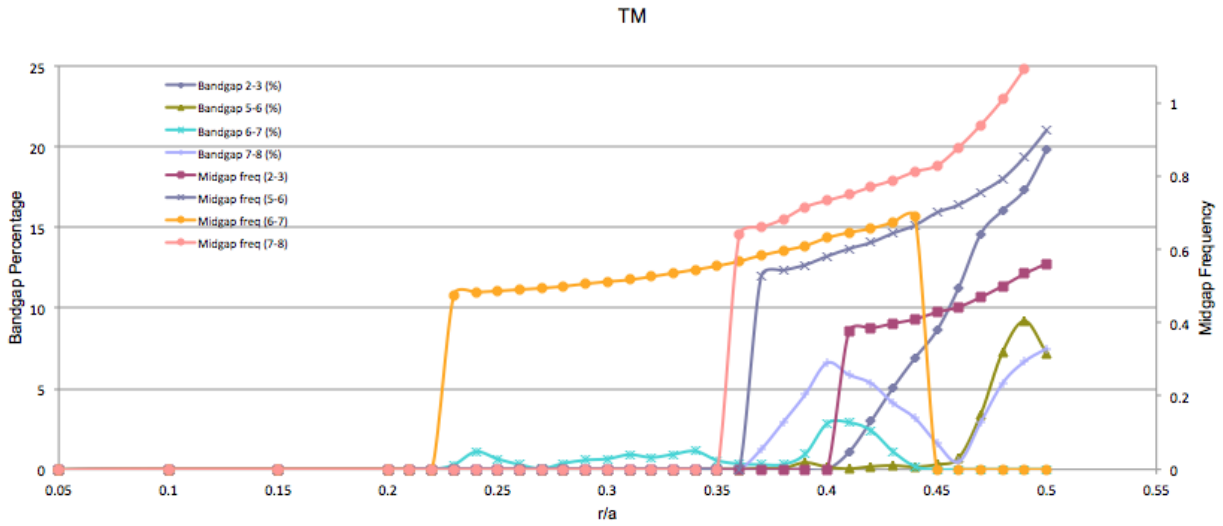

Figure 3.58 TM band profile for a structure with various hole radius while *a* is kept constant at *a* = 1.0

The table for the full band gap can also be seen in Appendix B. A graph of the full band gap can be seen in Figure 3.59. This data shows the maximum full bandgap resides between the TE-2 and TM-2 bands at $r = 0.49$ and $a = 1.00$ with a bandgap percentage of 17.5% as seen in Figure 3.60. This is the maximum bandgap structure possible for air holes in a background matrix of single crystal sapphire.

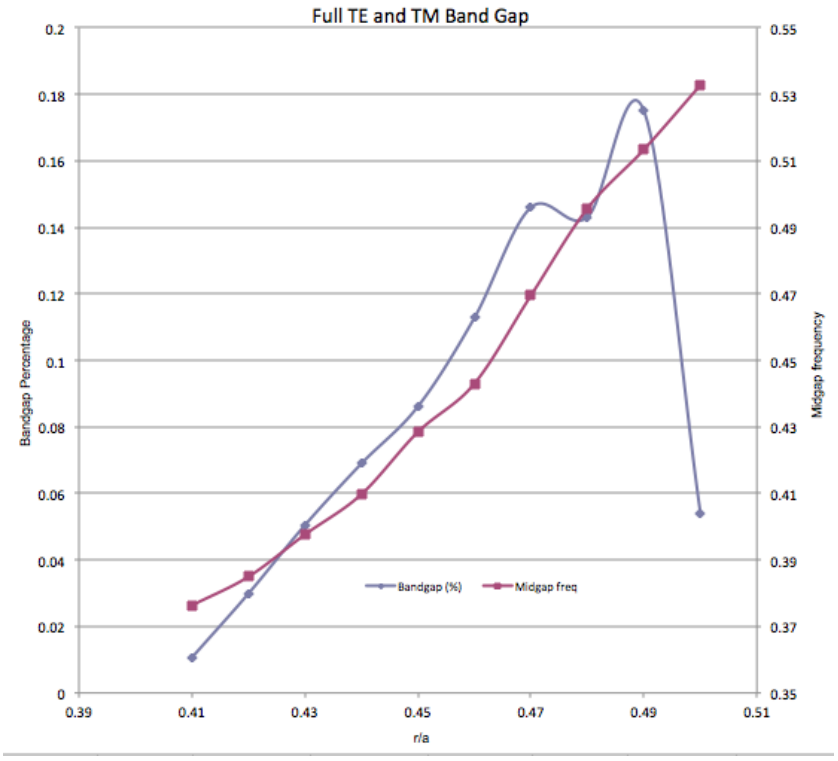

Figure 3.59 TE and TM full bandgap profile for a structure with various hole radius while a is kept constant at $a = 1.0$

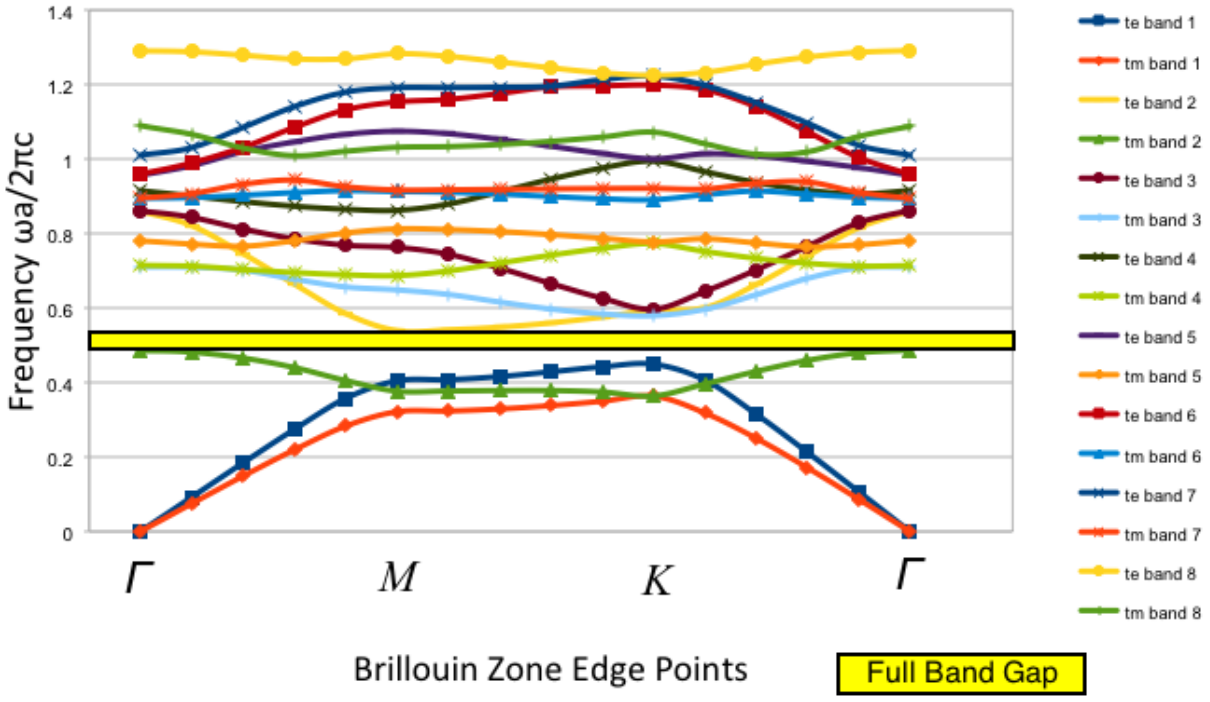

Figure 3.60 TE and TM full bandgap profile for a structure with at $r = 0.49$ and $a = 1.00$

A photonic band gap structure of air holes in a background matrix of silica was also analyzed for comparison purposes. This shows how the frequency range of a photonic band gap of air holes in silica is shifted compared to that of air holes in single crystal sapphire. A TE band plot can be seen for a structure consisting of a triangular lattice of air holes with radius $r = 3.9$ and with $a = 8.66$ with $r/a = 0.45$ which is the maximum gap for silica as seen by West et al.[73] in Figure 3.61. This plot also shows the hole radius structure in the bottom right hand corner. This structure shows the band gap midgap frequency of 0.05764 ($\omega a/2\pi c$, which is equivalent to a/λ) which is almost a factor or 10 different than that of the sapphire air holes case which has a maximum midgap frequency of 0.52 ($\omega a/2\pi c$). As an example, if the lattice parameter a=1.0 µm, the wavelength of bandgap operation would correspond to approximately 17 µm for the silica case and 1.923 µm for the single crystal sapphire case.

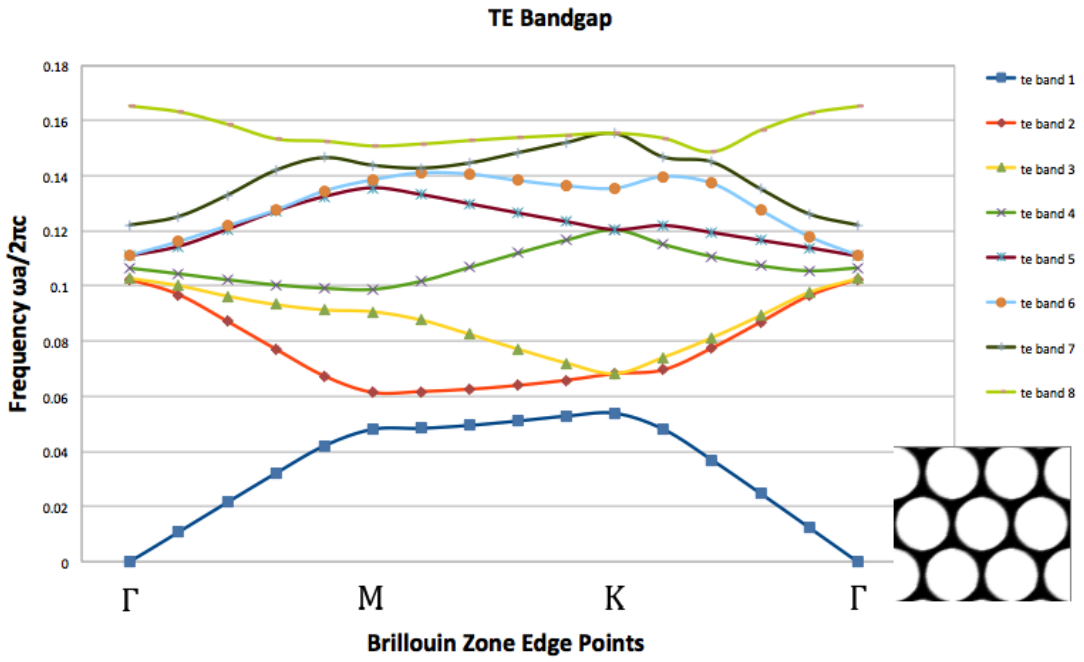

Figure 3.61 TE bandgap profile for a silica air hole structure with at $r = 3.9$ and $a = 8.66$

In summary, the work in this section proves that a complete band gap is possible for certain air hole designs with a background matrix of sapphire. The future work associated with this section is to begin attempting a structure that could potentially guide both TE and TM polarized light for a wide range of wavelengths. The bandgap range allows for larger, easier to fabricate fiber designs which are able to operate near common telecommunication frequencies. These fibers could potentially be fabricated using smaller scale sapphire tubes if this technology becomes readily available but much work needs to be completed before a useful fiber could be realized.

4. Experimental Procedures

4.1 7-Rod Silica Bundled Fiber

4.1.1 Fabrication

Silica fibers, with an outer diameter of approximately 70 µm, were cleaved into 7 pieces and polished with diamond grit paper starting with a 15 µm grit and finishing with a 0.5 µm grit. Each unclad fiber of silica was approximately 50 cm in length. The fibers were cleaned using distilled water and acetone, to remove any residual contaminants from the fibers. One of the seven cleaved fibers was fusion spliced to a 62.5 µm multimode graded-index silica fiber, which served as the lead in fiber. The lead in fiber was then fusion spliced to a 100 µm core, 140 µm cladding multimode silica fiber which connected to a miniature spectrometer (OceanOptics, Inc., USB2000). A diagram of this setup can be seen in Figure 4.1 below.

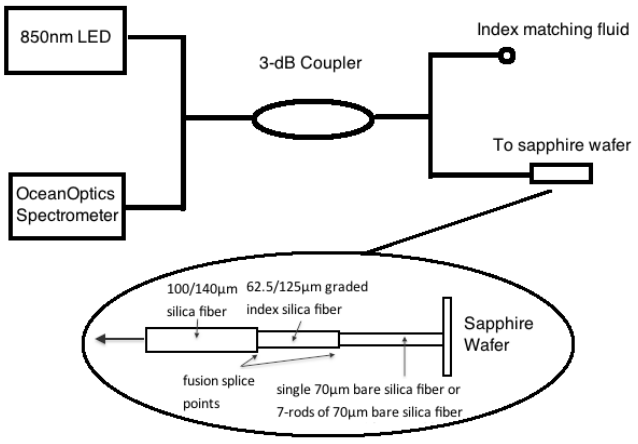

Figure 4.1 White light interferometric setup for both the single rod of silica and the bundled silica fiber

A C-plane (0001) sapphire wafer 59 µm thick and 1 mm x 1 mm in size was then glued onto a polished borosilicate tube. The tube was then secured to an optical goniometer attached to a 3D

stage so that precise angles could be adjusted for the incoming fiber. Light from an 850 nm LED was then launched into the 62.5 µm multimode graded-index silica fiber, which propagated through the bare silica fiber to the sapphire wafer through a 3 dB coupler. A schematic of this process can be seen in Figure 4.1. The bare silica fiber was then aligned and brought towards the sapphire wafer until it was within a few microns from touching the wafer.

Fringe visibility is defined[74] as Equation 30 which states:

$$Fringe\ Visibility = \frac{(Imax - Imin)}{(Imax + Imin)} \tag{30}$$

where I_{max} and I_{min} are the respective maximum and minimum intensities as seen in Figure 4.2.

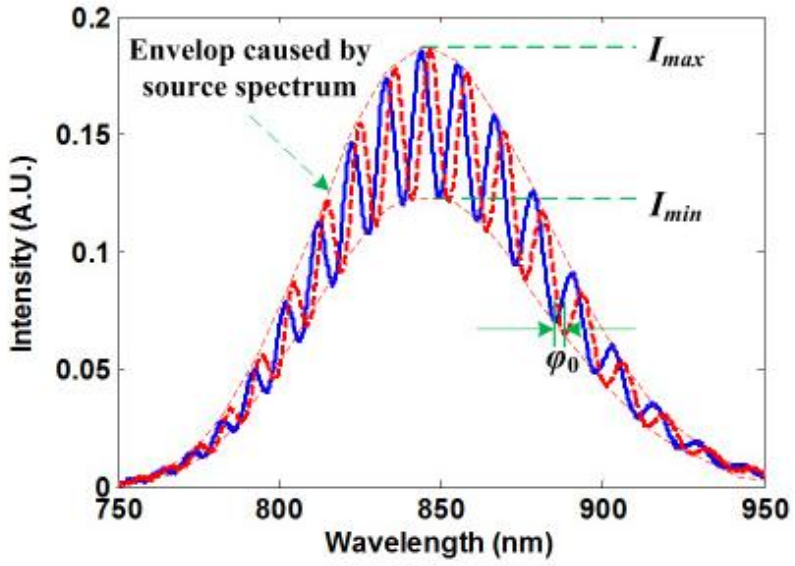

Figure 4.2 Sensor spectrum used to calculate the fringe visibility used from reference [74] with permission

Figure 4.2 also shows the $\varphi_{0,}$ which is defined as the additional phase component. The total phase shift of the sinusoidal spectrum, Φ, as a result of a temperature or pressure change is defined[74] by Equation 31:

$$\Phi = k * OPD + \varphi_0 \tag{31}$$

where k is the wavenumber and OPD is the optical path length difference. After multiple angular adjustments, the fringe visibility of the single bare rod of silica was optimized and the results were calculated using Equation 30 with Matlab. This process was repeated 5 times for repeatability with each run time averaging over 10 minutes. The optical loss of the bare fiber was then tested using a ThorLabs PDA 36A Si switchable gain photodetector set to a gain of 60 dB.

The same single bare rod of silica was then surrounded by the 6 rods of bare silica fiber and bundled together using platinum wire. This ensured that the fusion-spliced rod carrying the signal from the white light LED did not change over the course of the experiment.

4.1.2 White Light Interferometry

The setup shown in Figure 4.1 was repeated for the 7-rod bundled fiber for the white light interferometry testing. The 7-rod bundled fiber was then aligned and brought towards the sapphire wafer until they were almost touching. Again, multiple angular adjustments were made until the fringe visibility of the 7-rod bundled fiber was generated using Equation 30. This process was repeated 5 times for repeatability with each run time averaging over 10 minutes.

The fringe visibility data for both the single rod and the 7-rod bundled fiber was then post-processed in Matlab.

4.1.3 Photodetector Measurements

The single rod and 7-rod bundled fiber with the same central core rod as in the single rod case were then tested for optical loss using a ThorLabs PDA 36A Si switchable gain photodetector set to a gain of 60 dB. The bundled fiber was then removed from the lead-in 62.5 μm multimode graded-index silica fiber and cleaved so that the power from the 850 nm LED could be measured through the fusion spliced 100 μm core 140 μm cladding multimode silica fiber fusion spliced to a 62.5 μm multimode graded-index silica fiber. The power data from the photodetector was post processed using Matlab so that the runs for the single rod of silica fiber, the 7-rod bundled fiber, and the power from the LED to the 100 μm core, 140 μm cladding multimode silica fiber fusion spliced to a 62.5 μm multimode graded-index silica fiber could be combined into one graph to show the change in optical output.

4.2 7-Rod Sapphire Photonic Crystal Fiber

4.2.1 Fabrication

Fabrication of the first sapphire photonic crystal fiber began with individual single crystal sapphire fibers with an outer diameter of approximately 70 μm. These fibers were cleaved into seven pieces approximately 15 cm each. The fibers were cleaned in a series of steps which included rinsing in alcohol, distilled water, acetone, and diluted phosphoric acid. The fibers were assembled in a pattern that consisted of a central fiber surrounded by six outer fibers,

forming a symmetric ring around the central fiber. A schematic of the fiber placement is shown in Figure 3.13 in Section 3.3 Sapphire Photonic Crystal Fibers.

The fibers were held in place by using platinum wire. The platinum wire was wound around the fibers in a manner to preserve the ordered arrangement of the fibers and was wound around the fiber in several locations across the entire length of the fibers. An example of the resultant bundled structure can be seen in Figure 4.3 below.

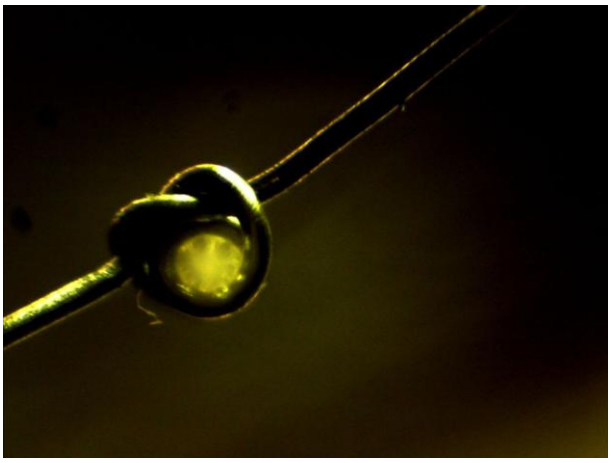

Figure 4.3 Image of the platinum wire holding the fiber in the correct arrangement

After the process was completed, the fibers were cleaned again using the same cleaning sequence previously outlined. The fiber bundle was then placed on a porous high purity alumina plate (Micromass, from Porvair Advanced Materials) and then inserted into a Deltech furnace. The fibers were heated at 1600 °C for 12 hours to remove any residual stresses from the bundling procedure. The fibers were then removed from the furnace and allowed to cool to room temperature. Polishing of the fibers was performed with diamond polishing paper of various

grits. In order to accomplish this, the fibers were mounted in a polishing fixture and bonded to it with a thermoplastic adhesive. The adhesive was later removed using acetone.

One of the key steps in the design of longer lengths of the 7-rod single crystal sapphire fiber bundle is the fabrication of the fiber bundle itself. The sapphire rods in this section were made by Micromaterials Inc. and grown with the C-axis of the crystal extending along the length of the fiber. Fabrication of the first 50 cm long and 1 meter long sapphire photonic crystal fibers began with individual single crystal sapphire fibers with an outer diameter of approximately 70 μm. As in the 15 cm long structure, the longer length fibers were cleaned in a series of steps which included rinsing in alcohol, distilled water, acetone, and diluted phosphoric acid. The fibers were assembled in a pattern that consisted of a central fiber surrounded by 6 outer fibers, forming a symmetric ring around the central fiber. A schematic of the fiber design and placement can again be seen in Figure 3.13 in Section 3.3 Sapphire Photonic Crystal Fibers.

The fiber bundle consists of seven fibers arranged in a hexagonal shape with one of the fibers directly in the center of the bundle. This creates a cladding that will maintain all of the chemical and physical property characteristics that an individual sapphire fiber would with the added benefit of core protection. The orientation of the fibers in a hexagonal shape was accomplished by threading the seven single crystal sapphire rods inside a fiber funnel with a correct inner diameter. The single crystal sapphire fibers have an outer diameter (OD) of 70 μm so the desired inner diameter of the silica funnel to produce the correct hexagonal arrangement would be three fiber OD's across. This was accomplished by polishing the tapered end of a silica funnel until an uncoated individual silica test fiber with an OD of 210 μm could barely fit through.

Each sapphire fiber was then added to the funnel with the correct inner diameter (ID) so that the only shape it could make was the hexagonal shape with one fiber directly in the center as seen in Section 3.5.2, Figure 3.22 (left). Next the fibers were adjusted so that they were all the same length at the end face. Then a knot was carefully tied using platinum wire to secure the fiber bundle just outside of the glass funnel to keep the bundle in the correct hexagonal arrangement across the entire length of the entire fiber bundle. A mechanical tweezer arm was used to aid in the fiber tying process. This bundling process can be seen in Figure 4.4 below.

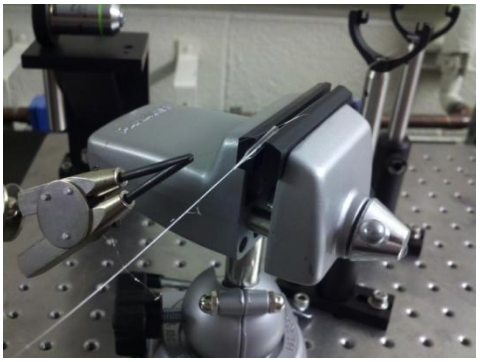

Figure 4.4 Bundling process using the greater than 210 µm ID fiber funnel at the tapered end to form the correct hexagonal structure

The fiber bundle was then pulled approximately 0.5 inches through the funnel and the process was repeated until the entire 50 cm or 1 m of fibers were in the correct arrangement. Great care had to be taken in this step as sapphire is very brittle. The bend radius to produce fracture is larger for sapphire than in silica so the fiber bundle was kept as straight as possible to avoid inducing any unwanted stress. After bundling, the fibers were cleaned in a series of steps which included rinsing in alcohol, distilled water, and acetone to remove any contaminants from the bundling process.

Various optical characterization techniques benefit from being fusion spliced to lead in or lead out fibers in order to minimize the reflections off of unwanted material interfaces. As seen in Section 2.9, white light interferometry is optimized when a lead-in fiber is fusion spliced rather than butt-coupled to the sensing fiber. A butt-coupled fiber would add a DC component to the background of the fringe visibility signal which would make the data post-processing more difficult. In order to fabricate a bundled fiber that is fusion spliced to a lead in fiber, a cautious fabrication approach had to be developed. A 50 cm long, 70 μm diameter single crystal sapphire fiber was first fusion spliced to a 100 μm core, 140 μm cladding graded index multimode silica fiber. This fiber was then placed next to six 45 cm long 70 μm diameter single crystal sapphire fibers and adjusted so that they were all the same length at the sapphire end face. The 50 cm long 70 μm diameter single crystal sapphire fiber that was fusion spliced to the 100 μm core/ 140 μm cladding graded index multimode silica fiber was then adjusted so that when all 7 sapphire rods were pushed through the silica fiber funnel, the fusion spliced fiber would be in the central core location. This was checked by aligning the silica end of the 100 μm core/ 140 μm cladding graded index multimode silica fiber to a 632.8 nm HeNe laser using a 3D stage as seen in Figure 4.5 below.

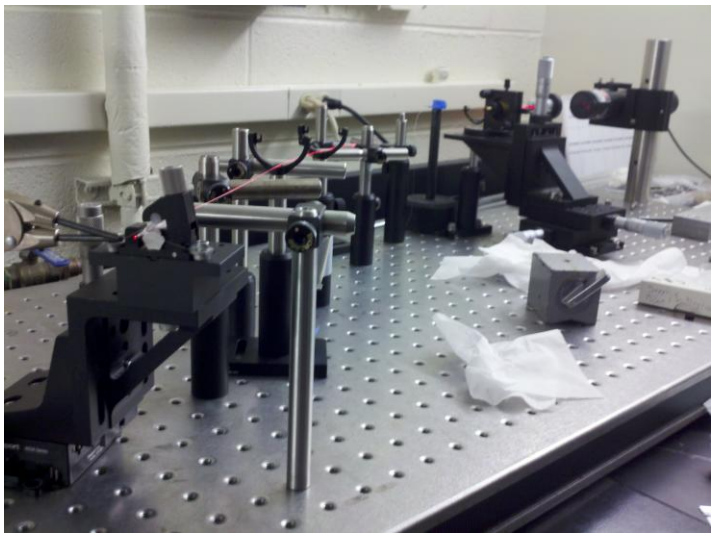

Figure 4.5 HeNe laser connection to determine if the fusion-spliced rod of sapphire is in the central core position of the fiber bundle

An adjustable microscope was then placed at the fiber funnel end of the sapphire fibers while the 632.8 nm HeNe laser was turned on. This confirmed that the fusion-spliced rod was in the correct central core location when illuminated. As in the previous fiber tying stages, a knot was carefully tied using platinum wire to secure the fiber bundle just outside of the glass funnel to keep the bundle in the correct hexagonal arrangement along the entire length of the entire fiber bundle. The fiber bundle was then pulled approximately 0.5 inches through the funnel and the process was repeated until the entire 50 cm length was tied in the correct hexagonal orientation.

Single crystal sapphire is a very hard material with a Knoop hardness of 2100 and a 9 on the Mohs scale. It is very difficult to polish due to its high mechanical strength. The easiest way to polish single crystal sapphire is through a variety of diamond lapping films starting with coarse grit and working towards fine grit. In all of the above fiber bundle lengths, the fiber bundle must be housed inside an array of protective silica tubes to give stability to the fiber bundle. The array

is held together by heating phenyl salicylate wax until it is liquid and then coating the inside of each array tube until the wax solidifies. When the wax solidifies, the fiber bundle will be fixed into place. It is also important to note that the bundle end face must remain as close to perpendicular as possible to get the best results during polishing. This is possible by using a level that is can accurately measure the angle of the fiber polisher. The silica tube array is then mounted in a metal v-shaped groove and is adhered into place using Crystal Bond. Once hardened, the Crystal Bond maintains the integrity of the entire bundle and the array of tubes. This ensures that the bundles' end face will remain perpendicular to the diamond lapping film.

The rotating plate of the fiber polisher first gets a few drops of water and then the 30 μm grit diamond film is placed on top. Decreasing the polishing grits from 30 μm grit to 9 μm to 3 μm and then finishing with 0.5 μm grit is the standard procedure to achieve the optimal fiber polish. The fiber bundle is cleaned with methyl alcohol to remove any polishing debris and then checked on an optical microscope before progressing to the next finer grit size to check the bundle's progress. The larger grit sizes generally require more time for optimal polishing compared to the fine diamond grit papers.

4.2.2 Characterization

As shown in the schematic of the fiber placement (Figure 3.13 in Section 3.3 Sapphire Photonic Crystal Fibers), the radius ratio of R_2 / R_1 would be 0.155. If the radius of the sapphire cylinders were 35 μm, then the radius of the holes would be approximately 5.4 μm. This again would be the upper bound on the hole size as sintering of the sapphire cylinders will tend to decrease the

size of the hole. End face images taken in reflected and transmitted white light were then preformed using an optical microscope.

4.2.3 Numerical Aperture

Numerical aperture (NA) is defined as the light gathering ability of an optical fiber. The equation for numerical aperture has been defined by Equation 28 in Section 3.5.1, but is also equivalent to:

$$\mathrm{NA} = n^{*}\sin(\theta) \tag{32}$$

Where n is the refractive index of the medium, and θ is the half angle of the maximum entrance or exit angle of the fiber. Equation 32 is only true if the numerical aperture (NA) is less than or equal to one. A NA greater than one means that rays incident on the end face of a fiber from all directions will be guided independent of the launch angle. In a real sapphire fiber, which is highly multimode, a more accurate numerical aperture equation is given as the effective numerical aperture $\mathrm{NA}_{\mathrm{eff}}$. This is because bulk defects and defects that are adsorbed onto the fiber surface scatter the input signal into larger angle, highly lossy modes[75]. $\mathrm{NA}_{\mathrm{eff}}$ is commonly defined[76] by:

$$NA_{\mathrm{eff}} = \sin(\theta_{5\%}) \tag{33}$$

where

$$\theta_{5\%} = \frac{\theta_{+} + \theta_{-}}{2} \tag{34}$$

with $\theta_{5\%}$ being the angle at which the angular intensity drops to 5% of the maximum reading at the zero degree angle.

Finding the effective numerical aperture (NA_{eff}) for the 1 m long single crystal rod of sapphire (70 µm diameter) and for the 1 m long 7-rod bundled fiber (with each rod being 70 µm diameter) was completed using a visible spectrum adjustable gain photodetector with up to 70 dB of adjustable gain (Thorlabs PDA36A) with a 5mW input HeNe laser which emits at 632.8 nm. The laser was focused into a 10x objective lens and into a 635 nm SMA fiber collimator with a NA = 0.25 and a focal length f = 35.41, which focused the input light through a 105/125 µm core/clad step index MMF. This fiber was aligned and butt coupled to the sapphire bundle using a fiber holder. The photodetector's acceptance angle was adjusted by rotating the platform around a fixed point (a screw that was 2.5 inches away) changing the resulting input angles.

4.2.4 Far Field Patterns

The goal of far field measurements is to show the reduction in the modal volume between a 7-rod bundle of single crystal sapphire versus a single rod of single crystal sapphire fiber both 1 m in length. The far field radiation pattern shows the distribution of irradiance as a function of angle with the z-axis of the optical fiber at a certain distance from the fiber end face. Images of the far-field pattern setup can be seen in Figure 4.6 below.

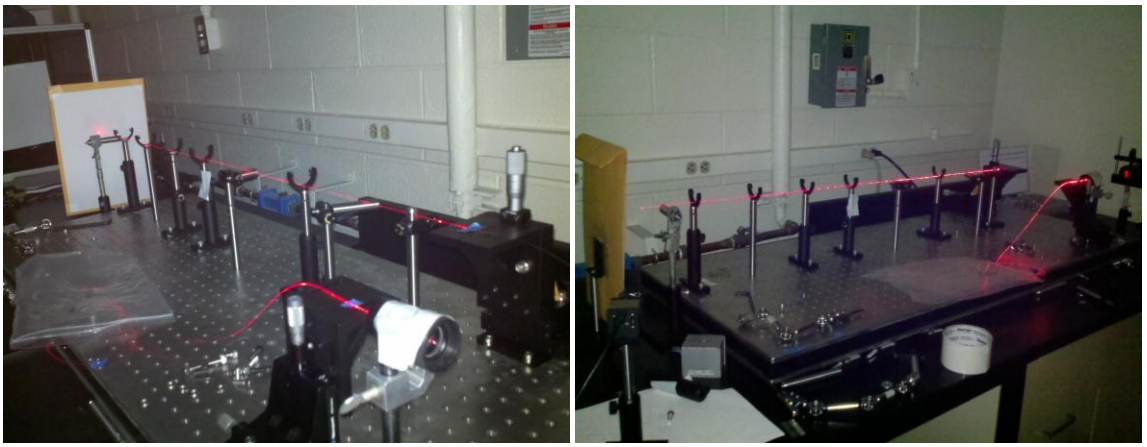

Figure 4.6 Far field imaging setup for all fibers tested

A single 70 μm diameter rod of single crystal sapphire was tested using a 5mW HeNe laser at 632.8 nm. A 20x microscope objective coupled the laser light into a Corning Infinicor 600 graded index multimode fiber with dimensions 50 μm core/125 μm cladding, which was then aligned and butt-coupled to the input sapphire fibers. The far field image speckle pattern could then be seen at a distance of 6 inches from the end of the fibers being studied. The far field pattern has an underfilled launch condition due to the 50 μm diameter core being smaller than that of the 70 μm diameter core of the fiber in this study. This concentrates the optical power in the center of the fiber and excites the lower-order modes more strongly. The 70 μm diameter fiber is highly multimode due to its refractive index difference between its core and cladding.

To calculate the number of modes that will propagate in both the 7-rod bundle of single crystal sapphire and the single rod case we again use Equation 28. As in Section 3.5.1, Comsol estimates the effective refractive index of this air-sapphire region surrounding the core for the 7-rod bundle to be $n_{c\ bundle} \approx 1.7147$. The refractive index for the cladding in the single rod case $n_{c\ single}$ equal to 1.0. The core refractive index in both cases has $n_f = 1.74618$. After solving Equation 28 for both the 7-rod bundled fiber and the single rod case, we find the 7-rod bundled

fiber has a NA = 0.330 with the single rod case having a NA = 1.4315. We then use the NA values to find the respective number of modes for each fiber by using Equation 27 at a wavelength of 632.8 nm. For the 7-rod bundled case Nm is given by Equation 35 with the core diameter D = 70 μm.

$$Nm = 0.5 * \left(\frac{\pi * D * (0.330)}{632.8\, nm}\right)^2 \quad (35)$$

Equation 35 gives us $Nm = 6575.98$ for the 7-rod bundled case. For the single rod case Nm is given by Equation 36 with the core diameter D = 70 μm.

$$Nm = 0.5 * \left(\frac{\pi * D * (1.4315)}{632.8\, nm}\right)^2 \quad (36)$$

Equation 36 gives us $Nm = 123742.0$ for the single rod case. Equations 35 and 36 show a percent decrease in the number of modes for the 7-rod bundle of approximately 95%. This large percent reduction stems from the fact that the NA value for the single rod case is > 1.0, which limits the accuracy of this result.

4.2.5 Gas sensing

Gas sensing experiments using the 7-rod sapphire bundle have been examined and tested in various lengths. It was discovered that this fiber was a poor evanescent wave gas sensor when the input light was injected into the fiber rods. This is due to the strong modal confinement of higher order modes to the core region due to the high dielectric contrast between the single

crystal sapphire fiber and the air surrounding it. In order to remedy this, it was proposed to guide light in the air regions in-between the fiber rods in order to have as much interaction time with the gaseous environment as possible. This functions similarly to the hollow core waveguide gas sensors discussed in Section 2.10 Gas Sensing. This process was simplified to better understand how the propagation within one of these air holes is contained by making a 1.5 inch long 3-rod single crystal sapphire bundle. An image of this polished 3-rod single crystal sapphire fiber which has spread out slightly due to the phenyl salicate wax can be seen in Figure 4.7.

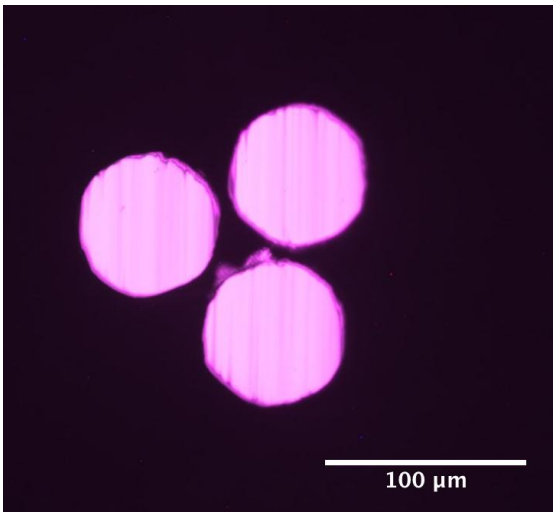

Figure 4.7 3-rod polished single crystal sapphire fiber

The CTS, as previously described in the preliminary work section, has the capability to trace the peaks of the reflection spectrum. Gas sensing as it relates to this experiment uses the component test system's (CTS) (Micron Optics, Inc., Si-720) wavelength sweeping laser was used as the source. This gives a narrow-bandwidth emission from 1520 – 1570 nm that covers the absorption spectra of acetylene at a scanning frequency of 5 Hz. As described in Background Section 2.10 Gas Sensing, the incident light that is transmitted in the air hole region of the fiber

bundle will pick up the absorption spectrum of acetylene due to its direct interaction with the gas molecules.

The optical signals are injected from the CTS into a lead in Corning SMF-28 fiber pigtail that has been cleaved. This fiber was aligned and butt coupled to the 1.5 inch long 3-rod sapphire bundle with each rod having a diameter of 70 µm and both ends polished to a 0.1 µm grit. The lead out fiber consisted of a step index 105/125 µm multimode fiber pigtail connected to a Thorlabs InGaAs photodetector (FGA04). An image of the fiber setup and alignment using the 3D stages can be seen in Figure 4.8.

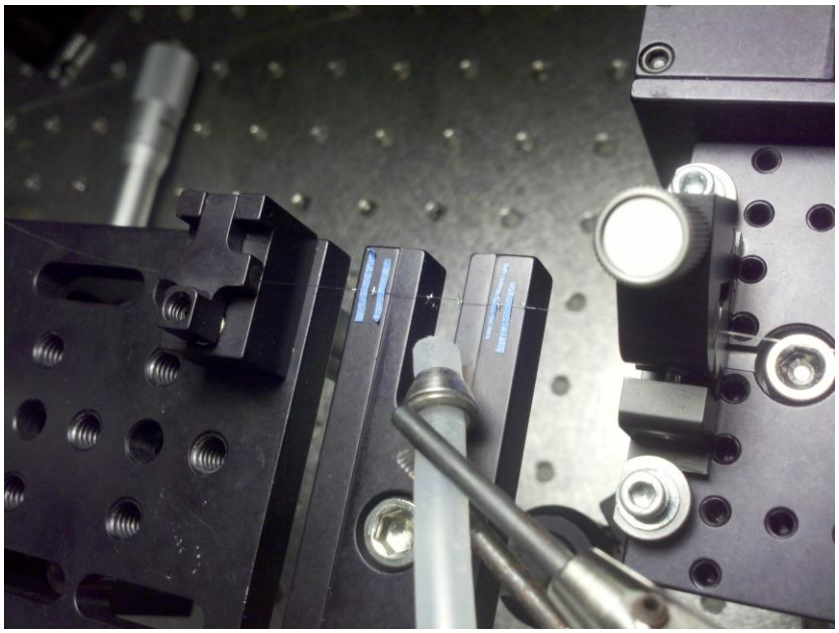

Figure 4.8 Fiber alignment using 3D stages

The photodetector was reverse biased using an Oriel gain amplifier model 70710 set to a gain of 10^7 V/A with a minimum time constant setting. The amplifier was connected to a Lecroy oscilloscope that is triggered to match the CTS emission so that the intensity can be measured as

a function of wavelength. This enables the determination of absorption peaks in the wavelength range that acetylene emits. Acetylene gas is then blown over the 3-rod bundled single crystal sapphire fiber. An overview of the setup can be seen in Figure 4.9 below.

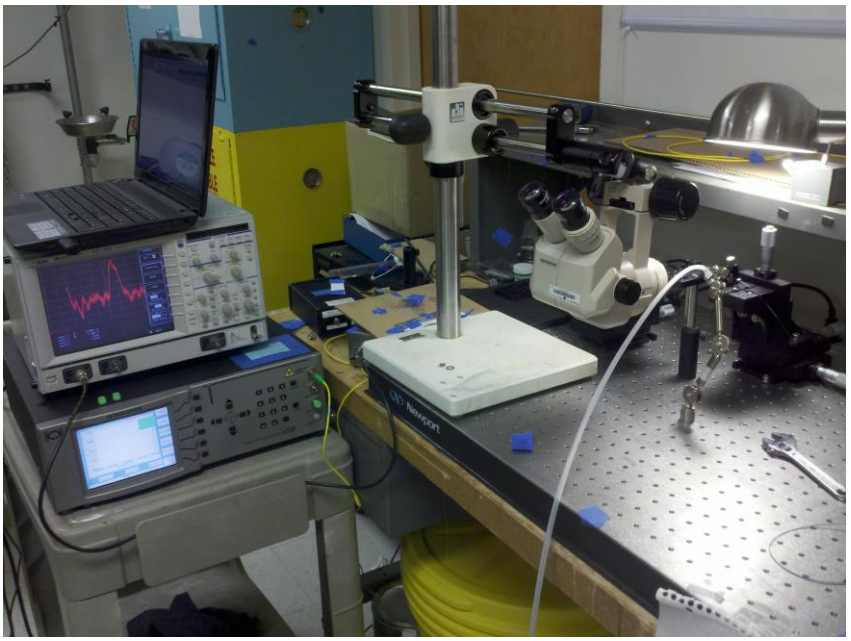

Figure 4.9 Gas sensing setup

Next a 7-rod single crystal sapphire photonic crystal fiber 1.5 inches in length was fabricated for acetylene gas sensing at room temperature. An image of this polished 7-rod single crystal sapphire photonic crystal fiber is seen in Figure 4.10.

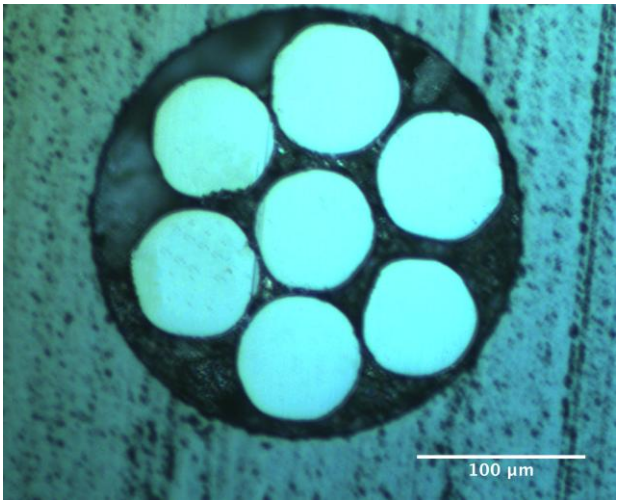

Figure 4.10 7-rod polished single crystal sapphire photonic crystal fiber

Gas sensing using the 7-rod bundled single crystal sapphire fiber also uses the component test system's (CTS) (Micron Optics, Inc., Si-720) wavelength sweeping laser as the source. Again, the optical signals are injected from the CTS into a lead in Corning SMF-28 fiber pigtail that has been cleaved. This fiber was aligned and butt coupled to the 1.5 inch long 7-rod sapphire bundle with each rod having a diameter of 70 µm and both ends polished to a 0.1 µm grit. The lead out fiber consisted of a step index 105/125 µm multimode fiber pigtail connected to a Thorlabs InGaAs photodetector (FGA04). The photodetector was also biased using an Oriel gain amplifier model 70710 set to a gain of 10^7 V/A with a minimum time constant setting. The amplifier was connected to a Lecroy oscilloscope that is triggered to match the CTS emission so that the intensity can be measured as a function of wavelength. Acetylene gas is then blown over the 7-rod bundled single crystal sapphire fiber in a similar fashion as in the 3-rod bundle experiment.

4.2.6 SLED White Light Interferometry

Single crystal sapphire fibers, with a diameter of 70 µm, were separated into 7 pieces and polished with diamond grit paper starting with a 15 µm grit and finishing with a 0.5 µm grit. Six of the sapphire rods were approximately 45 cm in length while one of the sapphire fibers was kept at 50 cm in length. The fibers were cleaned using distilled water and acetone, to remove any residual contaminants from the fibers. The 50 cm long fiber was fusion spliced to a 100/140 µm core/clad graded index silica fiber, which served as the lead in fiber. The fusion splicing process consists of arcing multiple times between a bare 70 µm rod aligned directly next to the 100/140 µm core/clad graded index silica fiber. After a few arcs, the graded index fiber's 100 µm core heats up enough to have the 70 µm single crystal sapphire fiber push into it upwards of 5-10 µm. The 100 µm graded index silica fiber then collapses onto the 70 µm sapphire fiber after more arcing is performed. This guarantees that all of the injected light into the 100/140 µm graded index silica fiber will be transferred to the 70 µm sapphire fiber, instead of traveling in free space due to the size mismatch between the 70 µm sapphire fiber and the 100/140 µm core/clad graded index silica fiber.

The lead in fiber was connected to a miniature spectrometer (Ocean Optics, Inc., USB2000). A diagram of this setup can be seen in Figure 4.11 below.

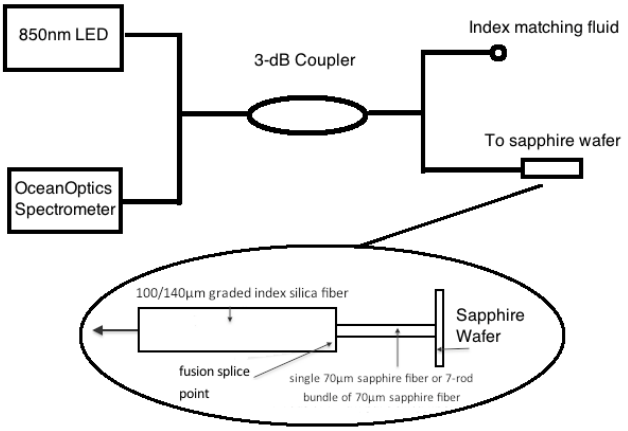

Figure 4.11 White light interferometric setup for both the single rod of single crystal sapphire and the 7-rod bundled single crystal sapphire fiber

A C-plane sapphire wafer 59 µm thick and 1 mm x 1 mm in size was then glued onto a polished borosilicate tube. The tube was then secured to an optical goniometer attached to a 3D stage so that precise angles could be adjusted for the incoming fiber. Light from an 850 nm LED was then launched into the 100/140 µm multimode graded-index silica fiber, which then propagated through the bare sapphire fiber, 50 cm in length, to the sapphire wafer through a 3 dB coupler. A schematic of this process can be seen in Figure 4.11. The bare sapphire fiber was then aligned and brought towards the sapphire wafer until it was within a few microns from touching the wafer. After multiple angular adjustments, the fringe visibility of the single crystal sapphire bare rod was generated using Equation 30 with Matlab. This process was repeated 5 times for repeatability with each run time averaging over 10 minutes. The bare fiber was then tested for optical intensity using a ThorLabs PDA 36A Si switchable gain photodetector set to a gain of 60 dB.

The single rod of sapphire was then surrounded by the 6 rods of bare single crystal sapphire and bundled together using platinum wire. This ensured that the fusion-spliced rod carrying the signal from the white light LED did not change over the course of the experiment. A reflected light optical micrograph of the polished 7-rod sapphire bundled fiber can be seen in Figure 4.12.

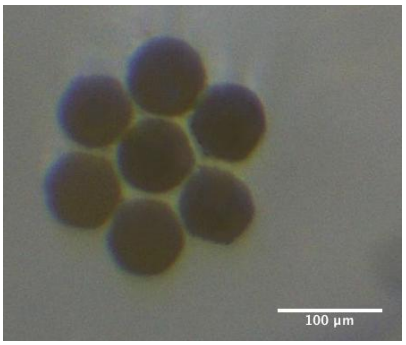

Figure 4.12 7-rod bundled sapphire fiber end face micrograph.

The setup shown in Figure 4.11 was repeated for the 7-rod bundled fiber for the white light interferometry testing. The 7-rod bundled fiber was then aligned and brought towards the sapphire wafer until they were almost touching. Again, multiple angular adjustments were made until the fringe visibility of the 7-rod bundled fiber was generated. This process was repeated 5 times for repeatability with each run time averaging over 10 minutes. The fringe visibility data for both the single rod and the 7-rod bundled fiber was then post-processed in Matlab.

4.2.7 Photodetector Measurements

The 7-rod bundled fiber was then tested for optical loss using a ThorLabs PDA 36A Si switchable gain photodetector set to a gain of 50 dB due to the increased intensity of the fiber bundle. A diagram of this measurement setup can be seen in Figure 4.13 below.

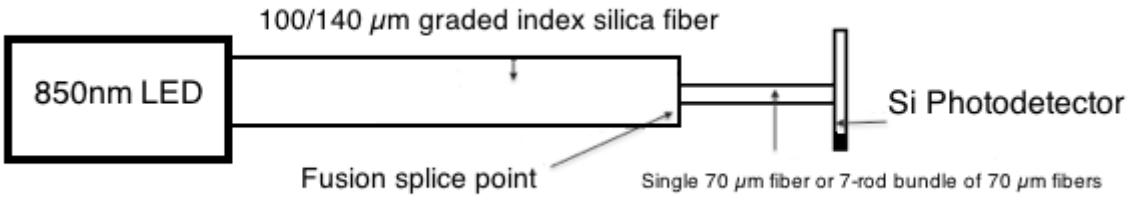

Figure 4.13 Photodetector setup for both the single rod of single crystal sapphire and the 7-rod bundled single crystal sapphire fiber

This data was converted to the 60 dB gain setting using Equation 37:

$$\text{Output [V/W]} = \text{transimpedance gain [V/A]} \times R(\lambda)\ \text{[A/W]} \tag{37}$$

where R (850 nm) is the spectral responsitivity that equals 0.55 A/W as seen in the PDA36A's photodetector specification sheet[77]. The transimpedance gain at 50 dB and 60 dB equals 4.75 x 10^5 V/A and 1.5 x 10^6 V/A respectively. The bundled fiber was then removed from the lead-in 100/140 μm multimode graded-index silica fiber and polished so that the power from the 850 nm LED could be measured. The power data from the photodetector was post processed using Matlab so that the runs for the single rod of sapphire fiber, the 7-rod bundled sapphire fiber, a dark measurement, and the power from the LED to the 100 μm core 140 μm cladding multimode silica fiber could be combined into one graph to show the change in optical output.

4.2.8 Exposure to Harsh Environments

Both the single rod of single crystal sapphire fiber and the 7-rod bundle were exposed to contaminants and put in a furnace to mimic a real world corrosive environment. Alumina particles cause losses in the fiber due to surface scattering. This scattering loss is expected to be more prevalent in the single rod of single crystal sapphire than in the 7-rod bundled fiber due to the protection of the central rod by the outer ring of rods from the contaminants.

Single crystal sapphire fibers, with a diameter of 70 μm, were separated into 7 pieces and polished with diamond grit paper starting with 15 μm grit and finishing with a 0.5 μm grit. Six of the sapphire rods were approximately 45 cm in length while one of the sapphire fibers was kept at 50 cm in length. A bare fiber, 50 cm in length with a 70 μm diameter served as the single rod in this case. The fibers were cleaned using distilled water and acetone, to remove any residual contaminants from the fibers. The 50 cm long fibers was fusion spliced to a 100/140 μm core/clad graded index multimode graded-index silica fiber, which served as the lead in fiber in both cases. The measured splice loss for each fusion splice was approximately 3 dB for each fiber as measured by a Si photodetector. Each fiber was housed in a stainless steel tube cut in half along its length. The lead in fiber was connected to a miniature spectrometer (OceanOptics, Inc., USB2000), which has a central wavelength at 850 nm. The resultant optical intensity was determined using a ThorLabs PDA 36A Si switchable gain photodetector connected to an oscilloscope. Both fibers were optically aligned to provide a maximum photodetector voltage using 3D optical stages.

Both of the fibers were first tested using the setup described above to obtain baseline data. Ten measurements were taken with each recorded data set being the 1000 run time average for repeatable results. Dark measurements and the intensity emitted from the miniature spectrometer were also recorded in the same fashion.

Alumina particles (80/200 mesh) were sieved to produce particle sizes in the 74-125 μm range. Two grams of alumina particles with diameters ranging from 74-125 μm were sprinkled onto each fiber inside of their respective stainless steel tubes. Great care was taken to not allow the alumina particles to contaminate the end face of both fibers. This was done so that the optical intensity changes would be based on the surface scattering along the length of the fibers and not as a result of the end face quality. An image of the contaminated single rod of single crystal sapphire housed inside a stainless steel tube is seen in Figure 4.14.

Figure 4.14 Alumina particle contamination of the single crystal sapphire rod housed inside half of a stainless steel tube

Both fibers were analyzed after the particle contamination using the ThorLabs PDA 36A Si switchable gain photodetector without altering their original optical alignment from the baseline

measurements. The fibers, still housed in their stainless steel tubes, were then placed in a furnace. The horizontal tube furnace temperature was ramped from 27 °C to 1000 °C at a ramp rate of 3.25 °C/min and held at temperature for 1 hour before ramping down to 27 °C at a rate of 1.94 °C/min. A thermocouple was used to check the temperature after the furnace reached 1000 °C. An image of the heat treatment furnace with the respective fibers can be seen in Figure 4.15. The heat treatment is meant to mimic a similar high temperature environment that would be seen in a coal gasifier.

Figure 4.15 Single crystal sapphire rod and the 7-rod bundled single crystal sapphire fiber in their respective stainless steel tube housing in a horizontal tube furnace

Scanning electron microscopy (SEM) was used to examine the fibers after heat treatment with the alumina contaminant particles. The fibers were cleaved and placed onto a stub holder using double-sided adhesive copper tape. The fibers were then sputtered with 10 nm of gold using a sputter coater. An accelerating voltage of 10 kV was used so the surface of the sapphire fiber could be imaged.

5. Results and Discussion

5.1 7-Rod Silica Bundled Fiber

5.1.1 Fabrication

A single bare rod of silica was fabricated and tested and then surrounded by the 6 rods of bare silica fiber and bundled together using platinum wire. This ensured that the fusion-spliced rod carrying the signal from the white light LED would not change over the course of the experiment. A reflected light optical micrograph of the polished bare silica bundled fiber can be seen in Figure 5.1. Small spots of phenyl salicylate wax are visible on the edges of the fibers, which were later removed using acetone. As can be seen in Figure 5.1, the spacing between the central rod and the surrounding rods is larger than the orientation as seen in the FEA structure in Figure 3.19 due to the fact that a platinum tie could not be placed close enough to the end face of the fiber to maintain the bundle spacing as well as not using a consistent fiber diameter for each of the rods. This limits the effective refractive index reduction due to the inability for the rod to be consistently in contact with the outer ring on silica fibers.

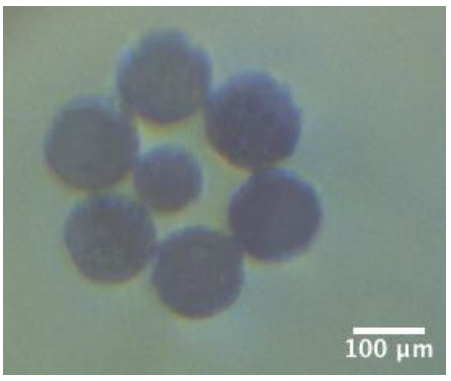

Figure 5.1 7-rod bundled silica fiber end face micrograph

5.1.2 White Light Interferometry

Figure 5.2 shows both data sets with the single rod of silica fiber having an integration time of 43 ms and the 7-rod bundled fiber having an integration time of 15 ms (for viewing purposes). The integration time for the 7-rod bundle of silica is scaled so that it also has the integration time to that of the single rod bundle (at 15 ms) so that the fringe visibility can be calculated using Equation 30. Table 5.1 shows the standard deviation between the both the single rod and the 7-rod bundled fiber.

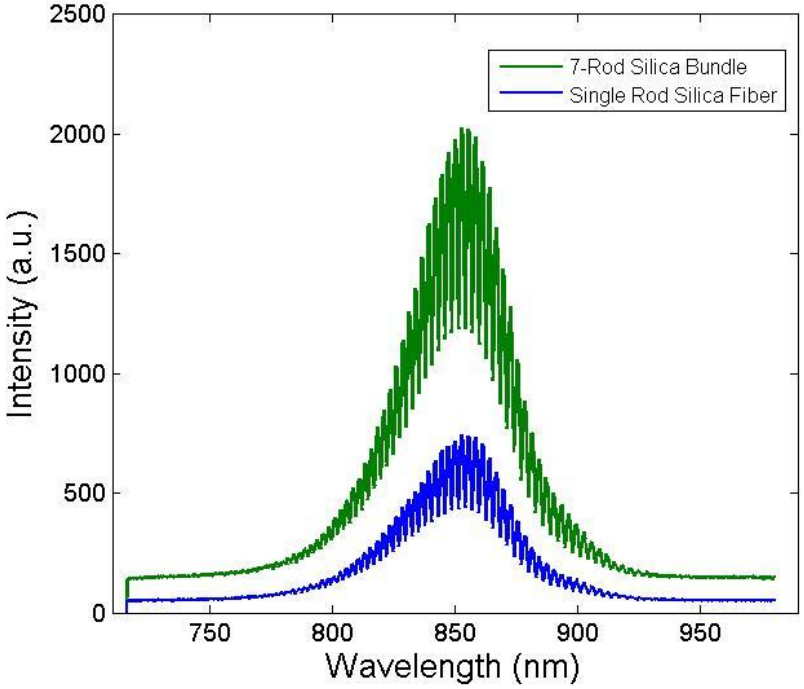

Figure 5.2 White light interferometric response from the single rod of silica fiber and the 7-rod bundled silica fiber

Table 5.1 Fringe visibility difference with the corresponding standard deviation between the both the single rod of silica and the 7-rod bundled silica fiber

	Fringe Visibility (a.u.)	Standard Deviation (μW)
Single Silica Fiber	25.2%	0.0044
7-rod Bundle Silica Fiber	26.4%	0.0076

The fringe visibility results in Figures 5.2 and Table 5.1 show almost no increase in the fringe visibility between the two fibers; meaning that there is not a significant reduction of modes. This is assumed to be due to the inability to maintain the 7-rod structure throughout the length of the z-direction. This agrees with the modeling results in Figure 3.21, which state that if the outer ring of rods is more than 5 μm from the core rod then there will not be a significant reduction in the number of modes. What is interesting about this fiber is the approximately 3x increase in intensity between the both the single rod and the 7-rod bundled fiber. The bundling apparently acts to reflect the higher order modes back into the core rod, which would be lost in the single rod case, thus reducing loss.

5.1.3 Photodetector Measurements

The data from Figure 5.3 shows the 1000 run time averaged photodetector data for the single silica rod, the 7-rod bundled silica fiber, and the LED input all subtracted from the dark measurement. The standard deviation for the single silica rod was 0.0013876, the 7-rod bundled silica fiber was 0.0024129, and the LED input was 0.0051735.

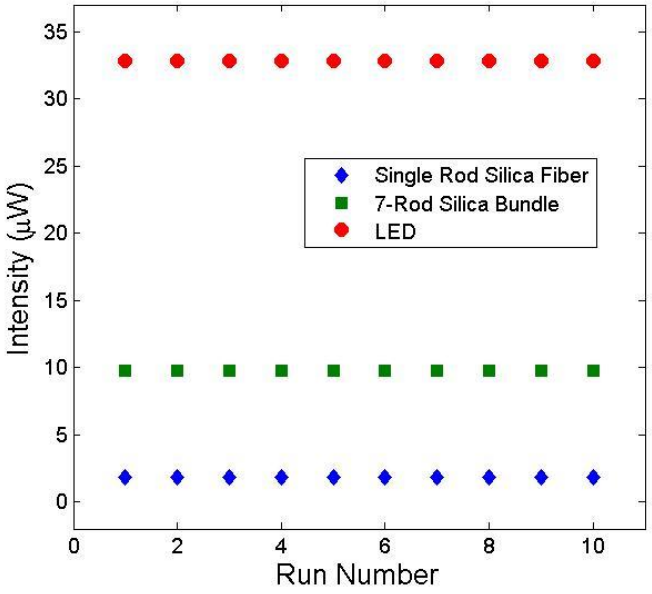

Figure 5.3 1000 run time averaged photodetector data for the single silica rod, the 7-rod bundled silica fiber, and the LED input

The data shows greater than a 5x increase in intensity for the 7-rod bundled fiber versus the single rod fiber, confirming the prior result shown in the fringe visibility tests. This result is expected to be much greater than the fringe visibility due to the fact the photodetector detects the transmitted signal, whereas the fringe visibility shows the reflection spectrum of the signal, leading to higher loss.

Both fibers were then analyzed using a white light interferometry setup as well as a Si photodetector. The results showed that with the current bundling technique, there was a minimal reduction in modes for the 7-rod bundled fiber versus the single rod case but approximately a 3-5x increase in intensity for the 7-rod bundled fiber versus the single rod fiber. This decrease in loss correlates well with the FEA modeling results as shown in Figure 3.20.

5.2 7-Rod Sapphire photonic crystal fiber

5.2.1 Fabrication

Figure 5.4 shows the resultant 7-rod sapphire fiber in the final stages of polishing. The wax and Crystal Bond is fully removed by a series of cleaning steps involving alcohol, distilled water, and acetone to remove any contaminants from the polishing process. This fiber design is the basis for all of the optical characterization in this section.

Figure 5.4 Optical micrograph of a single crystal sapphire bundle during a final polishing stage

5.2.2 Characterization

The polished end-face of one of the fibers produced is shown in Figure 5.5. The micrograph was taken in reflected light to highlight the structural aspects of the fiber.

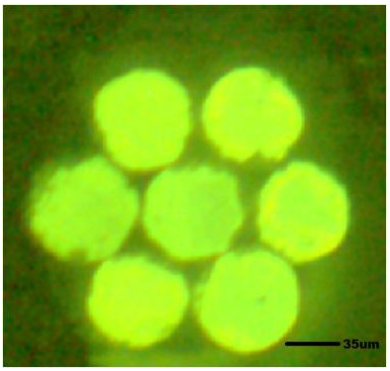

Figure 5.5 Optical micrograph of fiber end-face (reflected light image) with the diameter of the sapphire elements shown as 70 µm

The fibers were grown with the C-axis of the crystal extending along the optical axis of the fiber (along the length of the fiber). The cross-section of the fiber shown is taken perpendicular to the C-axis of each of the fibers. Figure 5.6 shows an optical micrograph of the fiber taken in transmitted light under white light illumination from the transmission side of the fiber.

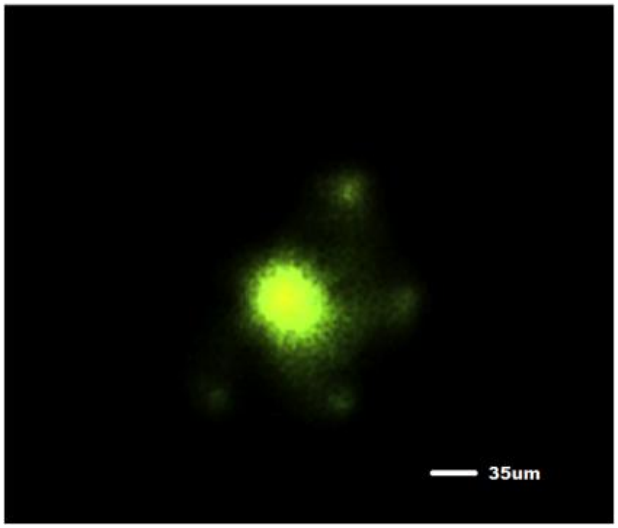

Figure 5.6 Optical micrograph of the photonic crystal sapphire fiber with the diameter of the sapphire elements shown as 70 µm (transmission mode image)

As can be seen in this photo, a significant amount of the light is propagating in the central "core" fiber, which would be consistent with confinement in the core due to the lowering of the average effective refractive index by the holes in the PCF structure. This has been discussed extensively in the literature for silica based PCF's, but we believe this is the first time that this has been demonstrated in a sapphire PCF structure as shown in Pfeiffenberger et al.[68]

The bright region in the center of the micrograph is coincident with the central sapphire rod. Very faint light spots can be seen surrounding the central fiber. These correspond to the center positions of the sapphire rods surrounding the central "core" sapphire rod. The micrograph shown was taken after the sapphire PCF was heated to successively higher temperature up to 1600 °C, demonstrating the extremely high temperature capability of these fibers. Single crystal sapphire in general is known to have excellent high temperature performance and excellent corrosion resistance, both of which were expected to be inherited by the sapphire PCF's.

5.2.3 Numerical Aperture

Multiple dark measurements were first calculated to determine the testing offset, which was determined to be from -0.167 V for the single rod case and -0.168 V for the 7-rod bundled fiber. Results were recorded for the single rod of sapphire and the 7-rod bundled sapphire fiber with a distance of 2.5 inches from the fiber end face to the photodetector at a zero degree angle with the respective dark offset taken into account. The photodetector was then adjusted at specific angles with the pivot point directly underneath the fiber end face so that the output angle could be changed for various photodetector locations. The angle was first adjusted in the positive direction until the 5% optical intensity ($\theta_{5\%}$) measurement was recorded and then measurements

were taken in the negative direction. As in Equation 34, the negative and positive 5% optical intensity angle readings were averaged and the sine of this angle (as in Equation 31) allowed for the computation of NA_{eff}. As seen in Appendix C, the bundled fiber had an average effective $NA_{eff} = 0.3222$ while the single rod had an average effective $NA_{eff} = 0.3436$ over 3 runs each. Appendix C shows the tables for the detailed numerical aperture calculation for the single sapphire fiber and 7-rod bundle respectively.

Figure 5.7 shows the fiber collimator coupling light from the 632 HeNe laser through a 105/125 µm core/clad step index MMF which is aligned and butt coupled to the sapphire bundle using a fiber holder. Figure 5.8 shows the setup for the single rod of sapphire fiber. This fiber had significantly less voltage output collected by the photodetector, which aligns with other results about the increased intensity for the 7-rod bundled fiber as seen in later sections.

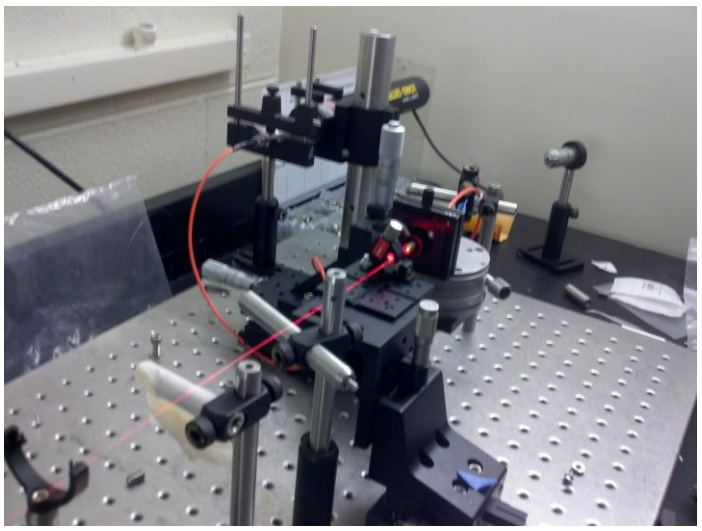

Figure 5.7 Fiber collimator coupling light from the 5 mW 632.8 nm HeNe laser through a 105 µm core step index MMF

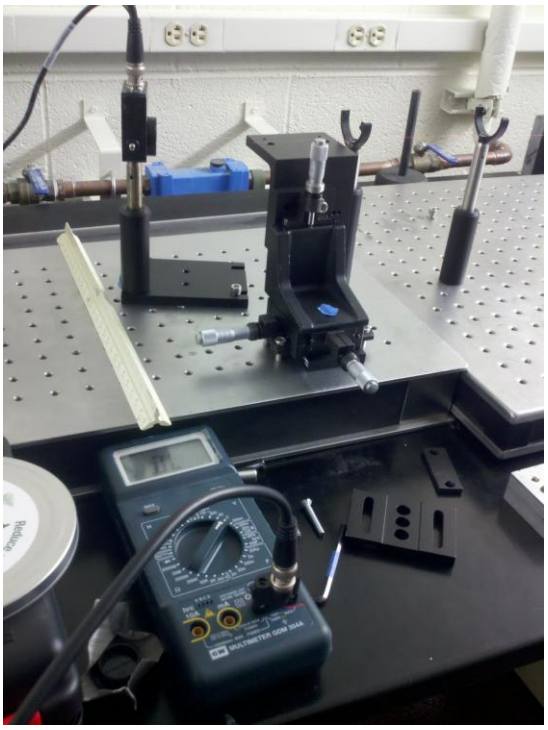

Figure 5.8 Setup for the PDA36A photodetector for the single rod of sapphire

Numerical aperture experiments have been completed using both a single 70 µm diameter rod of single crystal sapphire fiber and a 7-rod bundle (with each rod in the bundle being 70 µm in diameter) of single crystal sapphire. The 7-rod bundled fiber had an average effective NA of 0.3222 while the single rod had an average effective NA of 0.3436. Three runs for each fiber demonstrated the repeatability of the data for each fiber. This decrease in effective numerical aperture equates to a 12.068% decrease in the number of modes for the 7-rod bundled fiber case. The effective numerical aperture tests also show the increased intensity between the 7-rod bundled fiber versus the single rod of single crystal sapphire fiber, which shows an intensity increase is approximately 3x.

5.2.4 Far Field Patterns

At 632.8nm the far-field pattern for a SMF-28 and single sapphire rod has been examined as seen in Figures 5.9 and 5.10 respectively for comparison purposes. The 7-rod bundle of single crystal sapphire should have fewer modes than the single rod of single crystal sapphire due to the cladding layers average effective refractive index being slightly less than the refractive index of the core rod. Under the same setup conditions, the far field pattern in Figure 5.11 shows the 7-rod bundle of single crystal sapphire's intensity. The intensity is especially prevalent in the center of the image as compared to that of the single rod of sapphire in Figure 5.10.

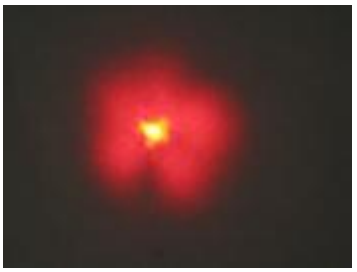

Figure 5.9 Far-field pattern for a meter length Corning SMF28 fiber

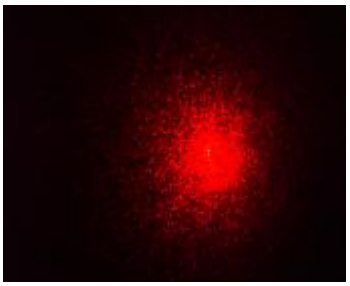

Figure 5.10 Far-field pattern for a single meter length rod of single crystal sapphire

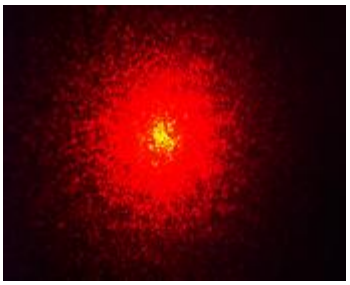

Figure 5.11 Far-field pattern for the 7-rod single crystal sapphire bundled fiber one meter in length

The far field patterns for both a single rod of single crystal sapphire and a 7-rod bundle of single crystal sapphire have been demonstrated. Both the single rod of single crystal sapphire and the 7-rod bundle of single crystal sapphire were tested under the same conditions so the results could be directly compared.

The far field pattern of the 7-rod bundle in Figure 5.11 has what appears to be a greater intensity as shown by the bright yellow spot in the center of the pattern as compared to the single rod case seen in Figure 5.10. This is determined to be a result of the fact that the outer rods of the 7-rod bundle are more able to couple the higher order modes, which would otherwise be lost as in a bare single rod. This enables a lower loss fiber that can maintain a higher intensity throughout the length of a fiber.

5.2.5 Gas sensing

The 3-rod sapphire fiber bundle's response spectrum with the acetylene gas turned on and off from the photodetector was post processed using Matlab and can be viewed in Figure 5.12. Each data point is the average of 150 spectrums collected.

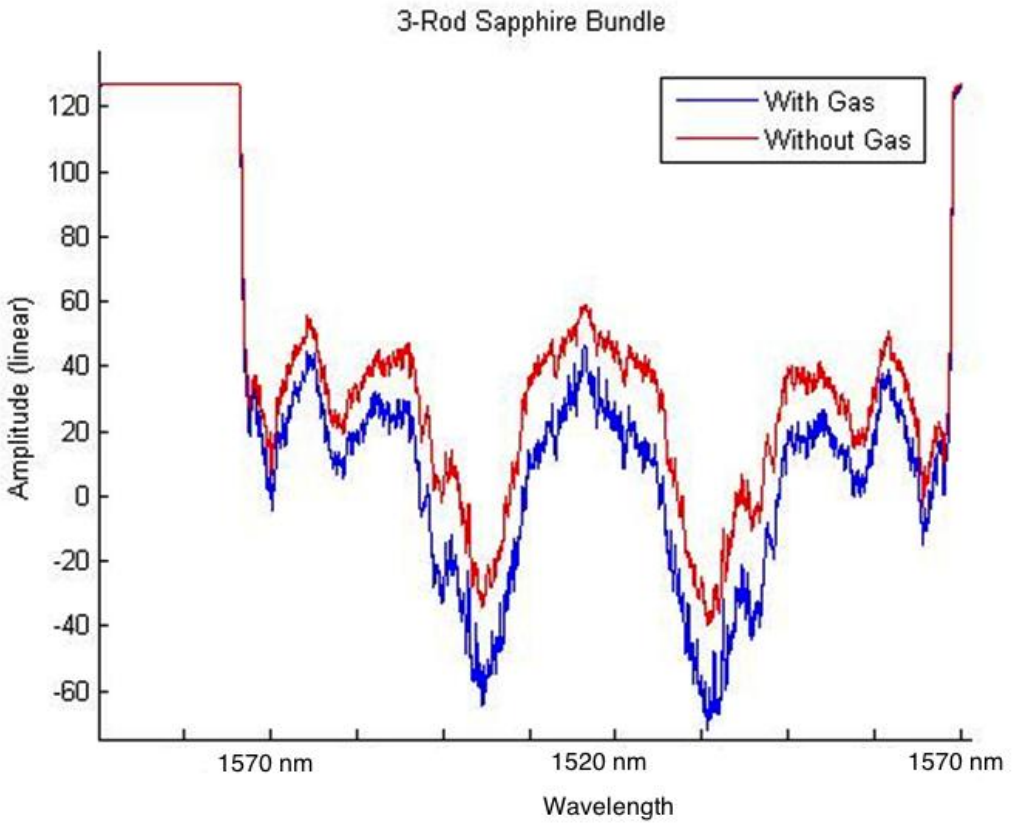

Figure 5.12 Response spectra for the baseline signal and the 3-rod single crystal sapphire fiber

The acetylene peaks are visible from the data point range of 1.5 to the 4.5 region but can be more visibly seen when compared to a reference cell. The x-axis in all of the Matlab figures in this section corresponds to the sweep of the CTS. To the left of 1570 nm is what is known as the dead zone, where the CTS is calculating the data for each sweep. The wavelengths 1570 nm to 1520 nm (left to right) corresponds to the sweep up of the CTS. To the right of the 1520 nm point, the spectrum is the mirror image of the wavelength range from 1570 nm to 1520 nm and represents the sweep back to the CTS. The dead zone then begins again to the right of 1570 nm (at right).

The 3-rod bundled fiber was tested against the same setup with the bundled fiber removed leaving the absorption peaks to propagate in free space between the lead-in and lead-out fibers with a separation distance of 1.5 inches. The response spectra for the free space baseline signal and the signal with the acetylene on can be seen in Figure 5.13 below.

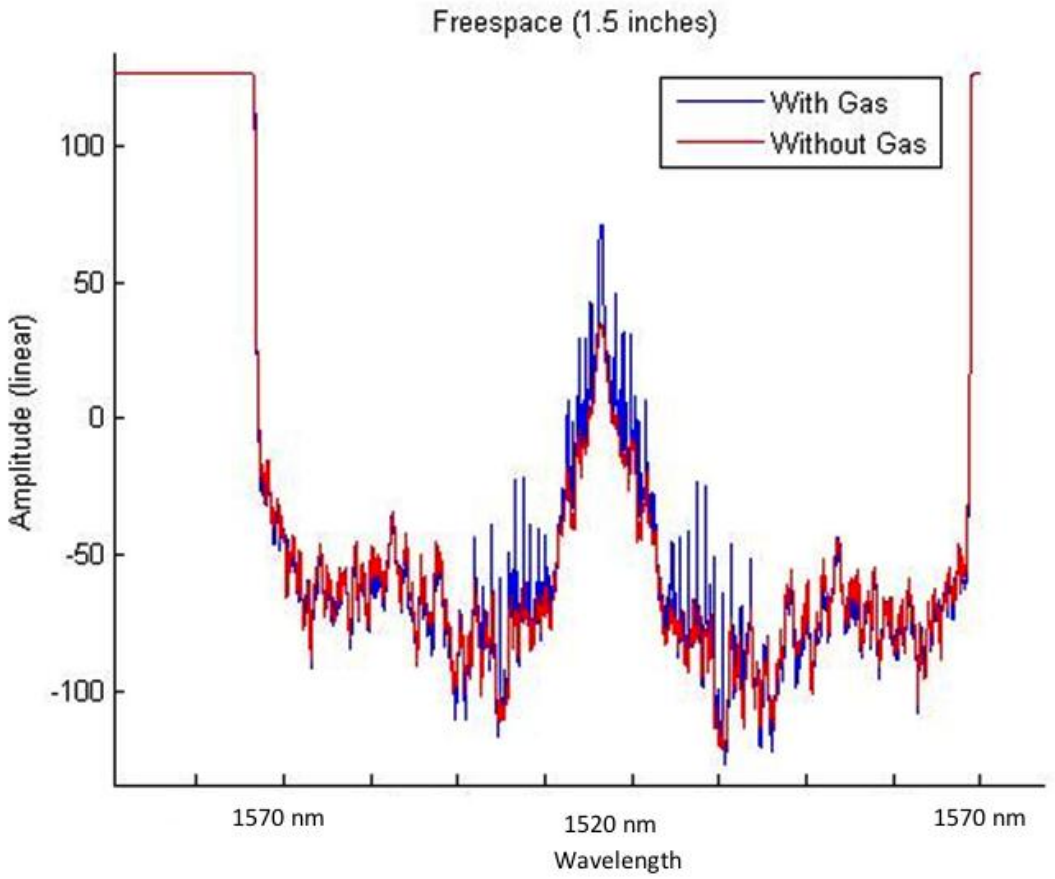

Figure 5.13 Response spectra for the free space baseline signal with the acetylene turned on

Figure 5.13 clearly shows the acetylene gas peaks for the free space reference cell. This shows the signal intensity is stronger for the reference cell than in the 3-rod bundle. This is thought to be due to the fact that the 3-rod bundle cannot maintain a perfect hole structure that the input light is guided into, giving rise to coupling and absorption loss as well at scattering losses. The

normalized difference between the 3-rod bundle and the reference cell in free space has been plotted in Figure 5.14. The normalized division between the 3-rod bundle and the reference cell in free space has been plotted in Figure 5.15.

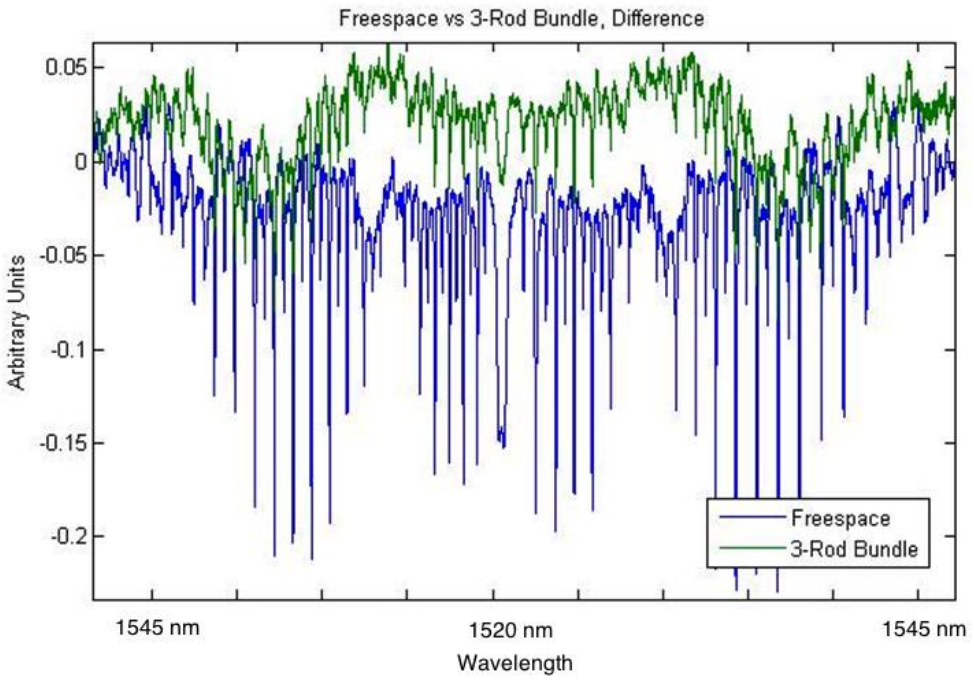

Figure 5.14 Normalized difference between the free space reference cell and the 3-rod bundle of single crystal sapphire fiber with the acetylene turned on

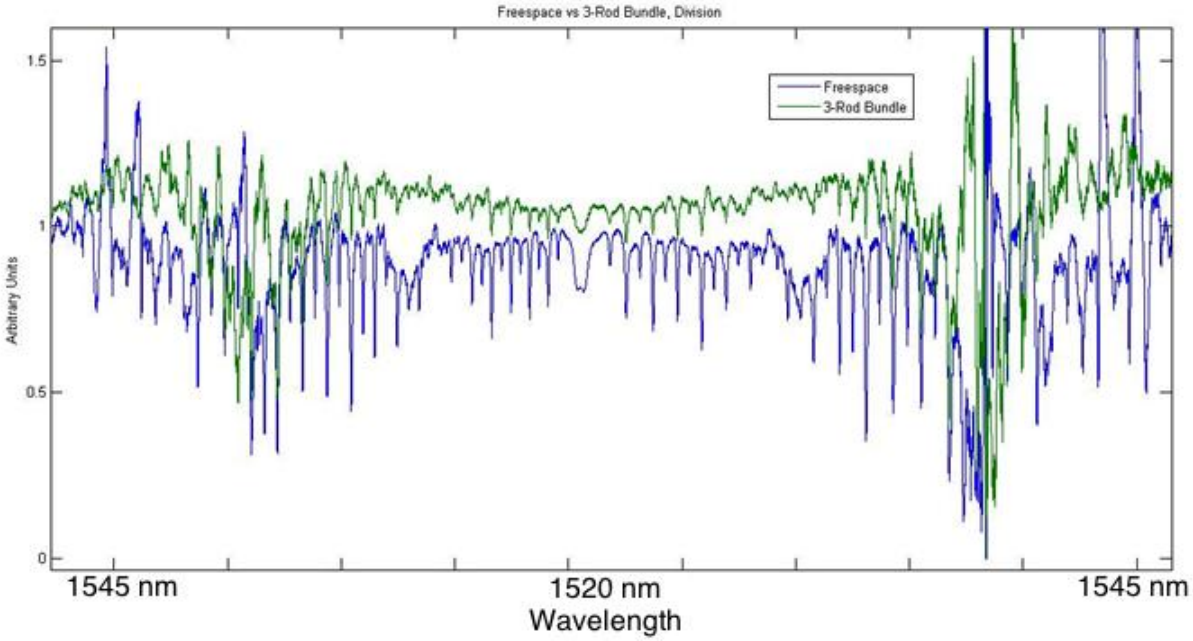

Figure 5.15 Normalized division between the free space reference cell and the 3-rod bundle of single crystal sapphire fiber with the acetylene turned on

Figure 5.14 and 5.15 clearly show that the absorption peaks from the acetylene gas in the reference cell directly line up to the 3-rod bundle case. These figures confirm the detection of acetylene at room temperature using a 3-rod bundle of single crystal sapphire.

The 1.5 inch long 7-rod sapphire fiber bundle's response spectrum with the acetylene gas turned on and off was post processed using Matlab and can be viewed in Figure 5.16. Each data point is the average of 150 spectrums collected.

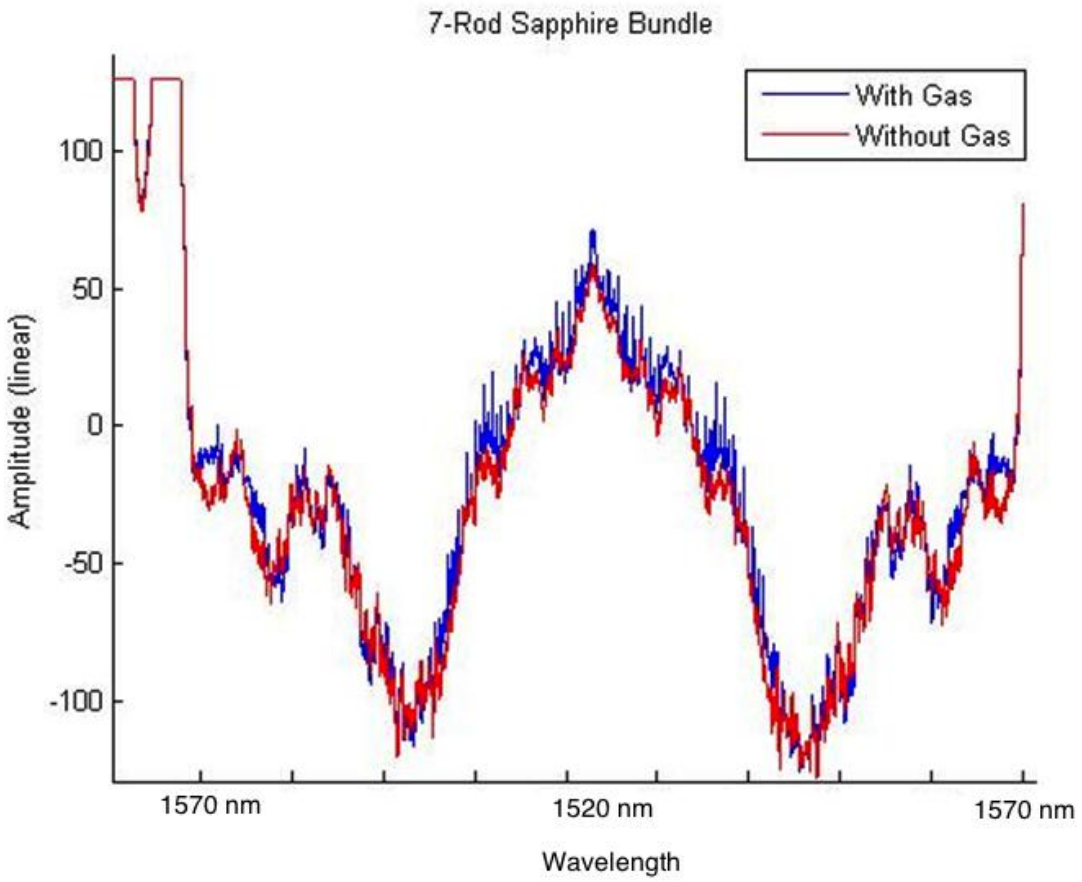

Figure 5.16 Response spectra for the baseline signal and the 7-rod single crystal sapphire fiber

The acetylene peaks are visible from the data point range of 1.5 to the 4.5 region but can be more visibly seen when compared to the same reference cell seen in Figure 5.13.

As in the 3-rod bundle case, the 7-rod bundle of single crystal sapphire cannot maintain a perfect hole structure that the input light is guided into, effectively scattering some of the signal. The 7-rod bundled fiber is much more difficult to align compared to that of the 3-rod bundle. This is due to the fact that the air holes on the lead-in side of the fiber do not always correlate to the same position on the lead-out side of the fiber due to imperfections in the bundling technique.

The normalized difference between the 7-rod bundle and the reference cell in free space has been plotted in Figure 5.17. The normalized division between the 7-rod bundle and the reference cell in free space has been plotted in Figure 5.18.

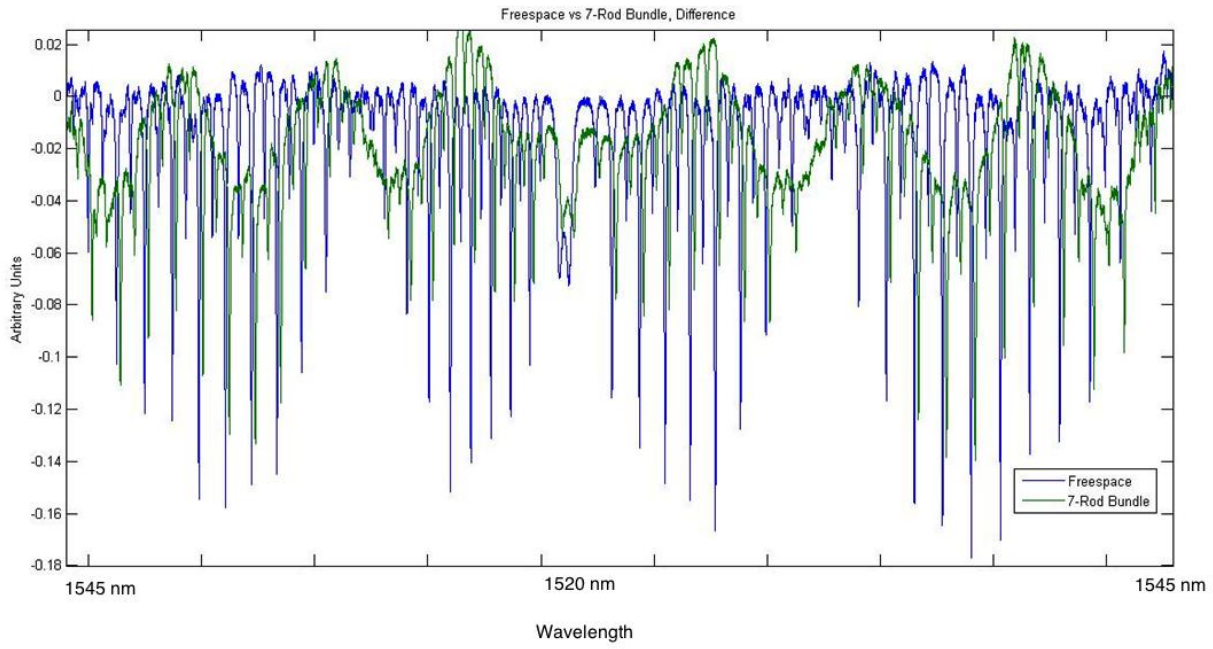

Figure 5.17 Normalized difference between the free space reference cell and the 7-rod bundle of single crystal sapphire fiber with the acetylene turned on

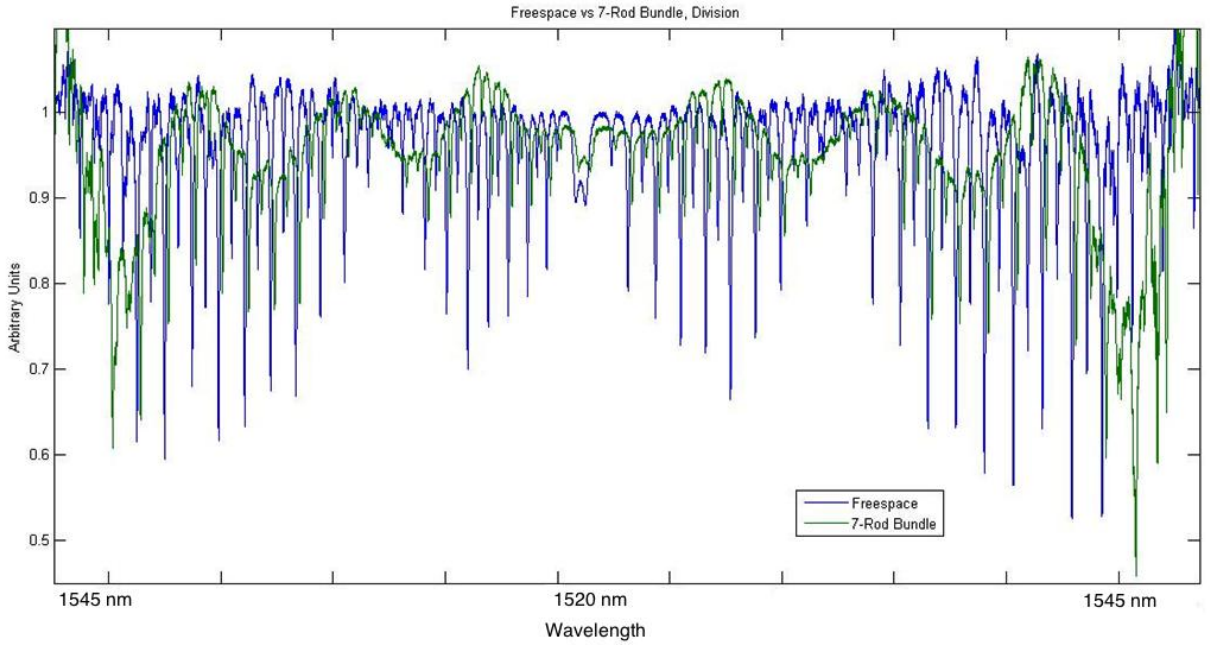

Figure 5.18 Normalized division between the free space reference cell and the 7-rod bundle of single crystal sapphire fiber with the acetylene turned on

This is the first time that a gas sensor has been fabricated using 7-rod single crystal sapphire photonic crystal fiber as well as in the 3-rod bundle structure. Much work still needs to be done on the fabrication and optimization for this fibers light-guiding ability in the air region between the fiber rods. A potential way to increase the transmission strength of this gas sensor would be to fuse the bundled sapphire rods together. This would minimize the amount of scattering due to imperfections in the bundling process. This would also allow for longer lengths of fibers to be used as a gas sensor which would help to increase the absorption peak signal strength due to a longer interaction time. Future applications of this fiber consist of higher temperature gas sensing with other gases that are present in a coal gasification system including CO, CO_2, and CH_4.

5.2.6 SLED White Light Interferometry

Figure 5.19 shows both data sets fit to one another with both the single rod of sapphire fiber and the 7-rod bundled fiber having an integration time of 80 ms. Table 5.2 shows the standard deviation between the both the single rod and the 7-rod bundled fiber.

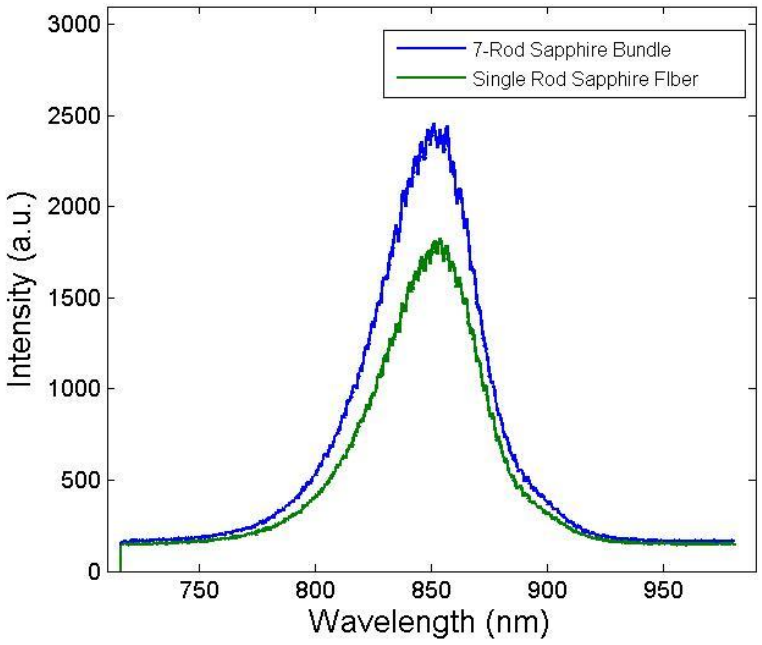

Figure 5.19 White light interferometric response from the single rod of sapphire fiber and the 7-rod bundled sapphire fiber

Table 5.2 Fringe visibility difference with the corresponding standard deviation between the both the single rod of sapphire and the 7-rod bundled sapphire fiber

	Fringe Visibility (a.u.)	Standard Deviation (μW)
Single Sapphire Fiber	2.11%	0.0027
7-rod Bundle Sapphire Fiber	2.38%	0.0098

The fringe visibility results in Figure 5.19 and Table 5.2 show that the alignment has not been optimized. The alignment is especially difficult in the 7-rod bundle where slight differences in the end face angle can have a major effect on the fringe visibility. Another challenge that must be overcome is the inability to perfectly maintain the 7-rod hexagonal structure throughout the length of the z-direction during the bundle fabrication. As in the previous experiment using a bare silica rod and a 7-rod silica bundle, there is approximately a 1.4x increase in intensity between the both the single rod and the 7-rod bundled fiber.

5.2.7 Photodetector Measurements

The data from Figure 5.20 shows the 1000 run time averaged photodetector data for the single crystal sapphire rod, the 7-rod bundled single crystal sapphire fiber, and the LED input all subtracted from the dark measurement. The standard deviation for the single crystal sapphire rod was 0.0026738, the 7-rod bundled single crystal sapphire fiber was 0.0098173, and the LED input was 0.0127617. The data shows approximately a 1.6x increase in intensity for the 7-rod

bundled fiber versus the single rod fiber, which agrees well with the prior results using a bare silica rod and a 7-rod silica bundled fiber.

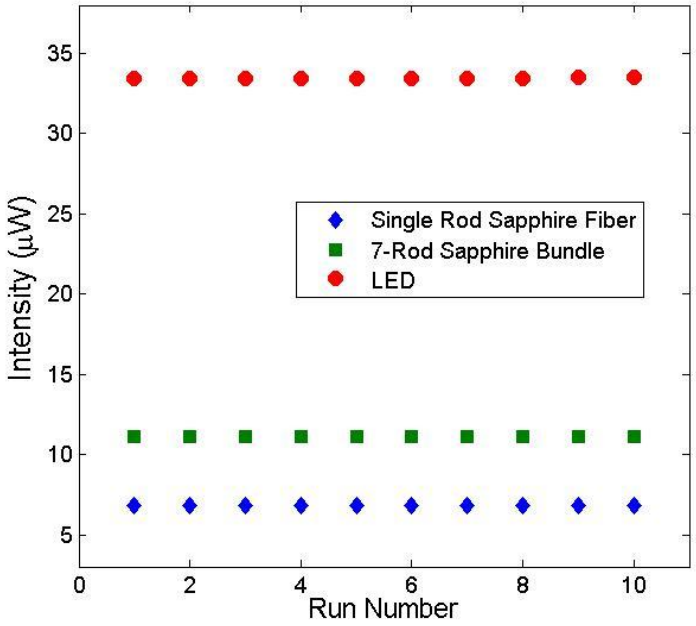

Figure 5.20 1000 run time averaged photodetector data for the single crystal sapphire rod, the 7-rod bundled single crystal sapphire fiber, the dark measurement, and the LED input

This result is expected to be greater than the fringe visibility due to the fact the photodetector detects the transmitted signal, whereas the fringe visibility shows the reflection spectrum of the signal, leading to higher loss. The difference between the sapphire data and the silica data shows that the strong confinement of modes to the core plays a key role in the sapphire bundle. In a silica bundle, higher order modes more easily escape from the core but are coupled into the outer rods limiting loss. In a sapphire bundle, the confinement of modes to the core rod due to the large refractive index difference between sapphire and air is much more prevalent. The higher order modes that escape the core are coupled into the outer sapphire fibers, but due to the high core confinement, not as many modes will propagate into the ring of cladding as compared with the silica bundle as seen in Section 5.1.3.

Fringe visibility and photodetector measurements were used to examine both a single rod of sapphire with a core diameter of 70 μm and also a 7-rod sapphire fiber with diameters of 70 μm, all made of single crystal sapphire fiber. Both fibers were then analyzed using a white light interferometry setup as well as a Si photodetector. The results showed that with the current bundling technique, there was a minimal reduction in modes for the 7-rod bundled fiber versus the single rod case but approximately a 1.4 -1.6x increase in intensity for the 7-rod bundled fiber versus the single rod fiber. This result directly relates to the silica FEA modeling results as well as the fringe visibility and photodetector results by showing an increase in intensity for the bundled fibers without a significant reduction in modes as compared to the single rod cases. The silica and sapphire fibers can be directly compared to each other because the same central rod is used in both cases: the central rod that made up the single rod cases was the rod that was bundled around, creating the 7-rod bundle.

5.2.8 Exposure to Harsh Environments

The baseline data for the single rod, the 7-rod bundle and the input LED can be seen in Figure 5.21.

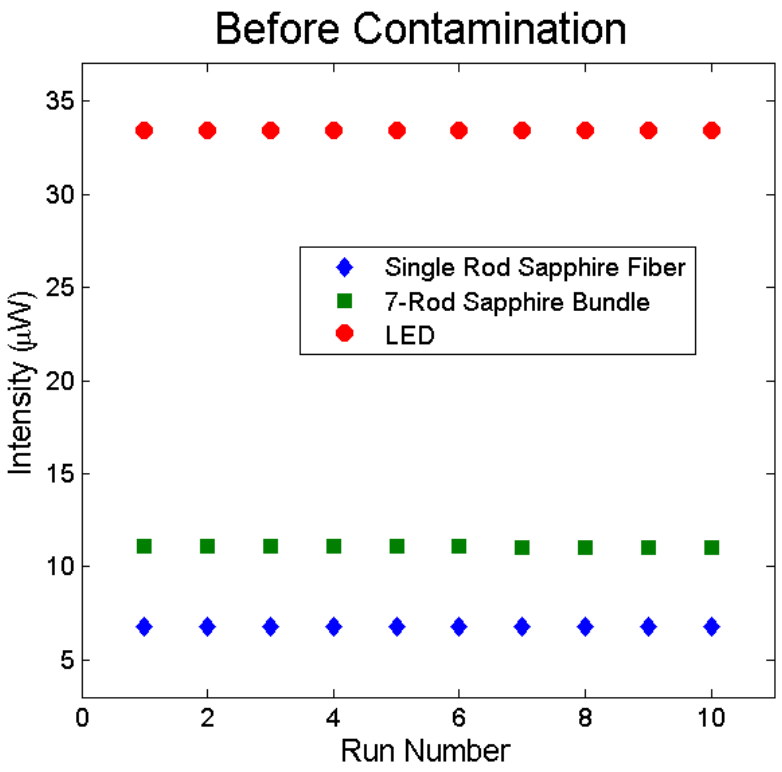

Figure 5.21 Baseline results of the 1000 run time averaged photodetector data for the single crystal sapphire rod, the 7-rod bundled single crystal sapphire fiber, the dark measurement, and the LED input

Photodetector measurements were taken after the heat treatment. Table 5.3 below shows the 1000 run time averaged photodetector data for the single crystal sapphire rod and the 7-rod bundled single crystal sapphire fiber before and after their heat treatment with the alumina contaminant.

Table 5.3 1000 run time averaged photodetector data and standard deviation for the single crystal sapphire rod and the 7-rod bundled single crystal sapphire fiber after contamination with 2 grams of alumina particles, before and after heat treatment at 1000 °C.

	Before Contamination		After Contamination		After 1000 °C	
	Avg. Intensity (µW)	Std. Deviation	Avg. Intensity (µW)	Std. Deviation	Avg. Intensity (µW)	Std. Deviation
Single Rod	6.782405626	0.000494908	5.43122266	0.003382562	5.929886736	0.002432046
7-Rod Bundle	11.07258354	0.019173502	10.79825571	0.023128144	10.90677377	0.004295811

The single rod case shows a before contamination to after contamination percent reduction of 24.8%, a before contamination to after 1000 °C percent reduction of 14.3%, and an after contamination to after 1000 °C percent increase of 8.4%. The 7-rod bundle shows a before contamination to after contamination percent reduction of 2.5%, a before contamination to after 1000 °C percent reduction of 1.5%, and an after contamination to after 1000 °C percent increase of 1.0%.

The 7-rod bundled fiber was able to better protect the core from these contaminants and allow the core to maintain a contaminant free interface. Contaminants on the outside of the core act as scattering sites due to their particle size being larger than the wavelength of light being transmitted which is why the data shows a reduction in the optical signal for the 7-rod bundled fiber after contamination. It is important to note that the bundled fibers intensity after contamination is still greater than that of the single rods intensity before contamination. This result aligns well with the loss reduction seen in other experiments in this thesis. This intuitively makes sense due to the fact that the majority of the signal is carried in the central rod of the bundle. In the 7-rod bundled fiber, the modes that travel into the outer ring of rods will still have scattering due to the contaminants which is why the small decrease in signal intensity can be seen.

Any alumina particles that were present during the heat treatment and photodetector runs did not survive the gold sputtering as can be seen in Figures 5.22 and 5.23. The splotches seen on the

fiber are assumed to be some of the smaller size alumina particles that made it through the sieving process. The heat treatment with the alumina particle contaminant was only held at 1000 °C for 1 hour, which is not long enough for the larger particles to sinter onto the surface of the structure.

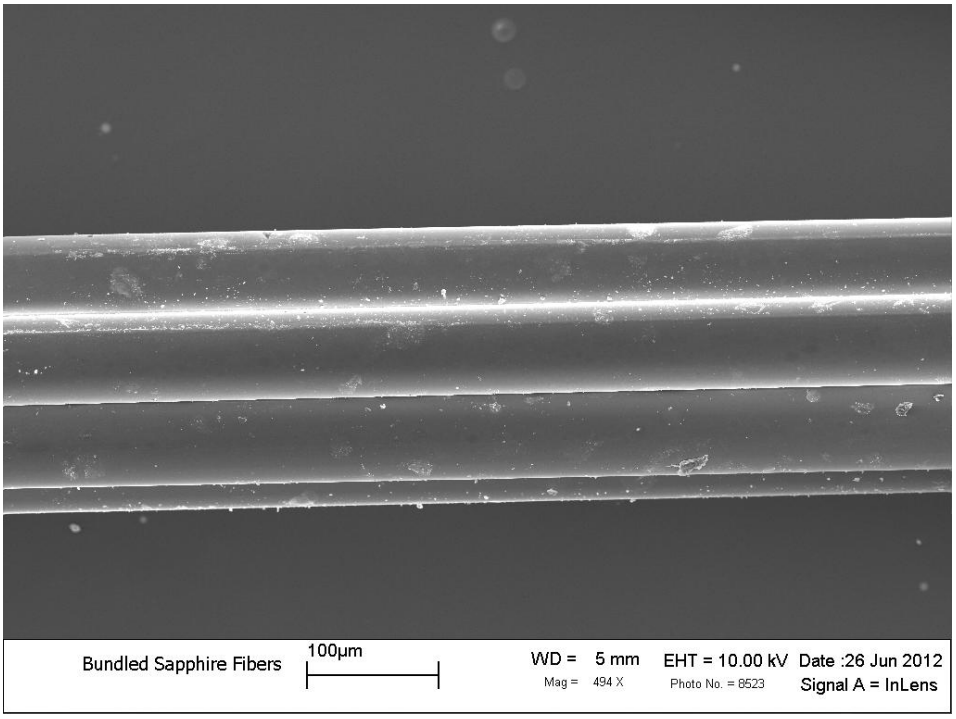

Figure 5.22 SEM micrograph of the side of the 7-rod bundled single crystal sapphire fiber after heat treatment with 2 grams of alumina particle contaminant

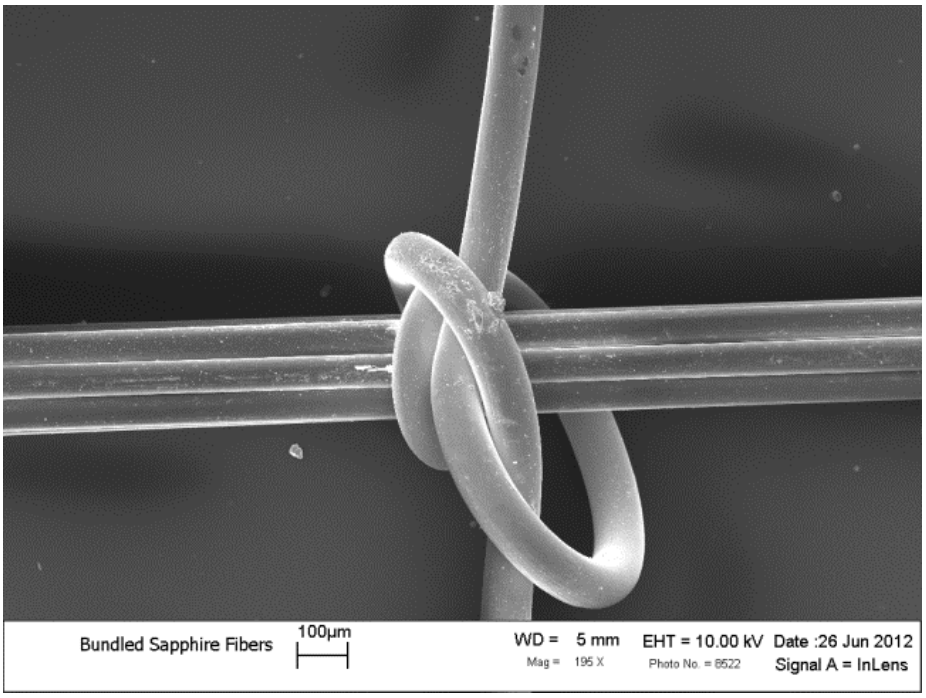

Figure 5.23 SEM micrograph of the side of the 7-rod bundled single crystal sapphire fiber at a Pt tie after heat treatment with 2 grams of alumina particle contaminant

This experiment helps to show the real world benefits that this fiber offers to shield against scattering defects due to the majority of the signal residing in the central rod of the bundle. This helps to limit contamination to the surface of the core rod, allowing for a transmitted signal with greater intensity and less loss.

6. Conclusions

Fabrication of the first photonic crystal sapphire fiber has been accomplished and modeled using Comsol Multiphysics and MIT Photonic Bands software. Although the fiber design that is mainly considered in this study (the 7-rod structure consisting of 70 µm diameter single crystal sapphire rods arranged in a hexagonal structure) does not contain either a TE or TM polarized band gap, the fiber still produces useful properties. These include lower loss compared to that of

a bare single rod of single crystal sapphire, protection from materials adsorbing onto the central core rod during contamination, potential use as a temperature sensor, and as a gas sensor.

The Comsol Multiphysics modeling work laid the foundation for understanding how these bundled fibers propagate light. Much work has gone into the modeling of this fiber to determine the optimum structure that can still be readily fabricated using current commercially available fibers. As for the photonic bandgap modeling, it has been shown that if a sapphire fiber structure with the correct dimensions and spacing's can be fabricated, then a photonic bandgap fiber made of single crystal sapphire in air is feasible. This work is very important to the eventual photonic band gap fabrication as it examines the optimal size and spacing's required to fine tune a bandgap in a wide range of frequencies.

The optical characterization of the 7-rod bundled fiber demonstrates its wide range of end uses. The effective numerical aperture tests also show the increased intensity between the 7-rod bundled fiber versus the single rod of single crystal sapphire fiber, which shows an intensity increase is approximately 3x. This also aligns with the fringe visibility and photodetector data taken from the 50 cm long 7-rod bundled fiber and single rod of sapphire which also show an approximately 1.5x increase in intensity. The white light interferometry demonstrates how this fiber could be used as a harsh environment high temperature sensor operating by reflection interferometry. The gas sensing experiments performed show the feasibility for this type of bundled sapphire fiber for its use in a gas sensing. Although this fiber has only demonstrated gas sensing at room temperature, its ability to sense gas should not be limited by higher temperatures.

7. Unique Accomplishments

Many unique contributions to literature have come from the work on random hole optical fiber modeling, solid core photonic band gap fiber modeling, silica bundled fiber modeling and fabrication, and single crystal sapphire photonic crystal fiber modeling and fabrication. These contributions include:

- The first to use FEA modeling for a random hole optical fiber
- The first to use FEA modeling for a solid core photonic band gap fiber
- Modeling of the first 7-rod bundled silica fiber
- Modeling of the first sapphire photonic crystal fiber structure
- Fabrication of the first sapphire photonic crystal fiber structure
- Fabrication of the first 7-rod bundled silica fiber
- Design optimization of sapphire photonic crystal fiber structures
- Design optimization of the first sapphire photonic band gap fiber
- The first to use a single crystal sapphire photonic crystal fiber as a gas sensor

8. Future Work

Using single crystal sapphire for high temperature gas sensing is a new technology and much work still needs to be done. Directly relating to this thesis, a better way to maintain a consistent hexagonal structure along the length of the bundles will aid in the reduction of modes. As seen in the previous section dealing with spacing the silica rods from the core, it is essential for the outer ring of rods to be in direct contact with the central core rod for the highest reduction in the

number of modes. From a fabrication standpoint, the ability to produce a fiber diameter less than 50 μm would significantly reduce the number of modes due to the core size's direct relationship with the number of modes it can carry. The only problem with smaller core rods would be a greater difficulty to fusion spice the fiber to a lead in or lead out fiber.

In terms of sapphire fiber modeling, much work could be done around finding what distance from the core rod the outer ring of fibers (in a 7-rod bundle) needs to be within for a significant reduction of modes. In terms of finding a photonic band gap in sapphire, the ability to be able to purchase fibers and tubes of single crystal sapphire with much smaller core diameters and wall thicknesses respectively, will allow for possible photonic band gaps in the telecommunications and IR wavelength ranges. The idea of stacking tubes of single crystal sapphire to create the first photonic bandgap fiber, similar to the structures described in Section 3.7 MIT Photonic Bands Modeling, could be a possibility if the tube sizes available for purchase can be scaled to have much smaller sizes with a very thin wall thickness. Depending on the scale size of these tubes, band gaps could open up different frequency ranges and create very useful high temperature gas sensors if these designs could be successfully fabricated.

References

[1] G. Keiser, *Optical Fiber Communication*, McGraw-Hill Inc.: New York (1991).

[2] E. Udd, Fiber optic smart structure technology, in *Fiber Optic Smart Structures*, E. Udd, ed.; John Wiley & Sons, Inc.: New York (1995) 5-21.

[3] D. H. Jundt, M. M. Fejer, and R. L. Byer, Characterization of single-crystal sapphire fibers for optical power delivery systems, *Appl. Phys. Lett.* 55 (1989) 2170-2172.

[4] http://www.sciner.com/Opticsland/FS.htm

[5] K. A. Murphy, B. R. Fogg, G. Z. Wang, A. M. Vengsarkar, and R. O. Claus, Sapphire fiber interferometer for microdisplacement measurements at high temperatures, *SPIE-Int. Soc. Opt. Eng. Proc. of Spie — the Int. Soc. for Opt. Eng.* 1588 (1991) 117-124.

[6] Keiser, G. 1991. Optical Fiber Communications. McGraw-Hill, New York.

[7] Handbook of Optical Materials, Ed. Marvin Weber, Laser and Optical Science and Technology (CRC Press, 2002)

[8] global.kyocera.com/prdct/fc/product/pdf/s_c_sapphire.pdf Fig. 5 Transmission vs. Wavelength p.4.

[9] Nubling R. K. and J. A. Harrington. 1997. Optical properties of single-crystal sapphire fibers. *Appl. Opt.* 36:5934-5940.

[10] Innocenzi, M. E and R. T. Swimm, 1990. Room-temperature optical absorption in undoped α-Al_2O_3. J. Appl. Phys. 67:7542-7546.

[11] D. H. Jundt, M. M. Fejer, and R. L. Byer, "Characterization of single-crystal sapphire fibers for optical power delivery systems," Appl. Phys. Lett. 55, 2170–2172 (1989).

[12] R. S. Feigelson, "Pulling optical fibers," J. Cryst. Growth 79, 669–680 (1986).

[13] R. S. F. Chang, S. Sengupta, G. J. Dixon, L. B. Shaw, and N. Djeu, "Growth of small laser crystals for study of energy kinetics and spectroscopy," in *Growth, Characterization, and Applications of Laser Host and Nonlinear Crystals*, T. J. Lin, ed., SPIE 1104, 244–250 (1989).

[14] R. S. F. Chang, V. Phomsakha, and N. Djeu, "Recent advances in sapphire fibers," in *Biomedical Optoelectronic Instrumentation*, A. Katzir, J. A. Harrington, and D. M. Harris, eds., SPIE 2396, 48–53 (1995).

[15] G. N. Merberg and J. A. Harrington, "Optical and mechanical properties of single-crystal sapphire optical fibers," Appl. Opt. 32, 3201–3209 (1993).

[16] R. K. Nubling, R. L. Kozodoy, and J. A. Harrington, "Optical properties of clad and unclad sapphire fiber," in *Biomedical Fiber Optic Instrumentation*, J. A. Harrington, D. M. Harris, A. Katzir, and F. P. Milanovich, eds., SPIE 2131, 56–61 (1994).

[17] H. E. LaBelle, Jr., "EFG, the invention and application to sapphire growth," J. Cryst. Growth 50, 8–17 (1980).

[18] G. M. Clarke, D. Chadwick, R. K. Nubling, and J. A. Harrington, "Sapphire fibers for three micron delivery systems," in *Biomedical Optoelectronic Instrumentation*, A. Katzir, J. A. Harrington, and D. M. Harris, eds., SPIE 2396, 54–59 (1995).

[19] J. J. Fitzgibbon, H. E. Bates, A. P. Pryshlak, and J. R. Dugan, "Sapphire optical fibers for the delivery of Erbium:YAG laser energy," in *Biomedical Optoelectronic Instrumentation*, A. Katzir, J. A. Harrington, and D. M. Harris, eds., SPIE 2396, 60–70 (1995).

[20] A. P. Pryshlak, J. R. Dugan, and J. J. Fitzgibbon, "Advancements in sapphire optical fibers for the delivery of Er:YAG laser energy and IR sensor applications," in *Biomedical Fiber Optics*, A. Katzir and J. A. Harrington, eds., SPIE 2677, 35–42 (1996).

[21] http://www.photran.com/photran_pages/product_pages/optical_fiber.html

[22] J. R. Pedrazzani, (2007) "Sapphire Optical Fibers" in "Specialty optical fibers handbook" editors by A. Méndez and T. F. Morse, pp.651-670, Elsevier Academic Press, Burlington, MA, USA.

[23] Saphikon, Inc. Product information. Available at *www.saphikon.com*.

[24] Merberg, G. N. and J. Harrington. 1993. Optical and mechanical properties of single crystal sapphire fibers. *Appl. Opt.* 32:3201-3209.

[25] LaBelle, H. E. et al. 1986. Recent developments in growth of shaped sapphire crystals. *SPIE Int. Soc. Opt. Eng. Proc. SPIE Int. Soc. Opt. Eng.* 683:36-40.

[26] Desu, S. B. et al. 1990. High temperature sapphire optical sensor fiber coatings. *SPIE Int. Soc. Opt. Eng. Proc. SPIE Int. Soc. Opt. Eng.* 1307:2-9.

[27] Holey Fibers with Random Cladding Distributions by T. M. Monro, P. J. Bennett, N. G. R. Broderick, and D. J. Richardson, Opt. Lett. 25, 206 , 2000

[28] Highly Birefringent Photonic Crystal Fiber with Squeezed Hexagonal and Rectangular Lattices, by Marcos A. R. Franco, Elaine C. S. Barretto, Valdir A. Serrão and Francisco Sircilli, 0-7803-9342-2/05/$20.00 © 2005 IEEE

[29] T. A. Birks, J. C. Knight, and P. S. J. Russell, "Endlessly single-mode photonic crystal fiber," Opt. Lett. 22, 961–963 (1997). [ISI] [MEDLINE]

[30] J. C. Knight, T. A. Birks, P. J. Russell, and J. P. de Sandro, "Properties of photonic crystal fiber and the effective index model," J. Opt. Soc. Am. 15, 748–752 (1998).

[31] J. C. Knight, T. A. Birks, P. St. J. Russell, and D. M. Atkin, "All-silica single-mode optical fiber with photonic crystal cladding," Opt. Lett. 21, 1547–1549 (1996). [MEDLINE]

[32] D. Kominsky, G. Pickrell, and R. Stolen, "Generation of random-hole optical fiber," Opt. Lett. 28, 1409–1411 (2003). [ISI] [MEDLINE]

[33] G. Pickrell, D. Kominsky, R. Stolen, F. Ellis, J. Kim, A. Saffaai-Jazi, and A. Wang, "Microstructural analysis of random hole optical fibers," IEEE Photon. Technol. Lett. 16(2), 491–493 (2004).

[34] T. Nasilowski, R. Kotynski, F. Berghman, and H. Thienpont, "Photonic crystal fibers—state of the art and future perspectives" Proc. SPIE 5576, 1–12 (2004)PSISDG005576000001000001000001.

[35] B. Temelkuran, S. D. Hart, G. Benoit, J. D. Joannopoulos, and Y. Fink "Wavelength-scalable hollow optical fibers with large photonics bandgaps for CO_2 laser transmission," Nature 420, 650–653 (2002). [MEDLINE]

[36] M. Korwin-Pawlowski, G. Pickrell, and P. Mikulic, "Long period gratings on random hole optical fibers and microstructured disordered fibers," Proc. SPIE 6767, 67670D (2007)PSISDG006767000001676 70D000001.

[37] G. Pickrell, W. Peng, and A. Wang, "Random-hole optical fiber evanescent-wave gas sensing," Opt. Lett. 29, 1476–1478 (2004). [ISI] [MEDLINE]

[38] B. Alfeeli, G. Pickrell, M. Garland, and A. Wang, "Behavior of random hole optical fibers under gamma ray irradiation and its potential use in radiation sensing applications," Sensors 7(5), 676–688 (2007).

[39] G. Pickrell, C. Ma, and A. Wang, "Bending-induced optical loss in random-hole optical fibers," Opt. Lett. 33, 1443–1445 (2008). [MEDLINE]

[40] John D. Joannopoulos, Robert D. Meade, and Joshua N. Winn. Photonic Crystals: Molding the Flow of Light. Princeton University Press, 1995.

[41] A. H. Cherin, An Introduction to Optical Fibers, McGraw-Hill, 1983.

[42] Gloge, D. 1972. *Bell Syst. Tech. J.* 51:1767

[43] Yeh, P., Yariv, A., and Marom, E. 1978. Theory of Bragg fibers. J. Opt. Soc. Am. 68:1196.

[44] Luan, F., George, A. K., Hedley, T. D., Pearce, G. J., Bird, D. M., Knight, J. C., and Russell, P. S. J. 2004. All-solid photonic bandgap fiber. Optics Letters 29:2369.

[45] Vincent Pureur, Géraud Bouwmans, Mathias Perrin, Yves Quiquempois, and Marc Douay, "Impact of Transversal Defects on Confinement Loss of an All-Solid 2-D Photonic-Bandgap Fiber," J. Lightwave Technol. **25**, 3589-3596 (2007)

[46] Comsol Multiphysics, version 4.1, March 2011.

[47] Jianming Jin, "The Finite Element Method in Electromagnetics," Second Edition, John Wiley & Sons, Inc, New York 2002.

[48] K. Saitoh and M. Koshiba, "Full-vectorial imaginary-distance beam propagation method based on finite element scheme: Application to photonic crystal fibers," IEEE J. Quantum Electron. **38**, 927-933 (2002).

[49] Kunimasa Saitoh and Masanori Koshiba, "Leakage loss and group velocity dispersion in air-core photonic bandgap fibers," Opt. Express **11**, 3100-3109 (2003)

[50] Wyant J.C. White light interferometry (2002) *Proceedings of SPIE - The International Society for Optical Engineering*, 4737, pp. 98-107.

[51] Yizheng Zhu, "Miniature Fiber-Optic Sensors for High-Temperature Harsh Environments," Virginia Tech Dissertation (2007)

[52] http://scienceworld.wolfram.com/physics/FringeVisibility.html

[53] G.P. Brady, K. Kalli, D.J. Webb, D.A. Jackson, L. Zhang, and I. Bennion, "Extended-range, low coherence dual wavelength interferometry using a superfluorescent fiber source and chirped fiber Bragg gratings," Opt. Commun. **134**, 341–348 (1997).

[54] K.T.V. Grattan and B.T. Meggitt, *Optical Fiber Sensor Technology*, Vol. 4, Kluwer Academic Publishers, The Netherlands (1999).

[55] L.B. Yuan and F. Ansari, "White-light interferometric fiber-optic distributed strain-sensing system," Sensors Actuators A-Physical **63**(3), 177–181 (1997).

[56] A. Wang, M.S. Miller, A.J. Plante, M.F. Gunther, K.A. Murphy, and R.O. Claus, "Split-spectrum intensity-based optical fiber sensors for measurement of micro displacement, strain, and pressure," Appl. Opt. **35**(15), 2595–2601 (1996).

[57] F. M. Mirabella, Jr., Practical Spectroscopy Series; Internal reflection spectroscopy: Theory and applications, Marcel Dekker, Inc., 1993, 17-52.

[58] Jianming Jin, "The Finite Element Method in Electromagnetics," Second Edition, John Wiley & Sons, Inc, New York 2002.

[59] G. Bouwmans, L. Bigot, Y. Quiquempois, F. Lopez, L. Provino, and M. Douay, "Fabrication and characterization of an all-solid 2D photonic bandgap fiber with a low-loss region (< 20 dB/km) around 1550 nm," Opt. Express **13**, 8452-8459 (2005)

[60] N. M. Litchinitser, S. C. Dunn, B. Usner, B. J. Eggleton, T. P. White, R. C. McPhedran, and C. M. de Sterke, "Resonances in microstructured optical waveguides," Opt. Express **11**, 1243-1251 (2003)

[61] W.D. Kingery, H.K. Bowen and D.R. Uhlmann, *Introduction to Ceramics*, John Wiley and Sons, New York, NY (1976).

[62] Pfeiffenberger, N. T., Pickrell, G., Kokal, K., and Wang, A., "Sapphire photonic crystal fibers," Opt. Eng. 49, 090501; doi:10.1117/1.3483908 (2010).

[63] Pfeiffenberger, N. T. and Pickrell, G. R. (2011) Finite Element Modeling of Sapphire Photonic Crystal Fibers, in Advances in Nanomaterials and Nanostructures, Volume 229 (eds K. Lu, N. Manjooran, M. Radovic, E. Medvedovski, E. A. Olevsky, C. Li, G. Singh, N. Chopra and G. Pickrell), John Wiley & Sons, Inc., Hoboken, NJ, USA. doi: 10.1002/9781118144602.ch10

[64] Finite Element Modeling for Mode Reduction in Bundled Sapphire Photonic Crystal Fibers. Neal Pfeiffenberger, and Gary Pickrell. MS&T 2011, Pittsburgh, PA October 19, 2011.

[65] K. A. Murphy, B. R. Fogg, G. Z. Wang, A. M. Vengsarkar, and R. O. Claus, Sapphire fiber interferometer for microdisplacement measurements at high temperatures, *SPIE-Int. Soc. Opt. Eng. Proc. of Spie — the Int. Soc. for Opt. Eng.* 1588 (1991) 117-124.

[66] G. Keiser, *Optical Fiber Communication*, McGraw-Hill Inc.: New York (1991).

[67]Pfeiffenberger, N. T., Pickrell, G., "Finite Element Modeling for Mode Reduction in Bundled Sapphire Photonic Crystal Fibers," Proc. MS&T, Columbus, OH (2011).

[68] Neal Pfeiffenberger, Gary Pickrell, Karen Kokal and Anbo Wang, "Sapphire photonic crystal fibers", *Opt. Eng.* 49, 090501 (Sep 02, 2010); doi:10.1117/1.3483908

[69] Neal Pfeiffenberger; Gary Pickrell "Finite Element Modeling of Sapphire Photonic Crys tal Fibers" Virginia Tech. MS&T, Houston, TX October 21, 2010.

[70]Pfeiffenberger, N. T., Pickrell, G., "Finite Element Modeling for Mode Reduction in Bundled Sapphire Photonic Crystal Fibers," Proc. MS&T, Columbus, OH (2011).

[71] http://americas.kyocera.com/kicc/pdf/Kyocera%20Sapphire.pdf

[72] http://ab-initio.mit.edu/wiki/index.php/MPB_Data_Analysis_Tutorial

[73] West *et al*, *Opt. Express* 12 (8), 1485 (2004)

[74] C. Ma, B. Dong, J. Gong, and A. Wang, "Decoding the spectra of low-finesse extrinsic optical fiber Fabry-Perot interferometers," Opt. Express 19, 23727-23742 (2011).

[75] R. Nubling and J. Harrington, "Optical properties of single-crystal sapphire fibers," Appl. Opt. 36, 5934-5940 (1997). http://www.emtinc.us/images/Optical_properties_sapphire_fibers.pdf

[76] media.corning.com/WorkArea/downloadasset.aspx?id=7917

[77] http://www.thorlabs.us/Thorcat/13000/13053-S01.pdf

Appendix A. MPB Code for 7-rod structure with each rod being 35 μm radius, with all rods touching one another

```
(set! num-bands 8) ;

(set! geometry-lattice (make lattice (size 1 1 no-size)
                        (basis1 (/ (sqrt 3) 2) 0.5)
                (basis2 (/ (sqrt 3) 2) -0.5)
                        (basis-size .7 .7 .7)))

(define-param kz 0) ; use non-zero kz to consider vertical propagation

(set! k-points (list (vector3 0 0 kz)         ; Gamma
                (vector3 0 0.5 kz)       ; M
                (vector3 (/ -3) (/ 3) kz) ; K
                (vector3 0 0 kz)))       ; Gamma

(set! k-points (interpolate 4 k-points))

(set! default-material (make dielectric (epsilon 1))) ; the dielectric constant of the background is air

(set! geometry (list (make cylinder
```

```
                (center 0 0 0) (radius .35) (height infinity)
                (material (make dielectric (epsilon 11.5))))))

;(define-param eps_background 2)



(set! resolution 32)

;(run-tm (output-at-kpoint (vector3 (/ -3) (/ 3) 0)
;                fix-efield-phase output-efield-z))
(run-tm)
(run-te)
```

Appendix B. Band Table for Differing Rod/Hole Radius and Spacing

Rods Case:
r =0.35 and a varies 0.1 to 10
TE entire data range

			TE Gap						
r	a	r/a	Bandgap 1-2 (%)	Band 2-3 (%)	Band 3-4 (%)	Bandgap 4-5 (%)	Band 5-6 (%)	Band 6-7 (%)	Band 7-8 (%)
0.35	0.7	0.5	0	0	0	0	0	0	0
0.35	0.75	0.466666667	0	0	0.087353329	0	0	0	0
0.35	0.8	0.4375	4.734104515	0	0.083693614	0	0.308996074	0.118276543	0
0.35	0.85	0.411764706	8.06455155	0	0.073996934	0	0.22886654	0	0
0.35	0.9	0.388888889	8.86710895	0.65279282	0.252909162	0.230517624	0.218926341	0	0
0.35	0.95	0.368421053	9.850272763	0.445632491	0.022834031	0.161482349	0.092852283	0	0
0.35	1	0.35	10.19024031	0.35986537	0.19627007	0	0.126021706	0	0
0.35	1.05	0.333333333	9.840581068	0.157423104	0.028167344	0			
0.35	1.1	0.318181818	9.319574418	0.207233687	0.190238383	0	0.020591741	0	0
0.35	1.15	0.304347826	8.160761101	0.249340238	0.064360484	0	0.105769299	0.367735956	
0.35	1.2	0.291666667	6.747605007	0.505282115	0.060917185	0	0.134337522	0.117424802	0
0.35	1.25	0.28	5.334463943	0.619788663	0.247222682	0		0.209001728	
0.35	1.3	0.269230769	4.656637649	0.40675822	0.188871824	0	0	0.185363297	0
0.35	1.35	0.259259259	3.337700072	0.367777356		0		0.517617169	
0.35	1.4	0.25	1.672857011	0.728206678	0	0	0	0.322294299	0
0.35	1.45	0.24137931	1.24282019	0.063800891		0		0.366981015	
0.35	1.5	0.233333333	0	0.416473619	0	0	0	0.337688183	0
0.35	1.55	0.225806452	0	0.506457974		0.095856818		0.235449922	
0.35	1.6	0.21875	0	0.754215861	0	0.131360531	0	0.564933106	0
0.35	1.65	0.212121212	0	0.34189337		1.218921586		0.269399141	
0.35	1.7	0.205882353	0	0	0	3.86274672	0	0	0
0.35	1.75	0.2	0			6.051584192			
0.35	1.8	0.194444444	0	0	0	8.246150075	0	0	0
0.35	1.85	0.189189189	0			9.127778096			
0.35	1.9	0.184210526	0	0	0	9.111540883	0	0	0
0.35	1.95	0.179487179	0			9.155679903			
0.35	2	0.175	0	0	0	8.939376582	0	0	0
0.35	2.25	0.155555556	0			8.920047427		0.689857334	
0.35	2.5	0.14	0			7.098135003			
0.35	2.75	0.127272727	0			6.062740521			
0.35	3	0.116666667	0	0	0	5.053918524	0	0	0
0.35	3.25	0.107692308	0			4.219832792			
0.35	3.5	0.1	0			1.453486388			
0.35	3.75	0.093333333	0			0			
0.35	4	0.0875	0	0	0	0	0	0	0
0.35	4.25	0.082352941	0			0			
0.35	4.5	0.077777778	0			0			0.388952809
0.35	4.75	0.073684211	0			0			0.388952809
0.35	5	0.07	0	0	0	0	0	0	0
0.35	5.25	0.066666667	0			0			
0.35	5.5	0.063636364	0			0			
0.35	5.75	0.060869565	0			0			
0.35	6	0.058333333	0	0	0	0	0	0	0
0.35	6.25	0.056	0			0			
0.35	6.5	0.053846154	0			0			
0.35	6.75	0.051851852	0			0			
0.35	7	0.05	0	0	0	0	0	0	0
0.35	7.25	0.048275862	0			0			
0.35	7.5	0.046666667	0			0			
0.35	7.75	0.04516129	0			0			
0.35	8	0.04375	0	0	0	0	0	0	0
0.35	8.25	0.042424242	0			0			
0.35	8.5	0.041176471	0			0			
0.35	8.75	0.04	0			0			
0.35	9	0.038888889	0	0	0	0	0	0	0

TM entire data range

r	a	r/a	TM Gap Bandgap 1-2 (%)	Band 2-3 (%)	Band 3-4 (%)	Bandgap 4-5 (%)	Band 5-6 (%)	Band 6-7 (%)	Band 7-8 (%)
0.35	0.7	0.5	0	0	0	0	0	0	0
0.35	0.75	0.466666667	0	0	0	0	0	0	0
0.35	0.8	0.4375	5.088234262	0	5.338227119	0	0	0	0
0.35	0.85	0.411764706	10.54521568	0	10.23147213	0	0	3.080158261	0.215012109
0.35	0.9	0.388888889	15.46728791	0	14.23326788	0	0	7.453782838	0.700227181
0.35	0.95	0.368421053	19.50486396	0	17.48247224	0	0	9.932980543	0
0.35	1	0.35	23.28894135	0	20.25123119	0	0	12.63142011	0
0.35	1.05	0.333333333	26.55098589		22.6081997			14.63013072	
0.35	1.1	0.318181818	29.2115409	0	24.28597768	0	0	15.7115459	0
0.35	1.15	0.304347826	31.77659533		24.69111046			16.31141626	
0.35	1.2	0.291666667	34.02811589	0	24.22508005	0	0	15.44086077	0
0.35	1.25	0.28	36.27281677		23.40084565			13.69864856	
0.35	1.3	0.269230769	37.85094358	0	22.30135224	0	0	11.93493385	0
0.35	1.35	0.259259259	39.28263356		21.15338954			9.879822577	
0.35	1.4	0.25	40.91027407	0	19.30238297	0	0	7.136271389	0
0.35	1.45	0.24137931	41.93069665		17.31844051			4.697511931	
0.35	1.5	0.233333333	42.82827359	0	16.10662466	0	0	2.850225047	0
0.35	1.55	0.225806452	44.19441096		13.1446741			0.024585709	
0.35	1.6	0.21875	44.93585807	0	11.10310455	0	0	0.105670898	0
0.35	1.65	0.212121212	45.35603299		9.380541205		0.152990509	0.108624867	
0.35	1.7	0.205882353	46.04507842	0	6.983592942	0.119683383	0.182559579	0.248928389	0
0.35	1.75	0.2	46.76627236		4.106525957	0.073252358	0.186526974	0.422514138	
0.35	1.8	0.194444444	47.05728445	0	2.037550919	0	0.32767236	0.235293484	0
0.35	1.85	0.189189189	47.37658592		0.184187224		0.661723575	0.429960777	
0.35	1.9	0.184210526	47.46924944	0	0.207754451	0	0.080331704	0.086360533	0
0.35	1.95	0.179487179	47.57655294		0.087898432			0.248360946	
0.35	2	0.175	47.66565077	0	0.472973625	0	0	0.186858254	0
0.35	2.25	0.155555556	46.74734893		0.044415893			0.903709158	
0.35	2.5	0.14	44.58021641	0.544188826	0.974850793	0.212379054		0.515268023	
0.35	2.75	0.127272727	41.15091809	0.167340167	0			0.545696983	
0.35	3	0.116666667	36.97502104	0.169744666	0	0	0	0	0
0.35	3.25	0.107692308	33.28283616	0.043813382	0	1.993459489		0	
0.35	3.5	0.1	31.15677335	0.008163448	0	3.662232443		0	
0.35	3.75	0.093333333	25.72509984		0	3.914539924		0	
0.35	4	0.0875	25.72509984	0	0	3.914539421	0	0	0
0.35	4.25	0.082352941	21.44127515		0	2.760076368		0	
0.35	4.5	0.077777778	17.90040063		0	2.023769582		0	
0.35	4.75	0.073684211	17.90040063		0	2.023769582		0	
0.35	5	0.07	13.82920888	0	0	1.550262764	0	0	0
0.35	5.25	0.066666667	9.346094781		0	0.903585166		0	0.306671049
0.35	5.5	0.063636364	9.346094781		0	0.903585166		0	0.306671049
0.35	5.75	0.060869565	8.420231503		0	0.857807596		0	0.186658313
0.35	6	0.058333333	8.420231503	0	0	0.857807596	0	0	0.186658313
0.35	6.25	0.056	3.110891961		0	0.85477851		0	1.052752751
0.35	6.5	0.053846154	2.056381048		0	0.73960233		0	
0.35	6.75	0.051851852	2.056381048		0	0.73960233		0	0.964697587
0.35	7	0.05	2.056381048	0	0	0.739602401	0	0	0.9646979
0.35	7.25	0.048275862	2.056381048		0	0.739602403		0	0.9646979
0.35	7.5	0.046666667	0		0	0.460954871		0	0.449968431
0.35	7.75	0.04516129	0		0	0.460954831		0	0.449968032
0.35	8	0.04375	0	0	0	0.460954849	0	0	0.44996843
0.35	8.25	0.042424242	0		0	0.460954767		0	0.449969331
0.35	8.5	0.041176471	0		0			0	
0.35	8.75	0.04	0		0			0	
0.35	9	0.038888889	0	0	0	0	0	0	0

a=1 and r varies 0.1 to 0.5
TE entire data range

			TE Gap						
r	a	r/a	Bandgap 1-2 (%)	Band 2-3 (%)	Band 3-4 (%)	Bandgap 4-5 (%)	Band 5-6 (%)	Band 6-7 (%)	Band 7-8 (%)
0.1	1	0.1	0	0	0	1.453486	0	0	0
0.11	1	0.11	0	0	0	5.038569562	0	0	0
0.12	1	0.12	0			5.054076018	0	0	0
0.13	1	0.13	0			6.451636521	0	0	0
0.14	1	0.14	0			7.098135005	0	0	0
0.15	1	0.15	0			8.308746094	0	0	0
0.16	1	0.16	0			9.071770948	0	0.583473828	0
0.17	1	0.17	0			8.91804675	0	0	0
0.18	1	0.18	0			9.155679897	0	0	0
0.19	1	0.19	0			9.039226541	0	0	0
0.2	1	0.2	0			6.051584192	0	0	0
0.21	1	0.21	0			2.958650977	0	0	0
0.22	1	0.22	0			0.109395697	0	0	0
0.23	1	0.23	0			0.192818486	0	0	0
0.24	1	0.24	0.4408593			0	0	0	0
0.25	1	0.25	1.71226737	0.7027595		0	0	0.2482305	
0.26	1	0.26	3.095857245			0	0		
0.27	1	0.27	4.656637649			0	0		
0.28	1	0.28	5.334463943			0	0		
0.29	1	0.29	6.7074886			0	0		
0.3	1	0.3	7.5852779	0.48442329	0.0793114	0	0.173794025	0.33116649	
0.31	1	0.31	8.001840676			0			
0.32	1	0.32	9.153280588			0			
0.33	1	0.33	9.333213283			0			
0.34	1	0.34	9.770028685			0			
0.35	1	0.35	10.1902403	0.35986537	0.19627009	0	0.126021587		
0.36	1	0.36	9.789497586			0.004282238			
0.37	1	0.37	10.05417947			0.20843934			
0.38	1	0.38	9.863194432			0.232687512			
0.39	1	0.39	8.911798656			0.232921105			
0.4	1	0.4	9.1387821		0.1196137	0	0.0709691		
0.41	1	0.41	8.219475352			0			
0.42	1	0.42	6.718935259			0			
0.43	1	0.43	6.318949975			0			
0.44	1	0.44	5.223889111			0			
0.45	1	0.45	2.41478837		0.02443781	0		0.25156222	
0.46	1	0.46	1.99229329			0			
0.47	1	0.47	0			0			
0.48	1	0.48	0			0			
0.49	1	0.49	0			0			
0.5	1	0.5	0			0			
0.56	1	0.56	0			0			
0.57	1	0.57	0			0			
0.58	1	0.58	0			0			

TM entire data range

			TM Gap						
r	a	r/a	Bandgap 1-2 (%)	Band 2-3 (%)	Band 3-4 (%)	Bandgap 4-5 (%)	Band 5-6 (%)	Band 6-7 (%)	Band 7-8 (%)
0.1	1	0.1	31.15677	0.0081634	0	3.6622324		0	
0.11	1	0.11	36.35925931	0.166603666	0			0	
0.12	1	0.12	38.47831873	0.376768651	0			0	
0.13	1	0.13	42.13733101	0.150651144	0	0.314578339		0.793002841	
0.14	1	0.14	44.58021641	0.544188826	0.974850677	0.212379054		0.515268023	
0.15	1	0.15	46.06959		0.642797			0.568386388	
0.16	1	0.16	46.96973648		0.318680084			0.549396456	
0.17	1	0.17	47.67846582		0.794221639			0.638207891	
0.18	1	0.18	47.57655294		0.087898464			0.248360946	
0.19	1	0.19	47.15153209		0.430785796		0.08085	0.375689467	
0.2	1	0.2	46.766272		4.1065258	0.0732523	0.1865269	0.4225141	
0.21	1	0.21	45.82401897		7.808999129			0.01984872	
0.22	1	0.22	44.79672769		11.51474236			0.098889389	
0.23	1	0.23	43.96460424		13.70279925			0.026673639	
0.24	1	0.24	42.28150114		16.98781709			4.100896865	
0.25	1	0.25	40.872815		19.3618709			7.192397566	
0.26	1	0.26	39.28263651		21.15338897			9.8798226	
0.27	1	0.27	37.85094358		22.30135196			11.93493385	
0.28	1	0.28	36.27281677		23.40084602			13.69864856	
0.29	1	0.29	34.02811589		24.22507937			15.44086077	
0.3	1	0.3	32.452764		24.620481			16.144319	
0.31	1	0.31	31.16050226		24.65636246			16.61980663	
0.32	1	0.32	28.93500933		24.05112576			15.46340451	
0.33	1	0.33	26.97725948		22.79757443			14.63737179	
0.34	1	0.34	25.13399651		21.52136809			13.6643507	
0.35	1	0.35	23.28894135		20.2512309			12.63142	
0.36	1	0.36	21.31805889		18.82253582			11.40620086	
0.37	1	0.37	18.87532151		16.97920524			9.62997741	
0.38	1	0.38	17.11720097		15.64458529			8.449311158	
0.39	1	0.39	15.46728791		14.23326788			7.453782838	
0.4	1	0.4	12.94160385		12.2686678			5.1882752	0.3460192
0.41	1	0.41	10.76920427		10.42452855			3.526134766	
0.42	1	0.42	9.011957292		8.820207983			2.157026413	
0.43	1	0.43	6.605082657		6.771649404			0	
0.44	1	0.44	4.68694961		5.056121568			0	
0.45	1	0.45	2.1813315		2.6217486			0	
0.46	1	0.46	0.468117771		1.103488211			0	
0.47	1	0.47	0		0			0	
0.48	1	0.48	0		0			0	
0.49	1	0.49	0		0			0	
0.5	1	0.5	0		0	0	0	0	
0.56	1	0.56	0		0			0	
0.57	1	0.57	0		0			0	
0.58	1	0.58	0		0			0	

Holes Case:

r and a varies with r/a =0.5
TE entire data range

				TE Gap					
r	a	r/a	Bandgap 1-2 (%)	Band 2-3 (%)	Band 3-4 (%)	Band 4-5 (%)	Band 5-6 (%)	Band 6-7 (%)	Band 7-8 (%)
0.1	0.2	0.5	5.415728832						0.40723338
0.2	0.4	0.5	5.526764844						0.463830336
0.3	0.6	0.5	5.971781815						0.367492357
0.4	0.8	0.5	5.526764844						0.463830336
0.5	1	0.5	5.415728832						0.40723338
0.6	1.2	0.5	5.971781815						0.367492357
0.7	1.4	0.5	5.526766964						0.463830336
0.8	1.6	0.5	5.526764844						0.463830337
0.9	1.8	0.5	5.526764844						0.463830336
1	2	0.5	5.415728441						0.40723338
2	4	0.5	5.415728441						
3	6	0.5	5.415728441						
4	8	0.5	5.415728441						
5	10	0.5	5.415728441						
6	12	0.5	5.415728441						
7	14	0.5	5.415728441						
8	16	0.5	5.415728441						
9	18	0.5	5.526764844						
10	20	0.5	5.415728441						

TM entire data range

						TM Gap			
r	a	r/a	Band 1-2 (%)	Band 2-3 (%)	Band 3-4 (%)	Band 4-5 (%)	Band 5-6 (%)	Band 6-7 (%)	Band 7-8 (%)
0.1	0.2	0.5	0.373185635	19.81263342			7.213436629		7.490315643
0.2	0.4	0.5	0.410429677	19.78694769			7.271796301		7.461066013
0.3	0.6	0.5	0.373755359	19.73623048			7.329092676		7.378716102
0.4	0.8	0.5	0.410429677	19.78694772			7.271796451		7.461066013
0.5	1	0.5	0.373185635	19.81263342			7.213436629		7.490315643
0.6	1.2	0.5	0.373755359	19.7362306			7.329092562		7.378716102
0.7	1.4	0.5	0.410429677	19.78694793			7.271796451		7.461066013
0.8	1.6	0.5	0.410429677	19.78694608			7.271796451		7.461066013
0.9	1.8	0.5	0.410429677	19.78694113			7.271796451		7.461066013
1	2	0.5	0.373185635	19.81263327			7.2134367		7.490315643
2	4	0.5		19.81263321			7.213436698		7.490315643
3	6	0.5		19.812633			7.213436698		7.490315643
4	8	0.5		19.81263342			7.213436698		7.490315643
5	10	0.5		19.81263324			7.213436698		7.490315643
6	12	0.5		19.81263342			7.213436698		7.490315643
7	14	0.5		19.81263288			7.213436698		7.490315643
8	16	0.5		19.8126324			7.213436698		7.490315643
9	18	0.5		19.78694461			7.271796451		7.461066013
10	20	0.5		19.81263131			7.213436698		7.490315643

r =0.35 and a varies 0.1 to 10
TE entire data range

			TE Gap						
r	a	r/a	Bandgap 1-2 (%)	Band 2-3 (%)	Band 3-4 (%)	Band 4-5 (%)	Band 5-6 (%)	Band 6-7 (%)	Band 7-8 (%)
0.35	0.6	0.583333333	0	0	0	0	0	0	0
0.35	0.65	0.538461538	0	0	0	0	0	0	0
0.35	0.66	0.53030303	0						0
0.35	0.67	0.52238806	0						0
0.35	0.68	0.514705882	0						0
0.35	0.69	0.507246377	0						0
0.35	0.7	0.5	5.526764844	0	0	0	0	0	0.463830336
0.35	0.71	0.492957746	16.15156437						0.010453657
0.35	0.72	0.486111111	25.72110357						0.960915071
0.35	0.73	0.479452055	32.22696483		1.688957547				1.672940558
0.35	0.74	0.472972973	37.55513521						1.007881981
0.35	0.75	0.466666667	40.85909822	0	0	0.170932144	0	0	0.106016859
0.35	0.76	0.460526316	44.22186749						0.037424864
0.35	0.77	0.454545455	45.68689004						0.96421243
0.35	0.78	0.448717949	47.28112721				1.364658058		1.377596235
0.35	0.79	0.443037975	48.42051365				1.580389359		1.414010071
0.35	0.8	0.4375	49.34024792	0	0	0	0.338493549	0	1.232669595
0.35	0.81	0.432098765	48.61100422				1.147407679		1.599084474
0.35	0.82	0.426829268	49.59130437						1.311734161
0.35	0.83	0.421686747	49.96284226						1.15855233
0.35	0.84	0.416666667	49.09960624						1.066503708
0.35	0.85	0.411764706	49.12545769	0	0	0	0	0	1.005918468
0.35	0.86	0.406976744	48.63919668						0.751926899
0.35	0.87	0.402298851	48.06573732						0.884379364
0.35	0.88	0.397727273	48.63919668						0.751926899
0.35	0.89	0.393258427	46.9838112						0.133951048
0.35	0.9	0.388888889	46.19592262	0	0	0	0.944398314	0	0
0.35	0.95	0.368421053	42.75135201	0	0	0	0	0	1.196725089
0.35	1	0.35	38.51438992	0	0	0	0	0	2.805233972
0.35	1.05	0.333333333	34.93216324	0	0	0	0	1.025681102	3.710482959
0.35	1.1	0.318181818	31.64085107	0	0	0	0	0	4.350817259
0.35	1.15	0.304347826	28.45375092	0	0	0	0	0	4.968864907
0.35	1.2	0.291666667	25.48673651	0	0	0	0	0	5.040756727
0.35	1.25	0.28	22.56451159	0	0	0	0	0	4.423001899
0.35	1.3	0.269230769	20.2309535	0	0	0	0	0	3.350955517
0.35	1.35	0.259259259	18.3937549	0	0	0	0	0	2.620087669
0.35	1.4	0.25	16.07626794	0	0	0	0	0	1.576687671
0.35	1.45	0.24137931	14.3352115	0	0	0	0	0	0.535254008
0.35	1.5	0.233333333	13.18815684	0	0	0	0	0	0.060915336
0.35	1.55	0.225806452	10.97324191	0	0	0	0	0	0
0.35	1.6	0.21875	9.714003808	0	0	0	0	0	0
0.35	1.65	0.212121212	8.792644167	0	0	0	0	0	0
0.35	1.7	0.205882353	7.465970305	0	0	0	0	0	0
0.35	1.75	0.2	6.193710684	0	0	0	0	0	0
0.35	1.8	0.194444444	5.115397438	0	0	0	0	0	0
0.35	1.85	0.189189189	3.820249773	0	0	0	0	0	0
0.35	1.9	0.184210526	3.290024074	0	0	0	0	0	0
0.35	1.95	0.179487179	2.393014558	0	0	0	0	0	0
0.35	2	0.175	1.464526157	0	0	0	0	0	0
0.35	2.05	0.170731707	1.034908261	0	0	0	0	0	0
0.35	2.1	0.166666667	0.550125038	0	0	0	0	0	0

TM entire data range

			TM Gap						
r	a	r/a	Bandgap 1-2 (%)	Band 2-3 (%)	Band 3-4 (%)	Band 4-5 (%)	Band 5-6 (%)	Band 6-7 (%)	Band 7-8 (%)
0.35	0.6	0.583333333	0	0	0	0	0	0	0
0.35	0.65	0.538461538	0	0	5.479060951	0	0.992140386	0	0
0.35	0.66	0.53030303		0	7.405301268		2.932189339	0	0
0.35	0.67	0.52238806	0.122105652	4.995976558	11.03651144		6.233505167	0	0
0.35	0.68	0.514705882	0.005303838	10.62297291	10.09454243		7.777669579	0	0
0.35	0.69	0.507246377	0.019345254	14.65387765	6.071306198		7.036952022	0	2.838618833
0.35	0.7	0.5	0.410429676	19.78694664	0	0	7.271796451	0	7.461066013
0.35	0.71	0.492957746	0.097878648	18.60389537	0		8.358414574	0	7.697650062
0.35	0.72	0.486111111		18.40542208	0		8.739060159	0	6.682011985
0.35	0.73	0.479452055		16.05917232	0		7.298196529	0	5.347112801
0.35	0.74	0.472972973		15.5510761	0		4.225442743	0	3.368062265
0.35	0.75	0.466666667	0.211548463	13.44735866	0.45073924	0.018421761	3.239008352	0	2.109785936
0.35	0.76	0.460526316		11.10316342	0.155258579		1.229396055	0	0.479882906
0.35	0.77	0.454545455		9.965596762	0.304910221		0.296434206	0	0.714033961
0.35	0.78	0.448717949		8.810123064	0.297832992		0.036714803	0	1.748907722
0.35	0.79	0.443037975		7.504137247	0.082483657		0.132771561	0	3.039839727
0.35	0.8	0.4375	0.165272548	6.115757552	0.277424545	0.01090749	0.152631301	0	3.435481803
0.35	0.81	0.432098765		5.805454571	0.495983498		0.400698634	1.072713536	3.764323137
0.35	0.82	0.426829268		4.17118347	0.091968285		0.324809344	1.048371393	4.567399347
0.35	0.83	0.421686747		2.863307563	0.419211112		0.164402445	1.489582695	5.136895812
0.35	0.84	0.416666667		2.694540776	0.1036848		0.47472137	2.733005519	5.519368676
0.35	0.85	0.411764706	0.104072586	1.107290316	0.040766898	0.180123058	0.19890603	2.512245898	5.983686727
0.35	0.86	0.406976744		0.169570616	0.237634258		0.110075	3.191489446	6.125349524
0.35	0.87	0.402298851		0	0.343659845		0.358752507	3.389586802	6.30081647
0.35	0.88	0.397727273		0	0.237634258		0.110075	3.191489446	6.125349524
0.35	0.89	0.393258427		0	0.149928045		0.041592619	1.442826534	5.388320672
0.35	0.9	0.388888889	0.208796609	0	0.167892126	0.078660551	0.41859643	0.941754377	4.63627398
0.35	0.95	0.368421053	0.055902386	0	0.085450329	0.021529023	0.073974806	0.145425876	0.723655207
0.35	1	0.35	0.039747147	0	0.094770556	0.016192502	0	0.550550814	0
0.35	1.05	0.333333333	0.009143605	0	0.066711661	0	0	1.025681102	0
0.35	1.1	0.318181818	0.030147921	0	2.21543E-07	0	0	0.756338722	0
0.35	1.15	0.304347826	0.048758887	0	0.06715151	0	0	0.640154648	0
0.35	1.2	0.291666667	0.016777906	0	0.083830699	0	0	0.576847332	0
0.35	1.25	0.28	0	0	0.018055723	0	0	0.377246578	0
0.35	1.3	0.269230769	0	0	0.053946925	0	0	0.050175996	0
0.35	1.35	0.259259259	0	0	0.016926006	0	0	0.292306508	0
0.35	1.4	0.25	0	0	0	0	0	0.636599474	0
0.35	1.45	0.24137931	0	0	0	0	0	1.042271493	0
0.35	1.5	0.233333333	0	0	0	0	0	1.228929812	0
0.35	1.55	0.225806452	0	0	0	0	0	0	0
0.35	1.6	0.21875	0	0	0	0	0	0	0
0.35	1.65	0.212121212	0	0	0	0	0	0	0
0.35	1.7	0.205882353	0	0	0	0	0	0	0
0.35	1.75	0.2	0	0	0	0	0	0	0
0.35	1.8	0.194444444	0	0	0	0	0	0	0
0.35	1.85	0.189189189	0	0	0	0	0	0	0
0.35	1.9	0.184210526	0	0	0	0	0	0	0
0.35	1.95	0.179487179	0	0	0	0	0	0	0
0.35	2	0.175	0	0	0	0	0	0	0
0.35	2.05	0.170731707	0	0	0	0	0	0	0
0.35	2.1	0.166666667	0	0	0	0	0	0	0

a=1 and r varies 0.1 to 0.5
TE entire data range

			TE Gap						
r	a	r/a	Bandgap 1-2 (%)	Band 2-3 (%)	Band 3-4 (%)	Band 4-5 (%)	Band 5-6 (%)	Band 6-7 (%)	Band 7-8 (%)
0.05	1	0.05	0						0
0.1	1	0.1	0						0
0.15	1	0.15	0						0
0.2	1	0.2	6.19371068						0
0.21	1	0.21	7.900756335						0
0.22	1	0.22	9.950604221						0
0.23	1	0.23	11.46736181						0
0.24	1	0.24	13.87613198						0.394010185
0.25	1	0.25	16.108959						1.578661
0.26	1	0.26	18.36042648						2.425809265
0.27	1	0.27	20.2309535						3.350955517
0.28	1	0.28	22.56451159						4.423001899
0.29	1	0.29	25.52331714						4.972138613
0.3	1	0.3	27.591106						4.9126854
0.31	1	0.31	29.26887135						5.153193196
0.32	1	0.32	32.00369007						4.281742831
0.33	1	0.33	34.42853572						4.123636552
0.34	1	0.34	36.69617787						3.529597243
0.35	1	0.35	38.514389						2.80523397
0.36	1	0.36	40.84770882						2.207218413
0.37	1	0.37	43.30244113						1.315158837
0.38	1	0.38	44.84674706						0.060019633
0.39	1	0.39	46.21973178						0
0.4	1	0.4	47.95874	0.00751499					0.3743671
0.41	1	0.41	48.8591613						1.072970984
0.42	1	0.42	49.35610687						1.184406321
0.43	1	0.43	49.22169269						1.357670937
0.44	1	0.44	48.57066069				0.959525344		1.277010788
0.45	1	0.45	47.28094				0.8605442		1.18866
0.46	1	0.46	44.32532587				1.248397277		1.188660036
0.47	1	0.47	39.07500592						0.48821187
0.48	1	0.48	32.32795866		2.143910438				1.067203438
0.49	1	0.49	18.17254162						0.142750441
0.5	1	0.5	5.415728						0.40723337

TM entire data range

			TM Gap						
r	a	r/a	Bandgap 1-2 (%)	Band 2-3 (%)	Band 3-4 (%)	Band 4-5 (%)	Band 5-6 (%)	Band 6-7 (%)	Band 7-8 (%)
0.05	1	0.05		0			0	0	0
0.1	1	0.1		0			0	0	0
0.15	1	0.15		0			0	0	0
0.2	1	0.2		0			0	0	0
0.21	1	0.21		0			0	0	0
0.22	1	0.22		0			0	0	0
0.23	1	0.23		0			0	0.28781885	0
0.24	1	0.24		0			0	1.090316165	0
0.25	1	0.25		0			0	0.64054916	0
0.26	1	0.26		0			0	0.292306508	0
0.27	1	0.27		0			0	0.050175996	0
0.28	1	0.28		0			0	0.377246578	0
0.29	1	0.29		0			0	0.576847332	0
0.3	1	0.3	0.0612465	0	0.0181099		0	0.6527321	0
0.31	1	0.31		0			0	0.911708518	0
0.32	1	0.32		0			0	0.745604846	0
0.33	1	0.33		0			0	0.936113081	0
0.34	1	0.34		0			0	1.130295588	0
0.35	1	0.35	0.0397471	0	0.09477058	0.0161925	0	0.55055081	0
0.36	1	0.36		0			0	0.343813649	0
0.37	1	0.37		0			0.054913891	0.29474647	1.246302475
0.38	1	0.38		0			0.07317925	0.310173088	2.919263463
0.39	1	0.39		0			0.41859609	0.941754377	4.636275602
0.4	1	0.4	0.033638	0	0.0805786	0.03944703	0.14654898	2.8402708	6.598972
0.41	1	0.41		1.070396815			0.041851342	2.915216443	5.859034411
0.42	1	0.42		2.986095054			0.17649608	2.412005126	5.339860684
0.43	1	0.43		5.044632346			0.236539268	1.11447876	4.118406969
0.44	1	0.44		6.895918601			0.162615803	0.191470412	3.17839257
0.45	1	0.45	0.1175979	8.6124795	0.4375659	0.4375659	0.300509	0	1.620268
0.46	1	0.46		11.27714676			0.726239446	0	0.48114346
0.47	1	0.47		14.59533211			3.418444631	0	2.92001288
0.48	1	0.48		16.05917278			7.298196541	0	5.347112801
0.49	1	0.49		17.32765443			9.188704953	0	6.692230969
0.5	1	0.5	0.373185	19.812633			7.213436	0	7.4903156

Full band gap case (air holes)
r and a varies with r/a =0.5
TE entire data range

			TE Gap						
r	a	r/a	Band 1-2 (%)	Band 2-3(%)	Band 3-4(%)	Band 4-5(%)	Band 5-6(%)	Band 6-7(%)	Band 7-8 (%)
0.1	0.2	0.5	5.415728832						0.40723338
0.2	0.4	0.5	5.526764844						0.463830336
0.3	0.6	0.5	5.971781815						0.367492357
0.4	0.8	0.5	5.526764844						0.463830336
0.5	1	0.5	5.415728832						0.40723338
0.6	1.2	0.5	5.971781815						0.367492357
0.7	1.4	0.5	5.526766964						0.463830336
0.8	1.6	0.5	5.526764844						0.463830337
0.9	1.8	0.5	5.526764844						0.463830336
1	2	0.5	5.415728441						0.40723338
2	4	0.5	5.415728441						
3	6	0.5	5.415728441						
4	8	0.5	5.415728441						
5	10	0.5	5.415728441						
6	12	0.5	5.415728441						
7	14	0.5	5.415728441						
8	16	0.5	5.415728441						
9	18	0.5	5.526764844						
10	20	0.5	5.415728441						

TM entire data range

		TM Gap							
r	a	r/a	Band 1-2 (%)	Band 2-3 (%)	Band 3-4(%)	Band 4-5(%)	Band 5-6 (%)	Band 6-7(%)	Band 7-8 (%)
0.1	0.2	0.5	0.373185635	19.81263342			7.213436629		7.490315643
0.2	0.4	0.5	0.410429677	19.78694769			7.271796301		7.461066013
0.3	0.6	0.5	0.373755359	19.73623048			7.329092676		7.378716102
0.4	0.8	0.5	0.410429677	19.78694772			7.271796451		7.461066013
0.5	1	0.5	0.373185635	19.81263342			7.213436629		7.490315643
0.6	1.2	0.5	0.373755359	19.7362306			7.329092562		7.378716102
0.7	1.4	0.5	0.410429677	19.78694793			7.271796451		7.461066013
0.8	1.6	0.5	0.410429677	19.78694608			7.271796451		7.461066013
0.9	1.8	0.5	0.410429677	19.78694113			7.271796451		7.461066013
1	2	0.5	0.373185635	19.81263327			7.2134367		7.490315643
2	4	0.5		19.81263321			7.213436698		7.490315643
3	6	0.5		19.812633			7.213436698		7.490315643
4	8	0.5		19.81263342			7.213436698		7.490315643
5	10	0.5		19.81263324			7.213436698		7.490315643
6	12	0.5		19.81263342			7.213436698		7.490315643
7	14	0.5		19.81263288			7.213436698		7.490315643
8	16	0.5		19.8126324			7.213436698		7.490315643
9	18	0.5		19.78694461			7.271796451		7.461066013
10	20	0.5		19.81263131			7.213436698		7.490315643

Full Bandgap data

r	a	r/a	Full Band Gap	Bandgap (%)	Bandgap	Min Frequency	Max Frequency	Midgap Freq
0.1	0.2	0.5	TE-2 & TE-1	5.526663248	0.14713	2.58862	2.73575	2.662185
0.2	0.4	0.5	TE-2 & TE-1	5.527028499	0.07357	1.29431	1.36788	1.331095
0.3	0.6	0.5	TE-2 & TE-1	5.971830349	0.052861	0.858742	0.911603	0.8851725
0.4	0.8	0.5	TE-2 & TE-1	5.526736299	0.036783	0.647155	0.683938	0.6655465
0.5	1	0.5	TE-2 & TE-1	5.415734745	0.028851	0.5183	0.547151	0.5327255
0.6	1.2	0.5	TE-2 & TE-1	5.97172075	0.02643	0.429371	0.455801	0.442586
0.7	1.4	0.5	TE-2 & TE-1	5.526770748	0.021019	0.369803	0.390822	0.3803125
0.8	1.6	0.5	TE-2 & TE-1	5.526581894	0.018391	0.323578	0.341969	0.3327735
0.9	1.8	0.5	TE-2 & TE-1	5.526725919	0.016348	0.287625	0.303973	0.295799
1	2	0.5	TE-2 & TE-1	5.415552114	0.014425	0.25915	0.273575	0.2663625
2	4	0.5	TE-2 & TE-1	5.415917376	0.007213	0.129575	0.136788	0.1331815
3	6	0.5	TE-2 & TE-1	5.415736778	0.0048085	0.0863833	0.0911918	0.08878755
4	8	0.5	TE-2 & TE-1	5.415625167	0.0036063	0.0647875	0.0683938	0.06659065
5	10	0.5	TE-2 & TE-1	5.415734745	0.0028851	0.05183	0.0547151	0.05327255
6	12	0.5	TE-2 & TE-1	5.4156211	0.0024042	0.0431917	0.0455959	0.0443938
7	14	0.5	TE-2 & TE-1	5.415775338	0.0020608	0.0370214	0.0390822	0.0380518
8	16	0.5	TE-2 & TE-1	5.415779404	0.0018032	0.0323937	0.0341969	0.0332953
9	18	0.5	TE-2 & TE-1	5.526725919	0.0016348	0.0287625	0.0303973	0.0295799
10	20	0.5	TE-2 & TE-1	5.415552114	0.0014425	0.025915	0.0273575	0.02663625

r =0.35 and a varies 0.1 to 10
TE entire data range

			TE Gap						
r	a	r/a	Band 1-2 (%)	Band 2-3	Band 3-4	Band 4-5 (%)	Band 5-6	Band 6-7	Band 7-8
0.35	0.66	0.53030303							
0.35	0.67	0.52238806							
0.35	0.68	0.514705882							
0.35	0.69	0.507246377							
0.35	0.7	0.5	5.526764844	0	0	0	0	0	0.463830336
0.35	0.71	0.492957746	16.15156437						0.010453657
0.35	0.72	0.486111111	25.72110357						0.960915071
0.35	0.73	0.479452055	32.22696483		1.688957547				1.672940558
0.35	0.74	0.472972973	37.55513521						1.007881981
0.35	0.75	0.466666667	40.85909822	0	0	0.170932144	0	0	0.106016859
0.35	0.76	0.460526316	44.22186749						
0.35	0.77	0.454545455	45.68689004						
0.35	0.78	0.448717949	47.28112721				1.364658058		1.377596235
0.35	0.79	0.443037975	48.42051365				1.580389359		1.414010071
0.35	0.8	0.4375	49.34024792	0	0	0	0.338493549	0	1.232669595
0.35	0.81	0.432098765	48.61100422				1.147407679		1.599084474
0.35	0.82	0.426829268	49.59130437						1.311734161
0.35	0.83	0.421686747	49.96284226						1.15855233
0.35	0.84	0.416666667	49.09960624						1.066503708
0.35	0.85	0.411764706	49.12545769	0	0	0	0	0	1.005918468
0.35	0.86	0.406976744	48.63919668						0.751926899
0.35	0.87	0.402298851	48.06573732						
0.35	0.88	0.397727273							
0.35	0.89	0.393258427							

TM entire data range

			TM Gap						
r	a	r/a	Band 1-2 (%)	Band 2-3	Band 3-4 (%)	Band 4-5	Band 5-6	Band 6-7 (%)	Band 7-8
0.35	0.66	0.53030303			7.405301268		2.932189339		
0.35	0.67	0.52238806	0.122105652	4.995976558	11.03651144		6.233505167		
0.35	0.68	0.514705882	0.005303838	10.62297291	10.09454243		7.777669579		
0.35	0.69	0.507246377	0.019345254	14.65387765	6.071306198		7.036952022		2.838618833
0.35	0.7	0.5	0.410429676	19.78694664	0	0	7.271796451	0	7.461066013
0.35	0.71	0.492957746	0.097878648	18.60389537			8.358414574		7.697650062
0.35	0.72	0.486111111		18.40542208			8.739060159		6.682011985
0.35	0.73	0.479452055		16.05917232			7.298196529		5.347112801
0.35	0.74	0.472972973		15.5510761			4.225442743		3.368062265
0.35	0.75	0.466666667	0.211548463	13.44735866	0.45073924	0.018421761	3.239008352	0	2.109785936
0.35	0.76	0.460526316		11.10316342			1.229396055		
0.35	0.77	0.454545455		9.965596762				c	
0.35	0.78	0.448717949		8.810123064					1.748907722
0.35	0.79	0.443037975		7.504137247					3.039839727
0.35	0.8	0.4375	0.165272548	6.115757552	0.277424545	0.01090749	0.152631301	0	3.435481803
0.35	0.81	0.432098765		5.805454571				1.072713536	3.764323137
0.35	0.82	0.426829268		4.17118347				1.048371393	4.567399347
0.35	0.83	0.421686747		2.863307563				1.489582695	5.136895812
0.35	0.84	0.416666667		2.694540776				2.733005519	5.519368676
0.35	0.85	0.411764706	0.104072586	1.107290316	0.040766898	0.180123058	0.19890603	2.512245898	5.983686727
0.35	0.86	0.406976744		0.169570616				3.191489446	6.125349524
0.35	0.87	0.402298851						3.389586802	6.30081647
0.35	0.88	0.397727273							
0.35	0.89	0.393258427							

Full Bandgap data

r	a	r/a	Full Band Gap	Bandgap (%)	Midgap freq	Min Frequency	Max Frequency
0.35	0.66	0.53030303	no full band gap				
0.35	0.67	0.52238806	no full band gap				
0.35	0.68	0.514705882	no full band gap				
0.35	0.69	0.507246377	no full band gap				
0.35	0.7	0.5	TE-2 & TE-1	5.526770748	0.760625	0.739606	0.781644
0.35	0.71	0.492957746	TE-2 & TM-2	9.527027445	0.7280655	0.693384	0.762747
0.35	0.72	0.486111111	TE-2 & TM-2	13.02382526	0.697537	0.652114	0.74296
0.35	0.73	0.479452055	TE-2 & TM-2	14.26381735	0.6788295	0.630416	0.727243
0.35	0.74	0.472972973	TM-3 & TM-2	15.55102394	0.6406845	0.590868	0.690501
0.35	0.75	0.466666667	TM-3 & TM-2	13.44735866	0.6185345	0.576946	0.660123
0.35	0.76	0.460526316	TM-3 & TM-2	11.10316342	0.5865005	0.55394	0.619061
0.35	0.77	0.454545455	TM-3 & TM-2	9.965596762	0.5645745	0.536443	0.592706
0.35	0.78	0.448717949	TM-3 & TM-2	8.810123064	0.5468745	0.522784	0.570965
0.35	0.79	0.443037975	TM-3 & TM-2	7.504137247	0.5235115	0.503869	0.543154
0.35	0.8	0.4375	TM-3 & TM-2	6.115757552	0.50918	0.49361	0.52475
0.35	0.81	0.432098765	TM-3 & TM-2	5.805454571	0.494333	0.479984	0.508682
0.35	0.82	0.426829268	TM-3 & TM-2	4.17118347	0.4809555	0.470925	0.490986
0.35	0.83	0.421686747	TM-3 & TM-2	2.863307563	0.4675385	0.460845	0.474232
0.35	0.84	0.416666667	TM-3 & TM-2	2.694540776	0.4553095	0.449175	0.461444
0.35	0.85	0.411764706	TM-3 & TM-2	1.107290316	0.44415	0.441691	0.446609
0.35	0.86	0.406976744	TM-3 & TM-2	0.169570616	0.432895	0.432528	0.433262
0.35	0.87	0.402298851	no full band gap				
0.35	0.88	0.397727273					
0.35	0.89	0.393258427					

a=1 and r varies 0.1 to 0.5

TE entire data range

			TE Gap						
r	a	r/a	Band 1-2 (%)	Band 2-3	Band 3-4	Band 4-5	Band 5-6	Band 6-7	Band 7-8 (%)
0.41	1	0.41	48.8591613						1.072970984
0.42	1	0.42	49.35610687						1.184406321
0.43	1	0.43	49.22169269						1.357670937
0.44	1	0.44	48.57066069				0.959525344		1.277010788
0.45	1	0.45	47.28094				0.8605442		1.18866
0.46	1	0.46	44.32532587				1.248397277		1.188660036
0.47	1	0.47	39.07500592						
0.48	1	0.48	32.32795866		2.143910438				1.067203438
0.49	1	0.49	18.17254162						
0.5	1	0.5	5.415728						0.40723337

TM entire data range

					TM Gap				
r	a	r/a	Band 1-2	Band 2-3 (%)	Band 3-4	Band 4-5	Band 5-6 (%)	Band 6-7	Band 7-8 (%)
0.41	1	0.41		1.070396815				2.915216443	5.859034411
0.42	1	0.42		2.986095054				2.412005126	5.339860684
0.43	1	0.43		5.044632346				1.11447876	4.118406969
0.44	1	0.44		6.895918601					3.17839257
0.45	1	0.45	0.1175979	8.6124795	0.4375659	0.4375659	0.300509		1.620268
0.46	1	0.46		11.27714676					
0.47	1	0.47		14.59533211			3.418444631		2.92001288
0.48	1	0.48		16.05917278			7.298196541		5.347112801
0.49	1	0.49		17.32765443			9.188704953		6.692230969
0.5	1	0.5	0.373185	19.812633			7.213436		7.4903156

Full Bandgap data

r	a	r/a	Full Band Gap	Bandgap (%)	Min Frequency	Midgap freq	Max Frequency
0.41	1	0.41	TM-3 & TM-2	0.010705332	0.37434	0.3763545	0.378369
0.42	1	0.42	TM-3 & TM-2	0.02986106	0.379202	0.3849495	0.390697
0.43	1	0.43	TM-3 & TM-2	0.050446798	0.387578	0.397607	0.407636
0.44	1	0.44	TM-3 & TM-2	0.068958616	0.395611	0.4097385	0.423866
0.45	1	0.45	TM-3 & TM-2	0.086123397	0.410005	0.428455	0.446905
0.46	1	0.46	TM-3 & TM-2	0.112772264	0.41802	0.442999	0.467978
0.47	1	0.47	TM-3 & TM-2	0.145953482	0.435211	0.4694715	0.503732
0.48	1	0.48	**TE-2 & TM-2**	0.143078924	0.460204	0.4956635	0.531123
0.49	1	0.49	**TE-2 & TM-2**	**0.175040055**	0.487321	0.5133625	0.539404
0.5	1	0.5	TE-2 & TE-1	0.054157347	0.5183	0.5327255	0.547151

Appendix C. Numerical Aperture Table

Excel data for single rod of single crystal sapphire, 70 µm in diameter, 1 m in length.

			Single Rod sapphire 1m long 70um diameter		
			-0.167	in dark	
			Single Rod Run 1	Single Rod Run 2	Single Rod Run 3
x	y	Angle (°)	(V)	(V)	(V)
-1.375	2.75	-26.5651	-0.167	-0.167	-0.166
-1.25	2.75	-24.444	-0.167	-0.144	-0.152

-1.125	2.75	-22.249	-0.163	-0.151	-0.143
-1	2.75	-19.9831	-0.149	-0.134	-0.13
-0.875	2.75	-17.6501	-0.126	-0.098	-0.113
-0.75	2.75	-15.2551	-0.101	-0.1	-0.102
-0.625	2.75	-12.8043	-0.076	-0.074	-0.99
-0.5	2.75	-10.3048	-0.033	0.004	-0.03
-0.375	2.75	-7.76517	0.031	0.124	0.086
-0.25	2.75	-5.19443	0.105	0.2	0.065
-0.125	2.75	-2.60256	0.2	0.39	0.27
0	2.75	0	0.37	0.49	0.409
0.125	2.75	2.602562	0.26	0.328	0.19
0.25	2.75	5.194429	0.13	0.135	0.172
0.375	2.75	7.765166	0.022	0.03	0.03
0.5	2.75	10.30485	-0.045	-0.03	-0.037
0.625	2.75	12.80427	-0.109	-0.067	-0.083
0.75	2.75	15.25512	-0.117	-0.084	-0.11
0.875	2.75	17.65012	-0.13	-0.104	-0.12
1	2.75	19.98311	-0.136	-0.129	-0.131
1.125	2.75	22.24902	-0.143	-0.16	-0.155
1.25	2.75	24.44395	-0.156	-0.156	-0.16
1.375	2.75	26.56505	-0.167	-0.166	-0.167
		5%	-0.14015	-0.13415	-0.1382
		NA value	0.345395552	0.344992215	0.340456204
		NA avg	0.343614657		

Excel data for 7-rod bundled single crystal sapphire fiber, 70 µm in diameter, 1 m in length.

			Bundled 7-Rod sapphire 1m long 70um diameter		
			-0.168	in dark	
			7-Rod Bundle Run 1	7-Rod Bundle Run 2	7-Rod Bundle Run 3
x	y	Angle (°)	(V)	(V)	(V)
-1.375	2.75	-26.5651	-0.168	-0.168	-0.168
-1.25	2.75	-24.444	-0.158	-0.157	-0.152
-1.125	2.75	-22.249	-0.135	-0.137	-0.134
-1	2.75	-19.9831	-0.081	-0.079	-0.077
-0.875	2.75	-17.6501	-0.059	-0.061	-0.061
-0.75	2.75	-15.2551	-0.016	-0.0216	-0.031

-0.625	2.75	-12.8043	0.0011	0.0138	0.0143
-0.5	2.75	-10.3048	0.0186	0.0213	0.0214
-0.375	2.75	-7.76517	0.334	0.344	0.345
-0.25	2.75	-5.19443	0.528	0.538	0.545
-0.125	2.75	-2.60256	1.108	1.143	1.144
0	2.75	0	1.762	1.794	1.812
0.125	2.75	2.602562	0.968	1.092	1.234
0.25	2.75	5.194429	0.512	0.652	0.674
0.375	2.75	7.765166	0.332	0.341	0.348
0.5	2.75	10.30485	0.0181	0.0199	0.0218
0.625	2.75	12.80427	0.001	0.0138	0.0146
0.75	2.75	15.25512	-0.017	-0.0236	-0.034
0.875	2.75	17.65012	-0.064	-0.062	-0.06
1	2.75	19.98311	-0.08	-0.079	-0.08
1.125	2.75	22.24902	-0.133	-0.134	-0.133
1.25	2.75	24.44395	-0.156	-0.155	-0.151
1.375	2.75	26.56505	-0.167	-0.167	-0.168
		5%	-0.0715	-0.0699	-0.069
		NA value	0.323251826	0.321752876	0.321576485
		NA avg	0.322193729		